UNIVERSITÄT BERN

A Soft Tissue Image Guidance System for Percutaneous Needle Interventions Based on Multimodal Images

Graduate School for Cellular and Biomedical Sciences

University of Bern

PhD Thesis

Submitted by

Thiago Oliveira dos Santos

from Espírito Santo, Brazil

Thesis supervisor
Prof. Dr.-Ing. Stefan Weber
Institute of Surgical Technology and Biomechanics
ARTORG Center for Computer-Aided Surgery

Medical Faculty of the University of Bern

Original document saved on the web server of the University Library of Bern

This work is licensed under a
Creative Commons Attribution-Non-Commercial-No derivative works 2.5 Switzerland licence. To see the licence go to http://creativecommons.org/licenses/by-nc-nd/2.5/ch/ or write to Creative Commons, 171 Second Street, Suite 300, San Francisco, California 94105, USA.

Copyright Notice

This document is licensed under the Creative Commons Attribution-Non-Commercial-No derivative works 2.5 Switzerland. http://creativecommons.org/licenses/by-nc-nd/2.5/ch/

You are free:

to copy, distribute, display, and perform the work

Under the following conditions:

Attribution. You must give the original author credit.

Non-Commercial. You may not use this work for commercial purposes.

No derivative works. You may not alter, transform, or build upon this work.

For any reuse or distribution, you must take clear to others the license terms of this work.

Any of these conditions can be waived if you get permission from the copyright holder.

Nothing in this license impairs or restricts the author's moral rights according to Swiss law.

The detailed license agreement can be found at:
http://creativecommons.org/licenses/by-nc-nd/2.5/ch/legalcode.de

Accepted by the Faculty of Medicine, the Faculty of Science and the Vetsuisse Faculty of the University of Bern at the request of the Graduate School for Cellular and Biomedical Sciences.

Bern, Dean of the Faculty of Medicine

Bern, Dean of the Faculty of Science

Bern, Dean of the Vetsuisse Faculty Bern

Thesis supervisor

Prof. Dr.-Ing. Stefan Weber

Institute of Surgical Technology and Biomechanics

ARTORG Center for Computer-Aided Surgery

Medical Faculty of the University of Bern

Thesis co-supervisors

Dr. Mauricio Reyes

Institute for Surgical Technology and Biomechanics, Bern, Switzerland

Dr. Thilo Weitzel

Inselspital, Bern University Hospital and University of Bern, Bern, Switzerland

Thesis co-advisor

Prof. Dr. Philippe C. Cattin

University of Basel, Basel, Switzerland

Thesis mentor

Prof. Dr. med. Marco-Domenico Caversaccio

Inselspital, University of Bern, Bern, Switzerland

Medical Faculty of the University of Bern

External referee

Dr. Miguel Á. González Ballester

Head of the Research Department at Alma IT Systems, Barcelona, Spain

Acknowledgments

First of all, I would like to thank Prof. Stefan Weber and Dr. Mauricio Reyes for supervising me throughout this PhD program. I am thankful to Stefan Weber for all the guidance towards a clinically applicable solution. Thanks to his practical point of view, I had the opportunity to get touch with and gain experience on many different technologies related to computer aided surgery. I am also thankful to Mauricio Reyes for assisting me with the image analysis part of this project. Thanks to the ideas exchanged during these years, I could improve my medical imaging background. This joined guidance have considerably helped me with the completion of this thesis. Furthermore, I would like to thank Prof. Lutz-Peter Nolte for maintaining such a enthusiastic and inspiring environment at the Institute of Surgical Technology and Biomechanics (ISTB). The research atmosphere of the institute have motivated to peruse this title.

Additionally, I thank Prof. Dr. med. Marco-Domenico Caversaccio and Prof. Philippe C. Cattin for accepting being my mentor and co-advisor respectively. I also thank Dr. Miguel Á. González Ballester for accepting to be the external reviewer of this work.

On the clinical side, I would like express my gratitude to Dr. Thilo Weitzel who first initiated this project and created this PhD opportunity. I also thank Dr. med. Bernd Klaeser for all the support provided from the clinical side. I specially thank both for all the extra time spent on performing clinical experiments and writing articles. I am also thankful to Prof. Dr. med. Thomas Krause for enabling an environment for applied research at the nuclear medicine department of Inselspital.

To all my current and former colleagues from the ISTB, I would like to express my great satisfaction of having shared many nice moments in and out the institute. A special thanks to Dr. Matthias Peterhans for the great receptiveness when I first arrived and for all the valuable ideas exchanged during these years. Moreover, a special thanks to Kate Gavaghan for all the proofreading performed and the valuable inputs provided. Furthermore, a special thanks to all members of the computer aided surgery and medical image analysis groups for all the insightful meetings. Many thanks also to Annelies Neuenschwander and Barbara Schmitter for all the help with the difficult administrative work. Many thanks to all current and former members of the machine shop team for all the support during hardware manufacturing. A special thanks to Urs Rohrer for taking his time to teach me a bit of machine shop work. Likewise, I thank Ladina Ettinger for the support with the bio lab related questions.

I also owe a great thanks to my parents, who provided me with all the basis and studies I needed to get here. Finally, I am deeply thankful to my wife, Camila Soares de Magalhães, for joining me in this journey and for emotionally supporting me with love and happiness. I also would like to thank her for all the patience during the busy times and for always being such a good mood person who makes difficult moments easier.

Abstract

Percutaneous needle interventions have been widely used in medicine as minimally invasive alternatives to open surgical procedures. It supports a large number of applications including biopsy, wire marking, radiofrequency or microwave ablation, and percutaneous nephrolithotomy. In such interventions, a target point defined inside the human anatomy has to be reached by a needle through an entry point defined on the patient skin. The needle is typically guided by a structural modality like computed tomography (CT), and advanced towards the target with a step-by-step approach. A radio-opaque reference grid is placed on the skin of the patient (lying on the scanner table) around an estimated needle entry point. The patient is scanned and the reference grid as well as the lesion are identified in the image. Based on the imaged information, the needle is thus oriented and introduced in small steps towards the target. Each step is alternated with control CT acquisitions to ascertain the current needle position and orientation in respect to the grid and the target. The control scans are performed until the target is considered reached. Although effective, this approach have drawbacks that hinder a more efficient, more reliable, and side effect free procedure. Among these disadvantages, one can draw attention to: an excessive radiation exposure and intervention time due to the increased number of control CT scans, a limitation to perform punctures in the axial plane, a lack of patient to image registration to guide the needle, and a target displacement that might occur because of patient motion between two acquisitions in multimodal interventions. Stereotactic instrument guidance, also known as image guidance, is a possible approach to address such problems.

Image guidance is a technique used to increase accuracy and precision of clinical procedures by integrating pre-operative planning to an intra-operative scenario and by providing instrument guidance in anatomical areas of difficult visual access. Currently, there are no clinically established image guidance solution capable of addressing the problems associated to the standard clinical approach for percutaneous needle interventions while coping with all technical challenges associated to image guidance. State of the art image guidance systems for percutaneous needle intervention present limitations on handling multimodal data, on supporting punctures in different types of tissues such as bone and soft tissue, on referencing deformable parts of patient anatomy and on visualization methods without need for sight diversion from the patient. Hence, this work investigates advanced and clinically applicable methods to improve state of the art image guidance approaches and to address the issues of the current clinical routine.

This thesis starts by presenting an image guidance approach to support multimodal percutaneous needle interventions based on nuclear images. In a first stage, an image guidance system developed to aid multimodal interventions in stable regions of human anatomy (e.g. pelvis) is presented. The system, that integrates methods enabling punctures in soft tissue and bone, was evaluated in swine cadavers experiments. Results show that the achieved accuracy is sufficient for interventions based on positron emission tomography (PET) and CT datasets. Moreover, the methods demonstrated to increase visual intuitiveness and to facilitate the workflow of the instrument guided interventions. In addition, a registration pipeline for correcting target displacement caused by patient movement during bone interventions have been proposed and evaluated. The pipeline is able to isolate the bone of interest and to register a reference and a control CT images in order to correct the target in the reference PET image. Results show the feasibility of correcting target displacement during PET/CT intervention performed in bones.

In a second step, an image guidance approach to support interventions considering deformable regions of human's anatomy (e.g. chest and abdomen) is proposed. The approach is based on market available optical tracking systems and retro-reflective single markers spheres attached on the patient's skin. Firstly, a method for automatic patient-to-image registration is presented. Results show that patient-to-image registration can be performed without physician's interaction with the system. Additionally, a method for patient tracking under deformation is presented. Results show that soft tissue regions of the patient's anatomy can be tracked in real time while facing different intra-interventional conditions including deformation and occlusions. Furthermore, results show that identification of deformation with such approach is possible. Viewers displaying the current amount of deformation at the

region of the intervention enable physicians to perform gated punctures. Such an approach requires no extra hardware or complex setup, therefore it facilitates clinical integration.

Finally, an augmented reality projection approach is proposed in order to eliminate the need for sight diversion during image guided interventions. Using a portable image overlay device, needle guidance information could be displayed directly on the patient skin. Results show that guidance information is sufficiently visible at real time on the skin of the patient without the need for obtrusive hardware. Clinical integration was facilitated by using a plug-and-play device that does not need to be calibrated before each intervention. Such a direct visualisation was found to be highly intuitive because it eliminates the need for metal registration between the patient and the virtual scene displayed on monitors.

Contents

ACKNOWLEDGMENTS ..... **I**

ABSTRACT ..... **III**

CONTENTS ..... **V**

1 INTRODUCTION **1**

1.1 PERCUTANEOUS NEEDLE INTERVENTIONS 1
1.1.1 Applications 1
1.1.2 Image Modalities 2
1.1.3 Workflow 4
1.2 CLINICAL MOTIVATION 5
1.3 IMAGE GUIDANCE FOR PERCUTANEOUS INTERVENTIONS 6
1.3.1 Origin 6
1.3.2 Technical Challenges 7
1.4 THESIS OVERVIEW AND STRUCTURE 8

2 STATE OF THE ART **11**

2.1 OVERVIEW OF IMAGE GUIDED INTERVENTIONS 11
2.2 IMAGE DATA 12
2.3 POSITION MEASUREMENT PRINCIPLES 14
2.3.1 Instrument Tracking 16
2.3.2 Patient Tracking 17
2.4 PATIENT-TO-IMAGE REGISTRATION 19
2.5 VISUALIZATION 20

3 CURRENT DEFICITS **23**

4 AIMS AND APPROACHES **25**

5 IMAGE GUIDANCE FOR MULTIMODAL PERCUTANEOUS INTERVENTIONS **27**

5.1 A PET/CT BASED SYSTEM FOR SOFT TISSUE AND BONE PUNCTURES 27
5.1.1 Introduction 28
5.1.2 Material and Methods 29
5.1.3 Results 36
5.1.4 Discussions and Conclusions 40
5.2 LOCAL BONE REGISTRATION FOR PET/CT TARGET DISPLACEMENT CORRECTION 41
5.2.1 Introduction 42
5.2.2 Materials and Methods 43
5.2.3 Results 45
5.2.4 Discussions and Conclusions 47
5.3 PERCUTANEOUS NEPHROLITHOTOMY REQUIREMENTS AND WORKFLOW 47
5.3.1 Introduction 48
5.3.2 Materials and Methods 48
5.3.3 Results 51
5.3.4 Discussions and Conclusions 53
5.4 CLINICAL EXPERIMENT: PET/CT GUIDED ENT BIOPSY INTERVENTION 53
5.4.1 Introduction 53
5.4.2 Materials and Methods 54
5.4.3 Results 55
5.4.4 Discussions and Conclusions 56

6 TRACKING OF NON-RIGID ANATOMICAL STRUCTURES **57**

6.1 AUTOMATIC PATIENT-TO-IMAGE REGISTRATION 58
6.1.1 Single Marker Design 58
6.1.2 Single Marker Detection on CT Images 59
6.2 ANATOMY TRACKING FOR MOTION AND DEFORMATION DETECTION 67
6.2.1 Introduction 67
6.2.2 Materials and Methods 68

6.2.3 Results and Discussion ... 73
6.2.4 Conclusions ... 75
6.3 Integration into Percutaneous Needle Guidance ... 75
6.4 Clinical Experiment: Percutaneous Nephrolithotomy Intervention ... 76
6.4.1 Introduction ... 77
6.4.2 Materials and Methods ... 77
6.4.3 Results ... 79
6.4.4 Discussions and Conclusions ... 80
7 PROJECTION OF NEEDLE GUIDANCE DATA ON PATIENT ... 81
7.1 Portable Image Overlay Projector ... 81
7.2 Augmented Reality Applications ... 81
7.2.1 Introduction ... 82
7.2.2 Materials and Methods ... 83
7.2.3 Results ... 88
7.2.4 Discussions and Conclusions ... 90
8 CONCLUSIONS ... 93
8.1 Outlook ... 94
BIBLIOGRAPHY ... 95
LIST OF TABLES ... 103
LIST OF FIGURES ... 105
COMPLETE LIST OF PUBLICATIONS ... 113

1 Introduction

Brief: This chapter firstly introduces the clinical applications addressed in this thesis and describes the clinical issues that are associated with the current clinical approach. Subsequently, a technical solution is proposed and the technical challenges associated with it are presented. Finally, an overview and organization of this thesis are presented.

1.1 Percutaneous Needle Interventions

Percutaneous needle interventions have been widely used in medicine as minimally invasive alternatives to open surgical procedures. They not only allow patient treatment and diagnose in less time and with less surgical trauma than open surgery, but also allow patients with poor heart function that cannot undergo conventional surgery to benefit from an alternative treatment. In percutaneous needle interventions, a target point defined inside the human anatomy has to be reached by a needle or needle like instrument (see Figure 1 for examples) through an entry point defined on the patient skin. The needle placement is typically performed under the guidance of an available medical image modality and then used to perform an specific task that is dependent on the final medical procedure, i.e. treatment or diagnosis being performed.

a) 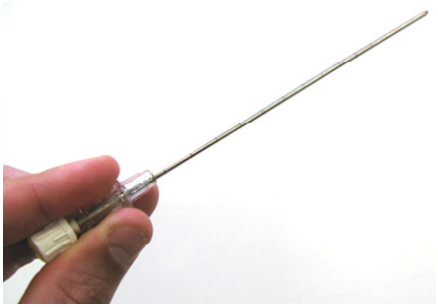 b) 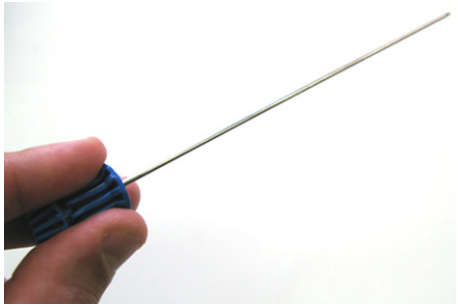

Figure 1: Two examples of needles used for percutaneous interventions.

In the following sections, the medical applications of the percutaneous needle interventions addressed within this work as well as the image modalities used for intervention guidance and the clinical workflow used for need placement are described in detail.

1.1.1 Applications

The number of medical procedures requiring percutaneous access to the human anatomy is large. In such applications, a cannula (i.e. a needle with hollow inside, see Figure 2) placed in the patient is typically used to guide specific medical tasks including biopsy, wire marking, radiofrequency or microwave ablation, and percutaneous nephrolithotomy among others. The cannula is normally combined with a trocar (i.e. a sharply pointed end instrument that fits in the cannula, see Figure 2) in order to facilitate puncture through soft tissue. After guiding the pair, cannula and trocar, to the aimed location, the trocar can be replaced by an application specific instrument. In biopsies for example, the trocar is replaced by a biopsy needle which is used to collect a sample of tissue from a suspicious region in the body for later examination and diagnosis. In wire marking, the trocar is replaced by a wire which is used to mark an anatomical structure. With the wire in place, the cannula can be removed and surgeons can later access the correct region in a more invasive surgical procedure. In ablation, the trocar is replaced by an ablation probe (radiofrequency or microwave) in order to ablate a lesion or

tumour. In percutaneous nephrolithotomy, the cannula is used to access the collecting system of the kidney in order to remove stones. Although all these applications share the need of a precisely placed cannula to perform a specific medical procedure, each relies on the visualization of different structures, and thus demands suitable image modalities to guide the needle to the target. In the following section, a description of the medical image modalities used for guiding needles in percutaneous interventions is presented.

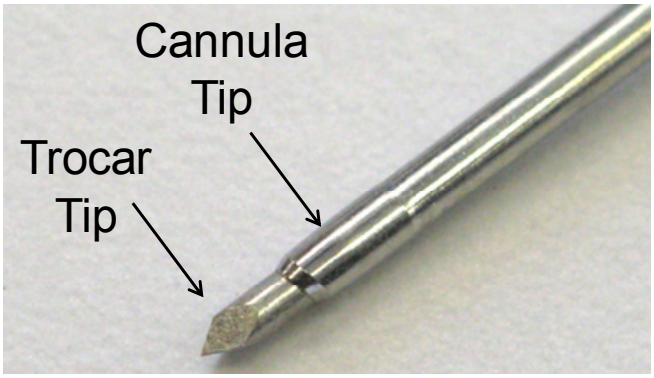

Figure 2: Example of a needle that is used to puncture soft tissue. It comprises a trocar and a cannula. The trocar fits inside the cannula and can be removed when it is not needed.

1.1.2 Image Modalities

Different image modalities for the guidance of needles during percutaneous interventions have been investigated, see Figure 3. Among them, one should emphasise planar image modalities like ultrasound [1, 2] and fluoroscopy [3], as well as volumetric image modalities like computed tomography (CT) [4, 5] and magnetic resonance (MR) [6]. Images for such modalities contain structural anatomical information that is used by physicians to correctly orient the needle within the patient. As mentioned by Huch *et al.* [7], each image is better suited to specific applications. Differences on acquisition time, flexibility of use, patient burden, image quality and visible content hinder the establishment of a common imaging device supporting all applications. Ultrasound imaging for example is versatile, has low cost, and is non-ionizing. However, the imaging range is limited to a certain depth and can only by applied to a limited variety of soft tissue interventions. Single fluoroscopic images provide quick access to a large field of view, but cannot provide three-dimensional orientation. In addition, it is based on ionizing radiation that is harmful to the patient and therefore should not be continuously used. CT and MR images on the other hand provide 3D image datasets, but are less versatile and have higher costs. While CT images provide greater detail of bone structures, MR provides more information about soft tissue. Like fluoroscopes, CT scanners are also based on ionizing radiation that are harmful to the patient, but can acquire images without restriction to ferromagnetic materials. Although different image types are available, clinical applications protocols are typically well defined with one or more of the available modalities.

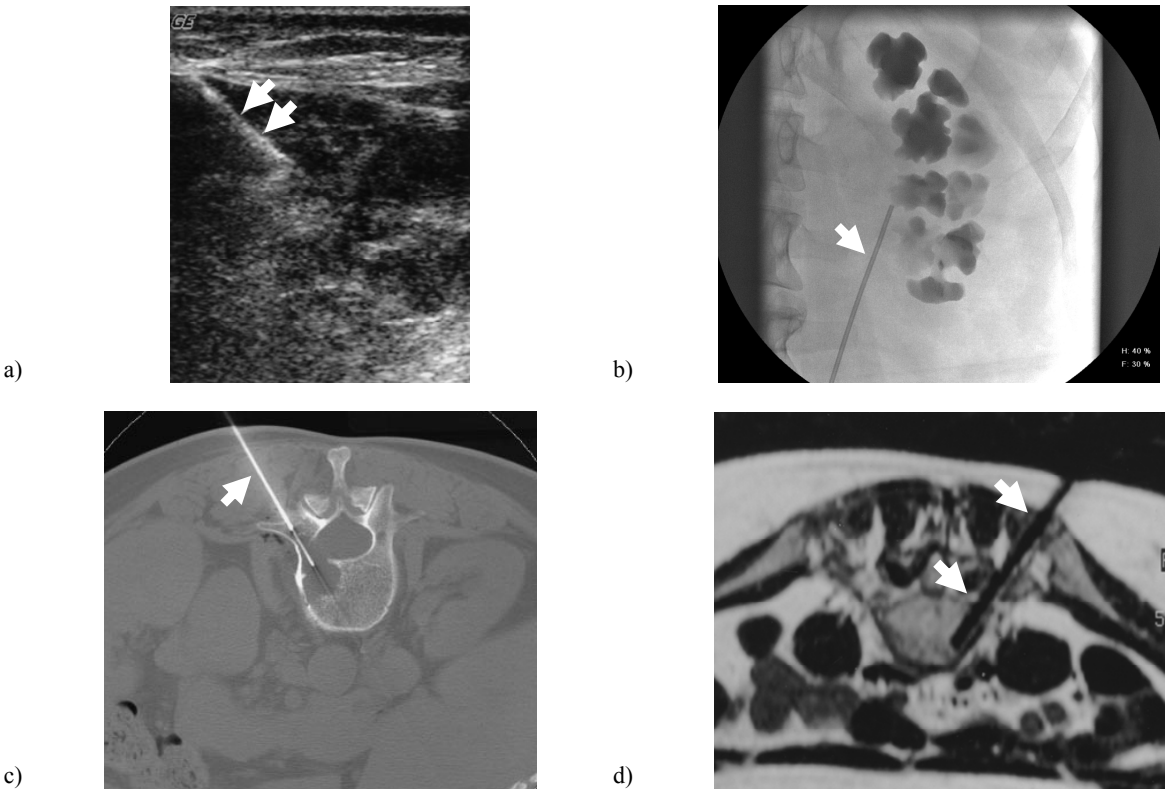

Figure 3: Examples of different image modalities used for needle (pointed by arrows) guidance. a) Ultrasound-guided biopsy (Source: [8]). b) Fluoroscopic needle guidance for percutaneous nephrolithotomy. c) CT-guided biopsy of vertebral body (Source: [9]). d) MR-guided biopsy of vertebral body (Source: [10]). Arrows were additionally added to the images.

In recent years, nuclear imaging has fundamentally changed oncological procedures with the improvement of functional modalities such as single photon emission computed tomography (SPECT) and positron emission tomography (PET). Functional images are able to capture changes in metabolism and therefore highlight possible lesions even before anatomical changes occur. By using multimodal combinations of structural and functional modalities (e.g. SPECT/CT and PET/CT), image understanding and therefore diagnosis can be optimized [11–13]. With these multimodal techniques even suspicious lesions without morphological correlation, i.e. not evident in structural datasets like CT, can be identified and verified histologically [14]. With the advent of these functional modalities, the range of percutaneous interventions have been extended. Interventions that were previously based on a single modality like CT have been extended to use multimodal datasets. In multimodal based interventions, the volumetric functional image (e.g. PET and SPECT) provides information about the suspicious lesion (i.e. target), while the volumetric structural image (e.g. CT and MR) provides anatomical information for geometric needle guidance. Physicians usually rely on information provided by a fused dataset comprising two different modalities. The principles and acquisition protocols of two common modalities used for percutaneous intervention (PET and CT) are briefly described below.

CT images are based on the detected attenuation of X-ray beams crossing the human body. PET is based on the principle of coincidence detection of photons emitted by positrons after interaction with matter [15]. While CT scanners produce and detect the beams being measured, PET scanners function passively as a detector. Typically during PET imaging, a radiopharmaceutical tracer is injected in to the patient blood stream. Metabolic changes are highlighted by detecting the concentration of positrons emitted at different regions of the body. A common radiopharmaceutical used during PET studies is the ^{18}F-Fluorodeoxyglucose. The administration of radiopharmaceutical is performed 40 to 60 minutes before scanning in order to allow time for the body to absorb the tracer. During the scan, the patient lies on the PET/CT scanner table and is asked to remain as still as possible for the entire study. A CT image is first acquired with the patient on breath hold. A whole body CT acquisition lasts a few seconds and is additionally used for attenuation correction of the PET image. After the CT acquisition, a whole body PET is then acquired. A whole body PET image comprises a few single bed acquisitions

(around 5) and is more time consuming than the CT. Considering current PET/CT scanners (e.g. Siemens Biograph 16 Hi-Rez), each single bed position takes two to four minutes and image reconstruction takes three to six minutes. Such scanners deliver two volumetric datasets, one CT and one PET, sharing the same coordinate system. Therefore, image fusion and visualization can be automatically performed by overlaying the two datasets.

1.1.3 Workflow

Percutaneous needle intervention based on PET/CT images is usually performed using a step-by-step technique [16] that is very similar to interventions based only on CT images [7]. Currently, multimodal oncologic interventions are performed in the same room in which the patient is scanned, and are pre-planned based on a diagnose PET/CT dataset. Firstly, the suspicious lesion is identified and a coarse needle entry point is defined in the diagnose image. With the patient lying in the scanner table (see Figure 4a), a radio-opaque reference grid (used to facilitate the guidance of the needle to the lesion) is placed on the patient's skin around an estimated needle entry point. A reference image comprising a single-bed PET/CT acquisition of the patient already positioned for the procedure is then acquired. After identifying the reference grid and the lesion in the reference dataset, the needle is oriented and introduced in small steps. Each step is alternated with control CT acquisitions to ascertain the current needle position and orientation in respect to the grid and the target. The physician, that is positioned beside the patient, mentally adjusts the needle according to the previous acquired control CT (see Figure 4b). The control scans are performed until the target is considered reached. With the needle in the right place, the physician is able to perform the intended task (e.g. biopsy, wire placement, ablation, etc). In some interventions (e.g. biopsies), the patient is fully awake, under only the effect of local anaesthesia. Such cases require physicians to better control unexpected patient motion.

a) b)

Figure 4: a) Illustration of a patient positioned for a PET/CT image acquisition (Source: © Siemens AG). b) Example of a PET/CT-guided needle placement for biopsy.

With the exception of percutaneous nephrolithotomy (described below) which is not performed in the same room in which the patient is imaged, the approach to guide the needle to the target is basically the same regardless the final medical application. However, the protocol is slightly modified if the target is located in bony tissue. Such a change is required due to the rigid nature of the bone which resists puncture from the trocar and thus prevents further advance to the target. In such cases, the trocar is replaced by a drill (i.e. drilling instrument that fits in the cannula and is used to penetrate the bone) as soon as the needle reaches the bone surface. See Figure 5 for an example of a bone biopsy kit. The physician can then drill to the target. The depth of the drill is controlled with the help of distance holders (provided with the drilling kit), which prevents drilling deeper than a specified value.

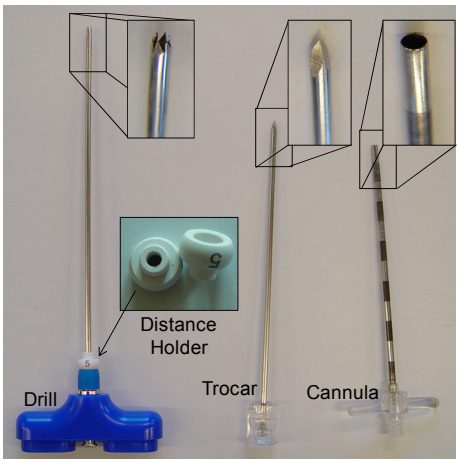

Figure 5: Bone biopsy kit example comprising a cannula of 3.4 mm outer diameter (10 G) and 130 mm length, a trocar, a drill and 5 mm long distance holders.

As mentioned above, percutaneous nephrolithotomy interventions are typically performed in a different location to where the planning CT image is acquired. Firstly, the patient is scanned and subsequently transferred to the intervention room. Percutaneous nephrolithotomy is typically performed with the patient in the standard prone position allowing a large surface area for the puncture site, less tissue along the path to the kidney, and a wide space for instrument manipulation. After planning the access points to the collecting system of the kidney, the actual puncture is performed under the guidance of ultrasound and fluoroscopic images. Thereafter, a guide wire is placed through the needle and the puncture channel is dilated in order to place a 30 French dilatators sheath (Amplatz). Thereafter, the stone can be fragmentized and removed in pieces using minimally invasive instruments.

1.2 Clinical Motivation

Although effective, current clinical approaches used for needle guidance have certain drawbacks that hinder a more efficient, more reliable, and side effect free procedure. A detailed description of the disadvantages related to the current clinical methods is presented below.

Excessive radiation exposure: Physicians typically ensure the current orientation of the needle by acquiring a control CT image after advancing the needle towards the target. Small needle steps in the direction of the target are alternated with control CT acquisitions to ensure correct needle placement. Therefore, several control CT images are usually necessary before the needle reaches the target. The number of acquisitions required increases with the complexity of the procedure. If the target is located close to an important organ or vessel that should be avoided, the needle step size is naturally decreased to obtain more guidance feedback. Such an excessive number of images increases not only the radiation burden to the patient, but also to the personnel, especially in case of nuclear images (e.g. PET and SPECT).

Excessive intervention time: In addition, the total procedure time is increased due to the high number of control images resulting also in an increased overall intervention cost.

Axial plane limitation: In order to minimize the patient's radiation exposure, control CT acquisitions, that capture only a small volume around the needle, are performed. Due to the construction limitations imposed by spiral CT scanners for example, image volumes are typically acquired as a stack of planar axial images. Therefore, the smallest possible volume to be acquired on a regular CT scan is a planar image in the axial direction. Such constraint limits the planning and guidance of the percutaneous intervention to the axial plane. Consequently, the needle entry point has to be planned in the same or adjacent axial image plane as the target. Such limitation imposes difficulties to procedures in which a clear path without obstacles (e.g. bones or important structures that should be avoided) cannot be found in the axial plane.

Lack of patient-to-image registration: During needle insertion, a correspondence between the visualized image and the actual patient lying on the table has to be found. In order to facilitate the achievement of such registration, a radio-opaque reference grid placed on the patient skin is used for orientation. Physicians typically locate the reference grid in the image and mentally align it with the one on the skin. Any necessary correction of the needle orientation is performed based only on the reference grid on the skin. Such poorly performed alignment makes the procedure non intuitive and therefore prone to errors.

Target displacement: This effect appears during multimodal interventions like PET/CT. Because of the increased time demanded for local PET acquisitions, the control acquisitions of the needle position is usually not performed as a complete PET/CT dataset, but as single CT acquisitions only. Such CT images are typically co-displayed with the first acquired PET image. However, this method does not account for possible displacement of the lesion which might occur between the first PET/CT acquisition and the control CT scans. Such displacements are usually a result of patient movement caused by the interaction between the needle and the bone when drilling, or by an involuntary rearrangement on the scanning table. Independent of their cause, these motions may produce a significant target displacement in the co-displayed PET and control CT images during the intervention (according to clinical observations often 5-10 mm), see Figure 6. Physicians have therefore to mentally compensate for these displacements which can potentially lead to an erroneous needle placement. Consequently, the number of necessary punctures and CT image acquisitions increases causing discomfort and unnecessary radiation exposure to the patient.

a) b)

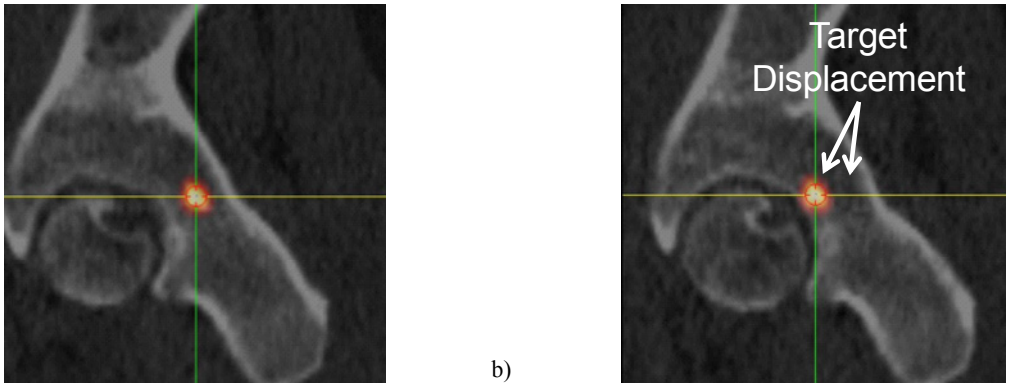

Figure 6: PET/CT image fusion showing a lesion in the bone. a) Initial PET fused with initial CT. b) Initial PET fused with control CT. The target displacement introduced by patient movement is highlighted by the arrows.

1.3 Image Guidance for Percutaneous Interventions

Stereotactic instrument guidance, also known as image guidance can address the problems presented above and improve quality of percutaneous needle intervention. Image guidance is a technique used to increase accuracy and precision of clinical procedures by integrating pre-operative planning into an intra-operative scenario and by providing instrument guidance in anatomical areas of difficult visual access. With image guidance systems, also known as navigation systems, physicians can visualize pre-operative data (e.g. patient anatomy image or models) simultaneously with intra-operative information. Surgical instruments are usually overlaid on pre-operative data to provide a virtual overview of the current surgical scenario, aiding in the execution of the intervention.

1.3.1 Origin

Evolving from stereotactic frames that were first applied to neurosurgery in 1908 [17], image guidance has made its way to the modern frameless stereotactic interventions through the pioneer works of Roberts *et al.* [18], Watanabe *et al.* [19], Kosugi *et al.* [20], and Friets *et al.* [21] (an extensive description of the development and evolution of this technology can be found in [22]). Their work motivated many other groups and since then, many position measurement systems have been devel-

oped in order to provide frameless instruments and anatomy referencing. Relying on such position measurement systems to estimate the pose of surgical instruments, image guidance has been successfully applied to many medical fields including orthopaedic [23, 24], neurologic [24], and ear, nose and throat (ENT) [25, 26] surgeries as well as other interventions performed on rigid structures like bones [24, 27–30]. The general principles of image guidance are described in [27, 28].

1.3.2 Technical Challenges

In order to transfer image guidance techniques from the surgical to the percutaneous needle intervention field, a set of issues raised due to the differences in requirements of these two types of procedure have to be addressed. The level of invasiveness of the procedure that should not be increased, the soft tissue nature of the human anatomy that is not considered in surgical scenarios targeting rigid structures (e.g. bone and head), as well as the clinical protocols followed during different percutaneous needle intervention applications are examples of challenges that must be overcome. An overview of the challenges that have to be considered to obtain a clinically applicable solution for percutaneous needle interventions is presented in the diagram of Figure 7 and is described below.

Figure 7: Challenges faced during investigation of a clinically applicable navigation system for percutaneous needle intervention.

Sufficient accuracy, precision and robustness: The proposed solution should be precise and accurate enough to safely perform the intended procedure. In addition, such a system should be robust to daily conditions faced in the clinical environment without interfering with nor being interfered by clinical routine.

Compliance to imaging protocols: In order to preserve the clinical workflow used in interventions based on multimodal datasets (e.g. PET/CT), such systems have to function with currently used image acquisition protocols considering resolution, acquisition time, and acquisition sequence.

Efficient planning: Percutaneous interventions are usually planned dynamically with the patient already prepared for needle insertion. Therefore planning should allow fast definition of a target and entry point as well as real time image data manipulation and visualization. Additionally, the planning should facilitate assessment of risk structures and of obstacles surrounding the planned needle path.

Patient referencing: Ideally, the image data would describe the current state of the patient at any point in time during the intervention. However with current state of the art of CT scanners, such dynamic anatomical representation is not possible without increasing harm to the patient or reducing the anatomical information in the image. A real time representation of the patient anatomy state is especially important for patients that are awake during the intervention. In such interventions, the patient

state is not only affected by motion, but also by soft tissue deformation of certain regions of the human anatomy. In case of procedures aiming anatomical regions like the chest or abdomen, investigation of methods for referencing soft tissue anatomy and for identifying deformations caused by patient breathing or any other movement is essential.

Efficient visualization: In case of multimodal based intervention, real time visualization of fused functional and structural volumetric datasets is necessary. For that reason, efficient data handling and visualization, supporting multiple datasets have to be explored. In addition, an optimal visualization should maintain the patient in the field of view of the physician.

Clinical integration: Although essential, this item is very often overlooked by many researchers when investigating methods to be used within a clinical environment. Usually, clinical protocols, time and available space are very well defined and changes are not allowed, or are difficult to introduce. Therefore, any data transfer, interaction with the system or additional equipment to be placed in the intervention room has to respect the constraints imposed by the clinical environment. System setup time as well as the sterility phases and areas are examples of very important requirements that should be considered in the development and evaluation process. Additionally, compliance to different clinical protocols (e.g. for targets located in different types of tissue like bone or soft tissue) is necessary for a successful clinical integration.

1.4 Thesis Overview and Structure

Currently, there are no clinically established image guidance solutions capable of addressing the problems associated with the standard clinical approach for percutaneous needle intervention while coping with all technical challenges mentioned. This thesis investigates advanced and clinically applicable image guidance methods and techniques to address the problems related to the current used clinical approach. The investigated methods should not only overcome individual challenges associated with the different aspects of image guidance, but also provide a unified solution that can be used in clinics.

This thesis is organized as follows:

- *State of the Art (Chapter 2)* begins by presenting an analysis of the state of the art of image guidance systems applied to percutaneous needle interventions. Firstly, the system is broken down in different aspects which are reviewed individually. Finally, the advantages and disadvantages associated with currently used approaches are discussed.
- *Current Deficits (Chapter 3)* identifies and summarizes the deficits of the state of the art approaches in order to reveal the aspects requiring improved solutions.
- *Aims and Approaches (Chapter 4)* describes the approaches proposed within this thesis in order to overcome the indentified deficits.
- *Image Guidance for Multimodal Percutaneous Interventions (Chapter 5)* presents the design, workflow and error analysis of a navigation system for multimodal based percutaneous interventions which facilitates needle placement for lesions located in soft tissue and bone. Additionally, it proposes a registration pipeline for correcting target displacement during bone interventions. Subsequently, an analysis of the requirements and workflow of a navigation system to perform percutaneous nephrolithotomy interventions is performed in order to extend the image guidance methods to different applications. Finally, a clinical biopsy case in the nasal cavity is performed with the system.
- *Tracking of Non-Rigid Anatomical Structures (Chapter 6)* proposes an approach for interventions to be performed in non rigid parts of the anatomy like chest and abdomen. Firstly, a method for automatic patient-to-image registration is presented in order to reduce the interaction between the physician and the system. Secondly, a method for soft tissue anatomy tracking under deformation is presented. Finally, both methods are integrated in the developed system. A clinical experiment evaluating the clinical integration of the presented approach is also presented.

- *Projection of Needle Guidance Data on Patient (Chapter 7)* presents an augmented reality visualization approach that projects needle guidance information directly on the patient skin. The presented method, which is based on a recently developed portable image overlay projector, is evaluated for different applications including percutaneous needle intervention.
- *Conclusions (Chapter 8)* discusses the general findings of this work and concludes the thesis in addition to presenting an outlook for future research.

2 State of the Art

Brief: This chapter presents an analysis of the state of the art of image guidance systems applied to percutaneous needle intervention. Firstly, the general concept of image guidance is presented and subdivided in different aspects for further analysis. Finally, a detailed literature review describes the current approaches used to address each aspect of image guidance.

2.1 Overview of Image Guided Interventions

For the purpose of analysis, the image guidance topic has been divided into four main aspects within the section: image data, position measurement principles comprising instrument tracking and patient tracking, patient-to-image registration and visualization. Whilst each of these items has specific requirements that vary from one application to the other, all maintain core functionality that is described as follows.

- *Image data* is used to plan the procedure and to provide anatomical guidance during the intervention. It is typically acquired prior to the intervention and has its own coordinate system, *img*.
- *Position measurement principles* are used to estimate the pose of dynamic references in a tracking space. Typical homogeneous transformations, ${}^{pms}T_{dr}$, to map points from the dynamic reference coordinate system, *dr*, to the position sensor coordinate system, *pms*, are provided. Each homogeneous transformation is composed of a three dimensional (3D) rotation and a 3D position.
    - *Instrument tracking* is used to determine the pose of an instrument within the position measurement system tracking space. It is typically achieved by attaching (or integrating) a dynamic reference on (or in) the respective instrument in order to provide a reference coordinate system, *idr*.
    - *Patient tracking* is used to determine the pose of the patient within the position measurement system tracking space. Considering rigid structures like bone, it can be achieved in the same way as the instrument tracking, i.e. by attaching a dynamic reference to the structure in order to provide a reference coordinate system, *pdr*.
- *Patient-to-image registration* is used to calculate the transformation, ${}^{img}R_{pdr}$, that maps points from the patient's anatomy to the image data. The registration is typically accomplished by matching corresponding features that can be visible in the patient and the image.
- *Visualization* of the image data overlaid by virtual instruments representing the actual position of the tracked instruments is finally achieved by applying the composition of transformations described in equation (1).

$$ {}^{img}T_{idr} = {}^{img}R_{pdr} \, ({}^{pms}T_{pdr})^{-1} \, {}^{pms}T_{idr} \qquad (1) $$

In order to understand the transformation model of image guidance, an overview of a generic system for neurosurgery is illustrated in Figure 8. Current state of the art position measurement systems can calculate the pose of dynamic references in real time. Consequently, actions performed on the

patient are reflected on a monitor display highlighting parts of the anatomy of difficult visual access. In addition, planning information can be displayed during the intervention so that physician's actions can be performed with maximal correspondence to the planned scenario.

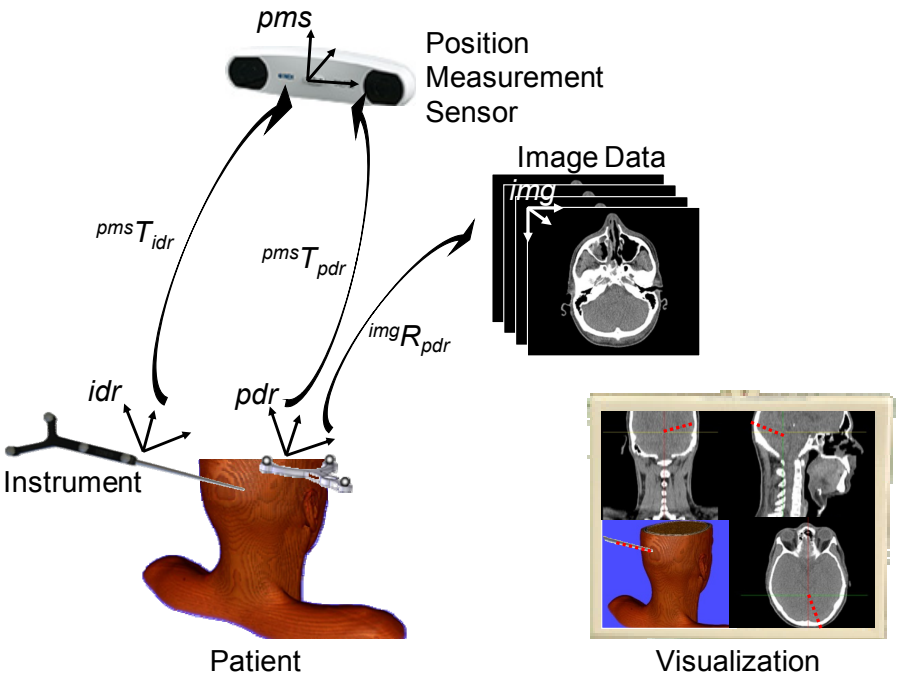

Figure 8: General navigation system overview. The instrument and patient poses, ${}^{pms}T_{idr}$ and ${}^{pms}T_{pdr}$, are measured by the position measurement system and overlaid on the image data by means of a patient-to-image registration transformation, ${}^{img}R_{pdr}$ (as illustrated in the visualization).

Navigation systems for percutaneous needle intervention follow the same general principals described previously and can also be divided into four main aspects (see Figure 9). Although working together towards a single solution, the research focus given to each of these aspects varies according to the application and to the research group. In the next sections, a detailed review of the literature presents the current state of the art of each of the aspects illustrated in Figure 9 giving a special focus on systems for percutaneous needle interventions.

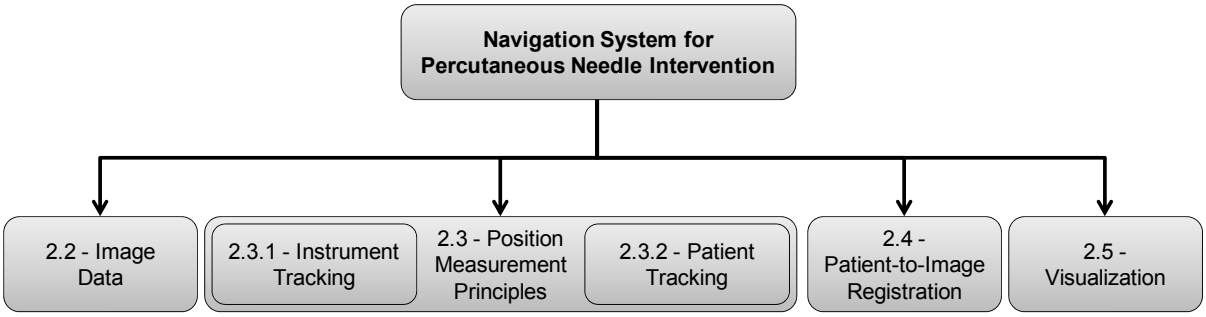

Figure 9: Image guidance systems subdivided in four aspects.

2.2 Image Data

As in the non-navigated image-guided intervention, image data provides anatomical information to guide physicians to a specific point within the human anatomy during navigated needle guidance. The modality used for such procedures is typically dictated by the medical application, and imposes constraints that have to be handled by the navigation system. Data transfer and handling, image resolution and size, and acquisition time are some of the limitations to be considered by systems aiming to

provide real time interaction. In addition to the interaction aspects, establishing image correspondence of misaligned datasets is mandatory for correct fusion and displaying. During percutaneous interventions, images are misaligned when fusing pre- and intra-interventional images after patient movement between two acquisitions. Several image co-registration methods have been investigated in the literature (a complete explanation of image registration methods can be found in [31]). Such techniques are used to align two images by establishing correspondence between voxels in each dataset. Many types of image co-registration exist (ranging from rigid methods, which only considers an overall rotation and translation, to non-rigid methods, which considers several degrees of freedom to map local patches or even voxels across the two images). This section presents an overview of the current systems used to address problems related to image data, with a special focus to CT and/or PET modalities.

Navigated intervention based on CT images has already been established within orthopaedics, neurologic, and ENT surgeries, and is one of the most common modalities for navigated percutaneous interventions. During CT based navigated interventions, the level of radiation exposure to the patient and personnel is minimized by performing the entire procedure with one single acquisition. In some cases, such image data is acquired prior to the intervention allowing for planning and for 3D models that provide more intuitive anatomical guidance. In some other cases, the image data is acquired during or immediately prior to the intervention demanding therefore, a low overhead for data transfer to the navigation system and planning as well as real time data manipulation and visualization. Many studies have been performed [32–42] to address and to evaluate requirements associated with percutaneous interventions based on a single modality like CT. Results have shown that the required accuracy, real time data manipulation and visualization can be achieved with existing computers. Data transfer is usually accomplished using media or network. However, systems able to handle multimodal data like PET/CT volumes still demand investigation.

Taking advantage of the information provided by multiple datasets, Militz *et al.* [43] successfully showed that standard commercial navigation systems can be used to perform multimodal based intervention. Nevertheless, the datasets have to be manipulated and fused prior to the transfer to the navigation system decreasing therefore operational flexibility. With a more advanced method, other groups [44, 45] have reported navigation systems able to handle multimodal data and to combine pre- and intra-interventional images for needle guidance (see Figure 10). Phantom experiments demonstrated the potential of such systems to work with multimodal images in a lab setup without considering clinical constraints (sterile phases, image acquisition protocols, etc.) imposed by clinically approved protocols for oncologic needle intervention such as presented in [14].

a) 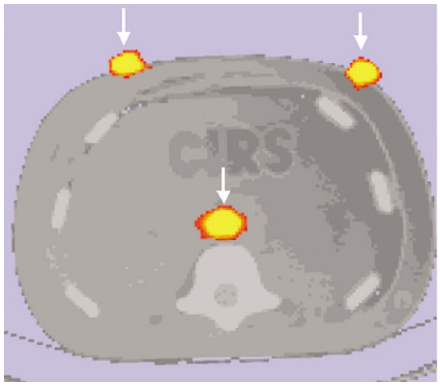

b) 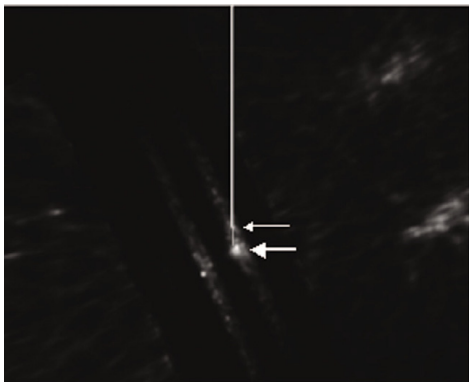

Figure 10: Image modalities experiments realized in (Source: [45]). a) PET/CT image of the interventional phantom with 6 mCi of ^{18}F-Fluorodeoxyglucose fiducials (arrows). b) Tracked needle position (small arrow) is displayed near internal target (large arrow) from pre-procedural PET during tracked needle insertion.

In a more recent report [46], a research navigation system [47] which is able to handle multimodal images was clinically evaluated on a set of patients undergoing biopsy or ablation. Such a system can import prior diagnostic PET or PET/CT volumes along with an intra-interventional CT volume. As an additional feature, automatic and manual co-registration methods for aligning the coordinate systems of PET and CT images are provided. Such alignment is specially required when fusing pre- to

intra-interventional data. In [48], Wood *et al.* present a summary of the necessary clinical workflow for using such a system in ablation procedures. In case of bone needle intervention based on PET/CT, an additional need for correction of target displacement is raised. In such procedures, the region of interest to be registered comprises non-rigid and rigid structures (e.g. soft tissue and bones) that move independently to each other. Moreover, the images to be registered (control and reference CT) contain undesired objects such as the puncturing needle and metal artefacts that might affect the accuracy of standard registration algorithms [31].

2.3 Position Measurement Principles

Position measurement systems, also known as tracking systems or localizers, are essential components to image guidance systems. They are responsible for measuring the pose of instruments relative to a reference that is typically set to the patient's anatomy. Since the advent of image guidance, many technologies providing referencing within a medical environment have been investigated including mechanical arm [49], ultrasonic [50], optical and electromagnetic systems. Mechanical arm systems use encoders and arm segments to estimate the position of instruments attached to an arm. Ultrasonic systems rely on microphones to capture sound transmitted by a dynamic reference to triangulate the dynamic reference position. However, due to of lack of dynamic referencing, limits on joint orientation, lack of accuracy, as well as other disadvantages related to these first two technologies, optical and electromagnetic systems have become most commonly used. A detailed description of the latter two technologies is presented below.

Optical tracking systems: This technology uses cameras to recognize and to calculate the pose of dynamic references containing specific markers. Two types of systems can be found today: active and passive. Active systems rely on infrared light emitted by diodes attached to a dynamic reference at known positions. The light is captured and used to recognize and estimate the dynamic reference pose via triangulation. Such systems require a wired connection between the dynamic reference and the camera in order to synchronize and power the diodes. The synchronization ensures a unique correspondence between each diode and the calculated position. An additional wireless version of dynamic references built for active technology is also available, but challenges with sterilization are introduced because of the presence of batteries. Several active optical tracking systems are available on the market including NDI Optotrak and NDI Polaris from Northern Digital Inc. (Waterloo, Canada), and accuTrack from Atracsys (Lausanne, Switzerland). Passive systems rely on markers, retroreflective infrared spheres or specific patterns, attached to a dynamic reference at known positions to recognize and estimate the dynamic reference pose via triangulation. No wired connection is necessary. However, for each distinct dynamic reference based on infrared markers a unique geometry is required, increasing therefore their final size. Additionally, smaller visibility angles are obtained for dynamic references based on specific patterns because of their flat shape. Several passive optical tracking systems are also available on the market including infrared based systems like NDI Polaris from Northern Digital Inc., specific pattern based systems like MicronTracker from Claron Technology Inc. (Toronto, Canada), and hybrid systems like infiniTrack from Atracsys.

Electromagnetic tracking systems: This technology uses electromagnetic signals produced by a field generator placed near to the intervention area to induce a voltage on sensor coils attached to a dynamic reference. The voltage induced on the coil sensors are used to estimate their pose. Basically, two types of coils are available: single coils that provide poses on only five degrees of freedom, and combined coils that provides poses on six degrees of freedom. A wired connection to the coil is necessary to measure the voltage induced. The small size of these coils (from 0.5 to 1 mm diameter and 5 to 10 mm length) makes it possible to directly embed the coils in the tip of the instrument. Like the optical tracking systems, several electromagnetic system are available on the marker including Aurora from Northern Digital Inc., and microBIRD from Ascension Technology Corporation (Burlington, Vermont, USA).

Electromagnetic vs. optical tracking systems: In order to identify the best application for each technology, many researchers have been studying the advantages and disadvantages of both systems. In [51], optical tracking is said to be a mature and reliable technology providing better accuracy and

robustness than electromagnetic systems. Two main disadvantages are associated with optical systems: the distance between the markers, which requires larger dynamic references for better accuracy, and need for line-of-sight between the camera and the dynamic references. Electromagnetic systems in the other hand, do not require line-of-sight, but do require wired connection to the tracked instruments [30]. The main advantage of tracking without a line-of-sight is the ability to determine the position of the tip of instruments (requires coil to be embedded on the tip) without being affected by instrument deflection. However two major disadvantages are brought by electromagnetic technology, interference by metal devices, which affects the overall tracking accuracy, and the smaller tracking volume.

Such different characteristics have led research groups to a split opinion regarding the technologies to be used in navigation systems for percutaneous needle interventions. Some groups have opted for passive optical systems, whilst others for electromagnetic systems. Active optical systems, although very popular in orthopaedic surgery are not commonly seen in minimally invasive procedures. As an example of groups using passive optical tracking, one can highlight the IRCAD group in France who use an in-house built optical tracking system to track patterns attached to the needle and markers attached to the patient [34–37, 52, 53] (see Figure 11a); the group from the German Cancer Research Center (DKFZ) in Heidelberg, Germany [40, 54–57] (see Figure 11b); as well as the independent work of other groups [32, 58–60]. From the electromagnetic side, one can highlight the work from the National Institute of Health (NIH) in the USA [40, 42, 45, 46, 48, 61] (see Figure 11c); as well as the independent work of other groups [41, 62, 63]. Trying to take advantage of the two technologies, some groups have investigated the possibility of constructing hybrid navigation systems for medical augmented reality [38, 39, 64] (see Figure 11d). The optical tracking is used to track the physician's head and the semi-transparent display while the electromagnetic tracking is used for needle tracking.

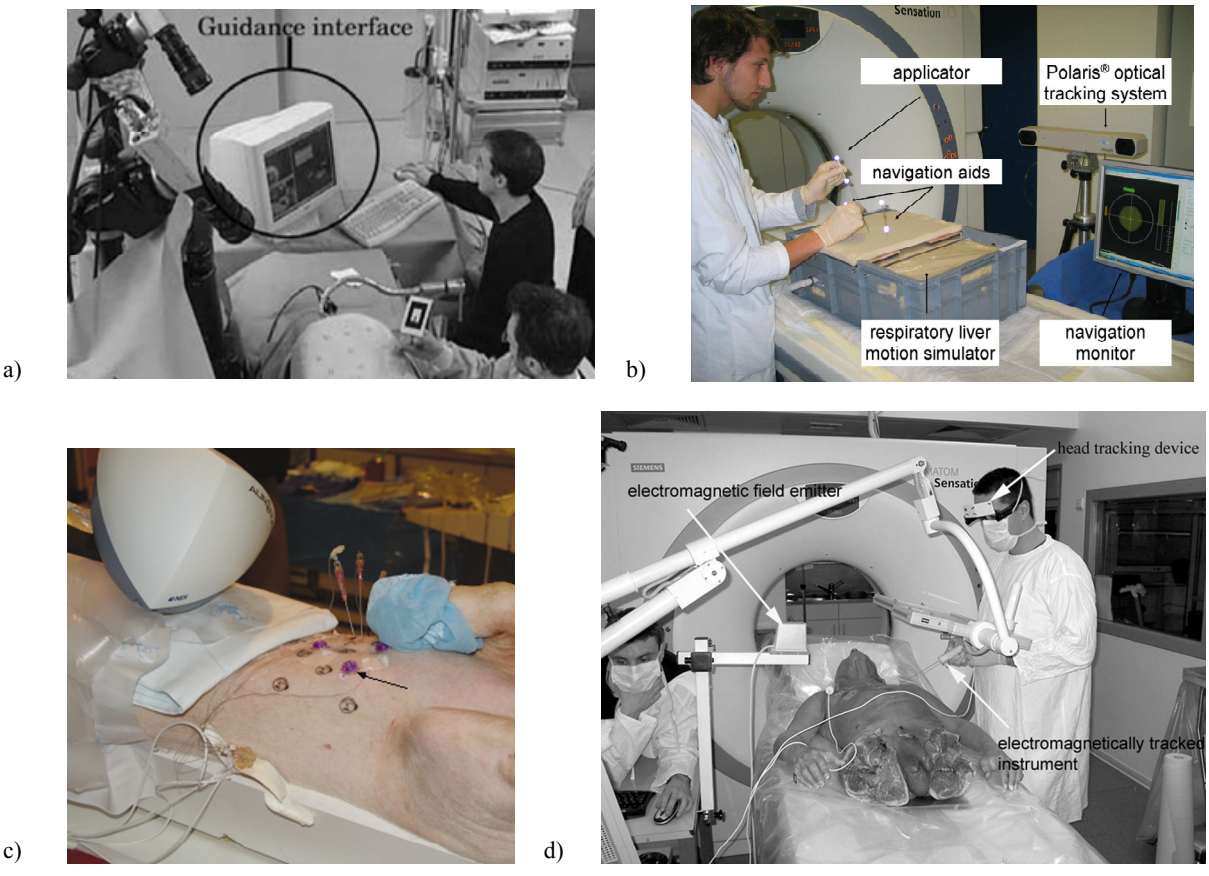

Figure 11: Experimental setups highlighting: a) the self developed stereoscopic optical system, the guidance interface and the user performing the puncture with the tracked needle (Source: [35]); b) the Polaris optical tracking system from NDI, the guidance interface and the user performing the procedure (Source: [40]); c) the electromagnetic field generator Aurora from NDI, the fiducials used for registration, and the tracked needle (Source: [45]); d) the electromagnetic field generator, the head tracking device (optical tracking), and the instruments being tracked (Source: [39]).

In summary, currently used tracking systems are based either on optical or electromagnetic technology. Both technologies are readily available on the market and can be used as certified measurement tools. Although improvements can, and should, still be investigated, both tracking systems have already reached a state of clinical acceptance that allows them to be used in clinical environments. Tracking solutions based on in-house technology can also be found in the literature, but certification and approval for use within clinical environments is not provided thus, hindering the use of these solutions in clinical research.

2.3.1 Instrument Tracking

Instrument tracking, i.e. needle tracking in the case of percutaneous needle intervention, provides referencing to instruments within a tracked, or navigated space. It can be achieved by attaching a dynamic reference, that can be detected by the tracking system, to the instrument. This method was widely used in the early days of surgical navigation and is still well accepted today. The easiest and most straight forward place to attach such a dynamic reference is the shaft of the needle. The shaft remains outside the patient's anatomy and thus can provide the required line-of-sight to the optical tracking system. Clamps can easily be manufactured to connect dynamic references to a large variety of needles. Nevertheless, with the improvement of electromagnetic systems, the tip of the needle is the preferable place to embed the dynamic reference. Needle tip tracking is insensitive to problems such as needle deflection which are well described by Abolhassani *et al.* in [65]. It has been showed that such effect can be significant, hence, different research groups have been trying to understand and model the deflection of needles [66–68]. Okamura *et al.* [68], for example, have shown that deflection can be minimized by using needles with conical and triangular tip shapes due to their symmetry. Alternatively, stiff needles could be employed in order to minimize or avoid the bending effect. Although more robust to needle deflection, tip tracking requires specific needle designs to be premanufactured with the integrated coil sensor therefore, limiting the range of needle types that can be used.

Regardless of the position of the attached dynamic reference, shaft or tip, the pose of the needle, i.e. the tip location and the axis orientation, relative to the attached dynamic reference has to be known prior to use. Therefore, a calibration method is required [69]. The calibration of pointing devices such as needles is also well established and is usually achieved using pivots, chamfers, or other tracked instruments with well known geometries as calibration units. Pivots are used to obtain the location of the needle tip whereas chamfers are used to obtain the axis orientation. Tip location can be calculated by placing the needle tip on a pivot and rotating the shaft (as shown in Figure 1a) while performing a set of measurements (rotations and translations of the dynamic reference) with the tracking system. Axis orientation can be calculated by placing the needle axis on the chamfer and rotating the shaft (as shown in Figure 1b) while performing a set of measurements (rotations and translations of the dynamic reference) with the tracking system. Such measurements can then be optimized to find the common point representing the tip as well as to find the axis direction. With calibration units, the complete needle pose can be directly obtained by transferring the construction data (e.g. well known location of guiding hole obtained from computerized numerical control machines, or CNC-machines, Figure 1c) from the calibration unit coordinate system to the needle dynamic reference coordinate system after performing a set of measurements with the tracking system.

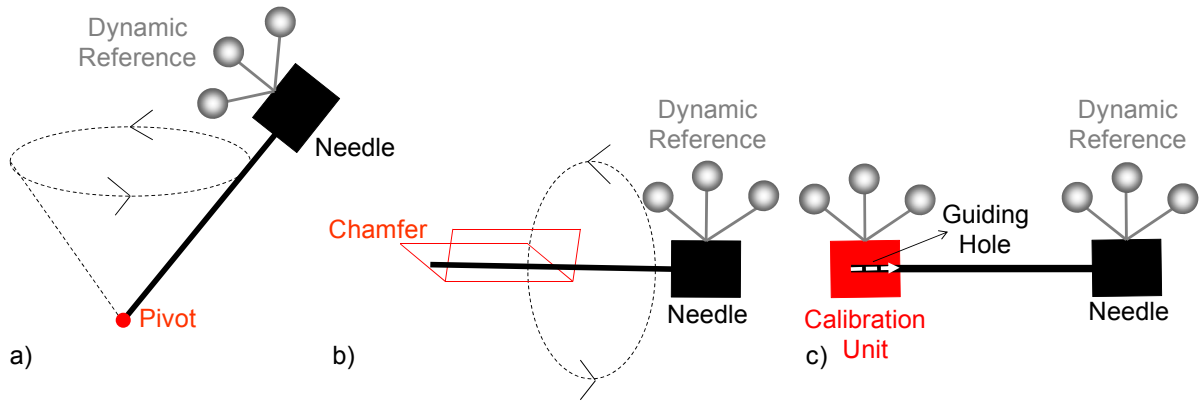

Figure 12: Needle calibration methods. a) Pivot for calculating tip location. b) Chamfer for calculating axis orientation. c) Calibration unit for calculating tip location and axis orientation by means of a guiding hole.

Most navigation systems for percutaneous intervention presented in the literature do not consider or do not differ between lesions located in bone or in soft tissue. However, such differences might influence the design of the needle being navigated as well as the outcome of the overall procedure [70]. As mentioned in the introduction, bone lesions are reached with a combination of cannula plus trocar to puncture through soft tissue, and cannula plus drill to penetrate the bone. The systems presented so far however, typically track the tip or shaft of the cannula and trocar pair. Shaft tracking is usually more flexible to the type of needle being tracked allowing either trocar or cannula tracking, whereas tip tracking is fixed to the tracking of the trocar because of the coil that needs to be embed in to the trocar tip. Drill tip tracking is usually difficult due to the design of some drills, e.g. hollow drills. Information about the drill orientation can be alternatively obtained by tracking the shaft of the cannula, although drill depth information is not available. Such limitations impose on the use of shaft tracking during percutaneous interventions with the target located inside bones.

2.3.2 Patient Tracking

Like instrument tracking, patient tracking provides referencing to the patient's anatomy within a tracked, or navigated, space. Such referencing is necessary in order to compensate for any patient or tracking system movements during the intervention. In surgeries performed on rigid structures like bone, patient tracking is typically performed by attaching a dynamic reference on the aimed structure. However, the non-rigid nature of percutaneous needle interventions introduces additional challenges that need to be considered. During soft tissue interventions, the anatomy of the patient can change considerably because of factors like breathing and patient movements. Therefore, the state of the patient during the image acquisition might not remain static throughout the entire intervention, and can be seen as a deformation of the imaged scenario. Such changes might lead to an incorrect patient referencing and that will have to be addressed by navigation systems.

Trying to provide reference to the patient, research groups have adopted two main approaches, rigid and non-rigid tracking. In the first, the patient is assumed to be rigid and is therefore tracked by a rigid dynamic reference like in neurologic and orthopaedic interventions. In the second, the deformable region surrounding the intervention area is tracked by many individual references which can move independently and represent different portions of the patient's anatomy. In order to have a more accurate assumption of a rigid patient, Nagel *et al.* [71] and Kenngott *et al.* [72] have proposed the immobilization of the patient by means of a vacuum mattress (see Figure 13 for an schematic). With the patient immobilized the combined patient, vacuum mattress and table could be tracked as one rigid structure.

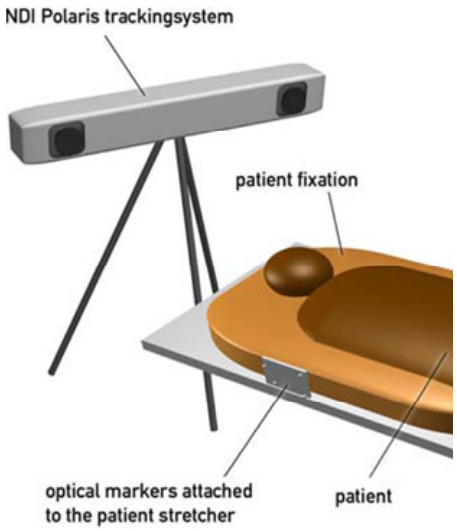

Figure 13: Illustration of a patient fixation and rigid tracking setup. The patient is immobilized with a vacuum mattress and tracked by a dynamic reference (optical markers) attached to the patient stretcher (Source: [72], image was cropped to emphasise the fixation and tracking devices).

Some other groups [60, 73] have also tracked the patient by attaching a rigid dynamic reference directly on the patient skin (see Figure 14a). This technique, though effective for targeting regions not affected by breathing (like pelvis for example), still does not allow detection of deformation for regions like chest and abdomens. To overcome these problems, the IRCAD have proposed to track the patient through a set of radio-opaque markers attached to the patient's skin [34, 37] (see Figure 14b). Their system can recognize the markers on the skin from video images, and calculate the current patient pose based on the 3D position of the markers. The set of marker positions can later be used for deformation detection (explained in details in the subsequent section). Tracking based on flat patterns suffers, however, from limited visibility angle. Similar patient tracking approaches based on electromagnetic tracking, have been reported by Appelbaum *et al.* [63]. Electromagnetic coils embedded in three patches placed on the patient skin provide information about the area surrounding the target. With a more invasive approach, the DKFZ group proposed patient referencing though a combination of internal and external markers [54, 56, 57] (see Figure 14c). The internal marker locations are obtained by attaching needles (so called reference aids) close to the target area (e.g. a tumour in the liver). Such a system advantageously provides information from within the vicinity of the target, however it requires another level of invasiveness that is not always accepted in the intervention. Other groups have also investigated the use of laser scanners [74] and time-of-flight cameras [75] in order to obtain denser data with a complete surface tracking. However, such equipment increases the necessary hardware in the intervention room and is either cumbersome and slow (not real time), or not accurate enough.

a)

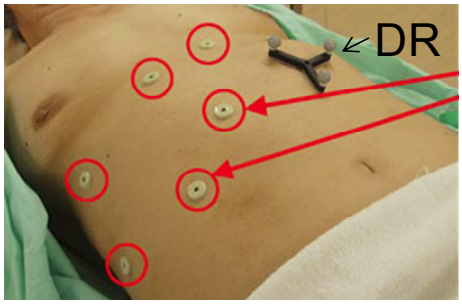

b)

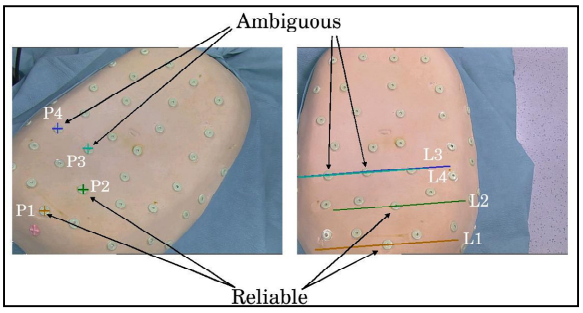

c)

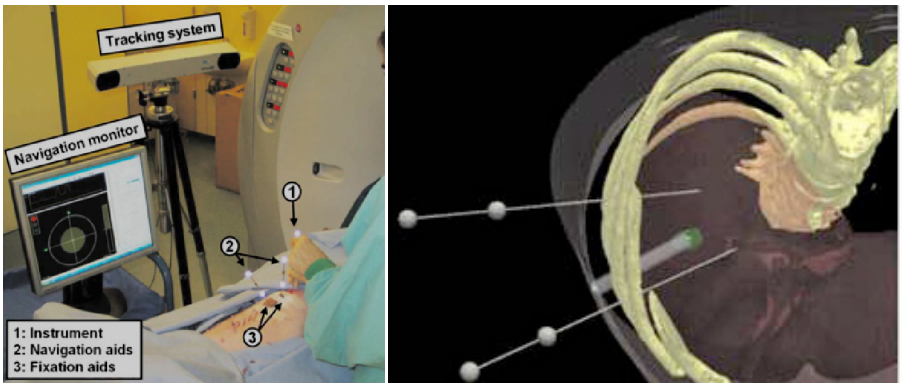

Figure 14: a) Patient tracking by means of rigid dynamic reference (DR) (Source: [60]). b) Patient tracking by means of radio-opaque marker detected from video images (Source: [37]). The pair of images correspond to one frame of the stereo camera. It shows one pair of reliable marker detection and one pair of ambiguous detection. c) Patient tracking by means of navigation aids (left) and virtual 3D view showing the navigation aids in the liver (right) (Source: [54]).

2.4 Patient-to-Image Registration

After establishing means of referencing the instrument and patient, their poses (${}^{pms}T_{idr}$ and ${}^{pms}T_{pdr}$ respectively) can be continuously estimated within a navigated space. Nevertheless, the correspondence between points within the navigated space and the image space still needs to be established in order to be able to co-display instruments and patient image data within a common coordinate system. Therefore, a registration between the patient and the image data has to be performed in order to obtain the transformation (${}^{img}R_{pdr}$) which maps points from the patient coordinate system to the image coordinate system. To enable such registration, corresponding fiducials markers, anatomical landmarks, or regions have to be located in both the patient and the image.

The most common method for aligning patient and image coordinate systems bases the registration on fiducial markers attached to the skin [38, 39, 42, 64]. The fiducials can be manually defined in the image and measured in the navigated space using the tip of the calibrated needle [64]. Variations of this method can reduce the required interaction by providing a fully automatic registration, as for example presented by the IRCAD group in [37]. Their system automatically identifies the fiducials in the CT images and in the video frames thus requiring no interaction of the physician with the system.

Primarily, two types of registrations are used to estimate the transformation, ${}^{img}R_{pdr}$: rigid and non-rigid. The rigid method simply calculates the rotation and the translation that best aligns two sets of corresponding fiducials, landmarks or regions (for example by using a least-square fitting [76]). The non-rigid approach on the other hand estimates a rigid transformation between the two spaces and later corrects discrepancies with non-rigid methods. The non-rigid registration provides means of extrapolating the location of anatomical regions surrounding the fiducials used for registration. In other words, it predicts possible patient deformations in regards to the imaged scenario. However, in order to obtain representative estimations, this approach demands denser information such as point clouds obtained from bulky surface scanners. In addition, it requires computational expensive finite element models that cannot be computed in real time [74].

In order to achieve a real time visualization without losing information about soft tissue deformation, the IRCAD group have combined rigid registration with tracking of the fiducial markers to provide gated intervention [53]. With their approach, the 3D location of the markers is continuously registered with the CT image and the registration error is used as a measure of deformation. Trying to take advantage of the information at the target vicinity which is provided by their patient tracker method, the DKFZ group employed simpler non-rigid registration methods (affine or thin plate spline) [57] to predict possible target motion caused by tissue deformation. Although their results showed that such methods can outperform rigid registration during continuous breathing motion, they also showed no improvement when simulating gated intervention at full expiration.

2.5 Visualization

Visualization is the part of the navigation system responsible for providing feedback of the physician's actions during planning and instrument guidance. In navigated percutaneous needle intervention, the planning is typically accomplished by defining a needle trajectory comprised of a target and a needle entry point, while the instrument guidance is accomplished by keeping the needle, tip and axis, as close as possible to the planned trajectory. Because physicians have already established method and tools for browsing through medical image data, navigation systems try to keep the visual feedback provided during planning similar to standard planar medical viewers [77] (see Figure 15 for an example). Instrument guidance on the other hand introduces new visualization concepts to physicians. Therefore, it requires the development of new, intuitive and effective guidance information. These aspects have been a subject of investigation and are discussed below.

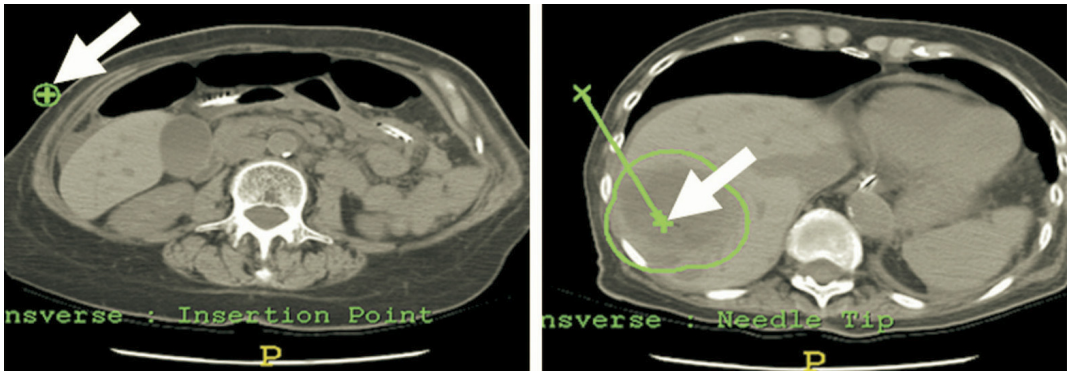

Figure 15: Planning of an entry point for the needle (left) and a target location (right) for radio-frequency ablation (Source: [77]).

The common approach for presenting needle guidance information that aids in the execution of a planned trajectory is to show a "targeting view" from the planned entry point looking to the target in which the user has to align the needle tip and orientation, such as presented in [42, 78] and illustrated in Figure 16a and b. In order to quantify the relevance of different visualization methods, the DKFZ group [79] developed and compared four visualization schemas including a projection view that is similar to the approach described above (see Figure 16c). Their results suggested that visualization methods following the concepts of the projection view are essential to a correct needle placement. Additional supporting views (e.g. off-sagittal and off-axial views showed in the top-right and bottom-left of Figure 16b respectively) have been also proposed to aid visualization of the area surrounding the needle [78] (see Figure 16b). However, the use of additional supporting visualization changes according to the medical application. With an alternative solution, the IRCAD group have proposed an augmented reality based visualization method [34–36, 36, 37, 52] to increase intuitiveness of the intervention. Virtual guidance information was overlaid on video frames to provide physicians with real patient images containing augmented virtual information. Although the feeling of visualizing a real scene could be achieved, there was still a need for sight diversion between the patient and the display that forces physicians to focus attention away from the patient. Techniques based on head mounted devices and semi-transparent displays, such as in Figure 11, give the illusion of navigation data floating within the underlying patient avoiding therefore, the need for sight diversion. Nonetheless, the

need for obtrusive equipment around the surgical scene and the associated limited workspace, long setup times and complex calibrations prevented the widespread use of the approach.

a)

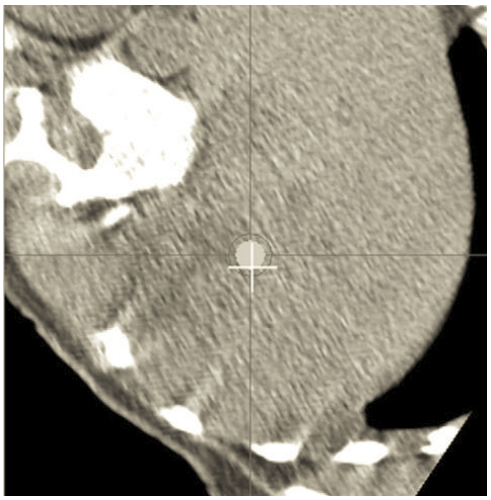

b)

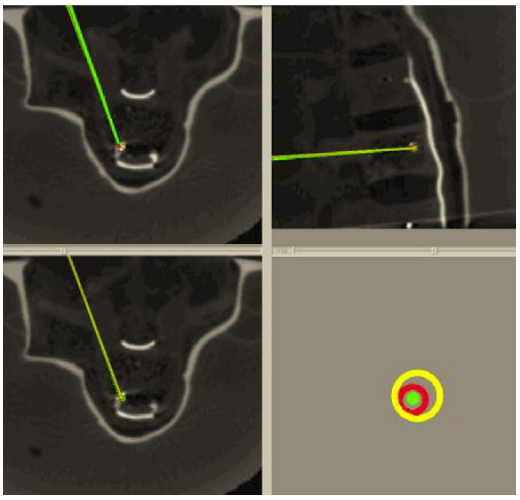

c)

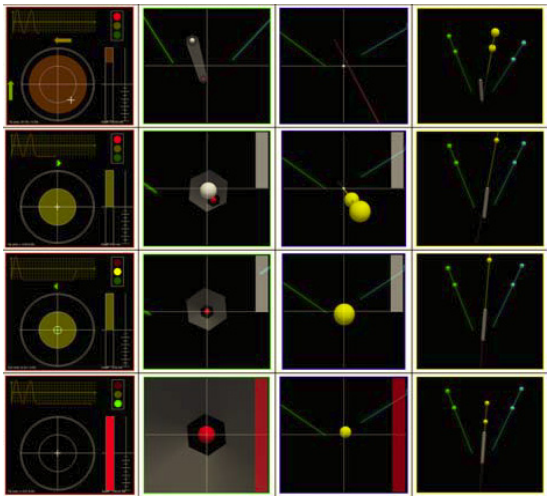

d)

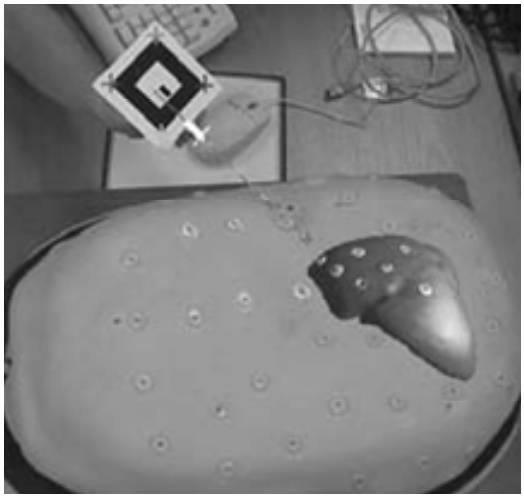

Figure 16: Instrument guidance viewers. a) Needle angle and position relative to the target site displayed as circle and cross in the middle on the cross-hair (Source: [42]). b) Axial view (top-left), off-sagittal view (top-right), off-axial (bottom-left), and targeting view (bottom-right) (Source: [78]). c) States of a targeting process evaluated by the DKFZ group (Source: [79]). Insertion point reached (first row), needle aligned (second row), needle insertion started (third row), target point reached (forth row). d) Augmented reality view displaying the 3D reconstruction of the liver and the virtual needle on the top of a video frame (Source: [35]).

3 Current Deficits

Brief: In this section, deficits with the state of the art approaches for image guidance are identified and summarized.

From within the previously presented state of the art review, deficits in current approaches to image guided percutaneous interventions could be identified. A summary of these deficits is presented below.

D1 - Deficits in image guidance for interventions based on nuclear images: The integration of multimodal nuclear images with image guidance is a relatively new concept and reports evaluating the proposed approaches are still very recent. Clinical workflow as well as data interaction and manipulation need further evaluation within a clinical context of oncologic interventions based on nuclear datasets such as PET. Current proposed approaches are based on electromagnetic tracking that imposes different types of constraints on workflow and interaction. To date, multimodal solutions based on optical tracking are still not available. In the image registration field, standard registration methods have been used to co-register pre- to intra-interventional data. In case of target displacement however, differences in the images being registered (e.g. presence of the puncturing needle and its metal artefacts) might affect the accuracy of such algorithms. Additional limitations in time availability and anatomical information hamper target displacement correction during PET/CT based interventions by means of standard registration approaches.

D2 - Deficits in approaches to puncturing hard tissue: To date, very few systems have considered percutaneous interventions aiming lesions located in bony tissue. Most of them make no distinction between soft tissue and bone, or do not even treat such cases. Although both punctures types rely on a precise needle placement, they follow different clinical protocols and demand image guidance systems to treat them differently. Current systems rely on needle tip tracking that is not suitable for bone interventions due to the need for embedded coils in the instrument. Therefore, the use of such approaches with standard and well accepted biopsy kits (e.g. the one illustrated in Figure 5) is limited.

D3 - Deficits in patient referencing robust to deformation: Effective and clinically acceptable approaches for patient tracking have been presented for rigid parts of the anatomy by using patient immobilization techniques and rigid dynamic references. Many of the first navigation systems for percutaneous interventions base the referencing of the patient on such techniques and have demonstrated to be efficient for rigid parts of the human anatomy. However, when considering motion factors like breathing or patient movement, more advanced methods are demanded. Currently investigated approaches usually depend on the type of tracking system used and present tradeoffs between reliability and computational efficiency on one side, and level of details and invasiveness on the other side. Complex setups and limitations on the usability were also important factors hindering acceptance of the reported approaches for tracking non-rigid portions of the patient's anatomy.

D4 - Deficits in patient-to-image registration under deformation: Initially, navigation systems for percutaneous needle interventions were based on manual rigid registration which required extensive physician interaction. Such systems could not provide information about deformation and required an increased time to manually register the patient. Later systems provide automatic registration methods and techniques to quantify or to compensate the presence of deformation. Deformation quantification is typically used to allow identification of the patient's state for gating procedures, and deformation compensation is used to directly estimate the current state of the patient. Available computer hardware and non-rigid registration methods limit state of the art approaches to non real time applications. Real time deformation quantification for gated procedures has shown potential within clinics, but currently available approaches are either invasive or require complex hardware and increased setup time.

D5 - Deficits in visualization without sight diversion: Many graphical concepts for presenting guidance data have been proposed and investigated over the years. Some of them like targeting viewers have been widely evaluated and are currently well accepted. However, available clinically applicable visualization hardware present guidance information on monitors requiring sight diversion from the patient. Alternative visualization approaches have tried to overcome these problem, but challenges with obtrusive hardware, limited workspace, long setup times and complex calibrations have hindered their clinical acceptance. To date, there is no clinically established solution for needle guidance visualization that can overcome such deficiency.

4 Aims and Approaches

Brief: In this section, the aims and approaches proposed in this thesis are presented. The methodology of research is also presented here.

Deficits in the state of the art image guidance methods hinder a more flexible and more reliable procedure. Improving the state of the art image guidance methods can enhance quality of the percutaneous needle interventions. The aim of this thesis is to address the deficits listed in the last chapter by presenting a respective improved approach for each of them, see list below.

A1 - Image guidance for PET/CT interventions: An image guidance approach supporting intra-interventional multimodal image data manipulation and handling is presented. A navigation system incorporating viewers for multimodal data interaction and visualization was developed in order to evaluate the workflow of oncologic procedures based on nuclear images. Additionally, an image registration pipeline for automatic correction of target displacement during PET/CT interventions was implemented. The registration pipeline is capable of: extracting the bone of interest without the needle and therefore turning the registration scenario into a rigid problem; registering a control CT with the reference CT; and finally, correcting the PET target location inside the bone. Pre clinical PET/CT experiments with swine cadavers showed that the presented method overcomes limitations of the standard clinical approach while respecting clinical routine constraints. Results also confirmed the feasibility of clinically using the registration pipeline for target correction in bone interventions.

A2 - Image guidance supporting bone and soft tissue puncture: An image guidance approach to aid punctures aiming targets located in bone and in soft tissue is presented. Viewers and workflow supporting clinical protocols of bone and soft tissue punctures have been developed. Additionally, clamps and dynamic references have been developed to enable needle shaft tracking. Calibration devices and methods for reducing physician and system interaction during intervention have also been presented. Evaluation performed on a set of swine cadavers has shown: that sufficient accuracy could be achieved for both types of punctures when using the presented viewers, that needle preparation and calibration could be performed effectively without increasing the intervention time, and that the clinical constraints (e.g. sterility phases and areas) for both protocols were respected with the image guidance workflow adopted.

A3 - Anatomy tracking for motion and deformation detection: A real time patient tracking approach based on market available optical tracking systems and on retro-reflective markers attached to the patient's skin is presented. The approach comprises a tracking algorithm that relies on a set of 3D positions measured by the optical tracking system. Once the single markers are placed on the patient's skin, the tracking algorithm can be initialized by defining the initial configuration of the single markers (i.e. non deformed state). After the tracking algorithm initialization, the patient's skin is continuously tracked throughout the intervention via the single markers. Our results have shown that the presented tracking approach is robust to several conditions faced in the intervention room including patient deformation, presence of unexpected markers as well as partial and temporary total single marker set occlusion.

A4 - Automatic patient-to-image registration with deformation identification: An automatic patient-to-image registration approach enabling gated intervention is presented. The approach performs a rigid registration between the current single marker set configuration and their initial configuration in the image to estimate the pose of the patient. The fiducial registration error is thereafter used for identifying the presence of deformation allowing physicians to gate the procedure. In order to reduce the interaction between physicians and the system, the single markers are automatically identified in the CT images and used to initialize the patient tracking algorithm. Results of experiments performed in a

laboratory setup showed that: the deformation information provided by the presented method is sufficient to enable gated procedures, and the single markers can be correctly identified in the CT images.

A5 - Projection of needle guidance data on patient: An augmented reality visualization approach that eliminates the need for sight diversion from the intervention area is presented. The approach comprises a portable image overlay projector. The projector is integrated as a tracked tool (a case with a dynamic reference) in the image guidance system in order to project needle guidance information directly on the patient's skin. The projector is portable, non obtrusive, and easily integrated (plug and play). Calibration to calculate the projector orientation regarding to its dynamic reference is only required once. Laboratory experiments proved the versatility and applicability of the presented approach that addressed many of the deficiencies of previously described augmented reality approaches.

Incremental and interactive research was used in this project in order to increase the communication with the clinics during the development of each method and to guarantee the clinical usability of the final outcome. In a first step, an image guidance system has been developed and used to evaluate the two first approaches, A1 and A2, within a static scenario. Subsequently, the system was augmented with means to cope with deformation and used to evaluate approaches A3 and A4 in a dynamic scenario. Finally, the augmented reality visualization approach, A6, was integrated in the system in order to evaluate new means of image guidance visualization. The collection of requirements and evaluation were performed closely together with clinical partners taking into account daily clinical routine and environment. The first two approaches addressing the issues with multimodality and different types of tissue puncture (A1 and A2) are presented in chapter 5 (Image Guidance for Multimodal Percutaneous Interventions). The two following approaches addressing problems related to patient deformation (A3 and A4) are presented in chapter 6 (Tracking of Non-Rigid Anatomical Structures). The final approach addressing problems related to the need for sight diversion during image guided interventions is presented in chapter 7 (Projection of Needle Guidance Data on Patient). The diagram in Figure 17 illustrates the relationship between the deficits found in the literature and the approaches presented in this thesis.

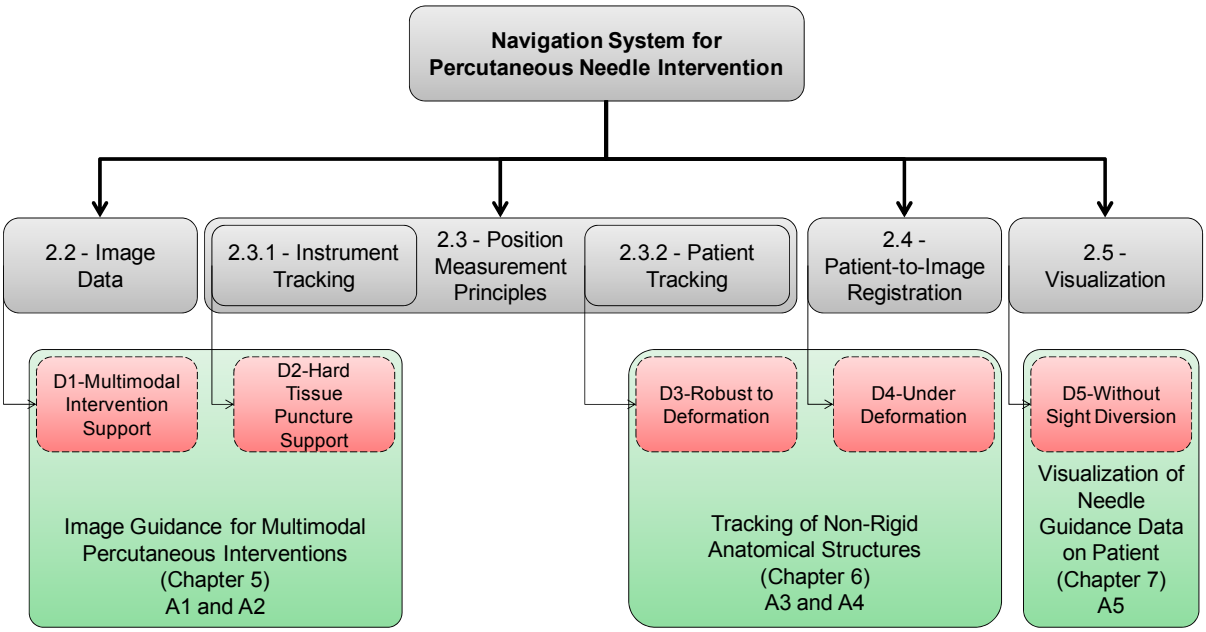

Figure 17: Diagram relating the deficits (red) of the state of the art approaches for image guidance of percutaneous needle interventions based on multimodal images and the respective improved approaches proposed in this thesis (green).

5 Image Guidance for Multimodal Percutaneous Interventions

Brief: This chapter presents a navigation system for percutaneous needle interventions with support to multimodal images. The design and workflow of the system for PET/CT based interventions is presented in section 5.1. The system supports interventions aiming lesions located in soft tissue and bone, and has been evaluated with a set of experiments performed in swine cadavers. Section 5.2 proposes a pipeline for local bone registration as a solution for target displacement during bone punctures. Section 5.3 presents an analysis of the requirements and workflow for percutaneous nephrolithotomy interventions to ensure the developed system can also handle other types of percutaneous applications. Finally, section 5.4 presents a clinical biopsy case performed with the system in order to evaluate some of the presented methods within a clinical scenario.

5.1 A PET/CT Based System for Soft Tissue and Bone Punctures

The work presented in this section was published in: T. Oliveira-Santos, B. Klaeser, T. Weitzel, T. Krause, L. Nolte, M. Peterhans, S. Weber, "A navigation system for percutaneous needle interventions based on PET/CT images: Design, workflow and error analysis of soft tissue and bone punctures", Computer Aided Surgery, September 2011; 16(5): 203–219. ***Copyright © 2011 Informa Heathcare****. Computer Aided Surgery is available online at:*
http://www.informaworld.com/doi/abs/10.3109/10929088.2011.597566

Abstract. Percutaneous needle intervention based on PET/CT images is effective, however it exposes the patient to unnecessary radiation due to the increased number of required CT scans. Computer-assisted intervention can reduce the number of necessary scans but requires handling, matching and visualization of two different datasets. While one dataset is used for target definition according to metabolism, the other is used for instrument guidance according to anatomical structures. Navigation systems capable of handling such data and performing PET/CT image based procedures while following clinically approved protocols for oncologic percutaneous interventions are not available. The need for such systems is emphasized within scenarios where the target can be located in different types of tissue such as bone and soft tissue. These two tissues require different clinical protocols for puncturing and therefore might raise different problems during the navigated intervention. Studies comparing the performance of navigated needle interventions targeting lesions located in these two types of tissues are not often found in the literature. Hence, this paper presents an optical navigation system for percutaneous needle interventions based on PET/CT images. The system provides viewers for guiding the physician to the target with real time visualization of PET/CT datasets and is able to handle target located in both bone and soft tissue. The navigation system and the required clinical workflow were designed considering clinical protocols and requirements, and the system is thus operable by a single person even during transition to the sterile phase. Both, the system and workflow were evaluated in an

initial set of experiments simulating 41 lesions (23 located in bone tissue and 18 located in soft tissue) in swine cadavers. We also measured and decomposed the overall system error into distinct error sources, which allowed for the identification of particularities involved in the process as well as highlighted the differences between bone and soft tissue punctures. An overall average error of 4.23 mm and 3.07 mm, for bone and soft tissue punctures respectively, demonstrated the feasibility of using this system for such interventions. The proposed system workflow showed to be effective in separating the preparation from the sterile phase as well as in keeping the system manageable by a single operator. Among the distinct error sources, the user error based on the systems accuracy (defined as the distance from planned target to the actual needle tip) appeared to be the most significant. Bone punctures showed higher user error, whereas soft tissue punctures showed higher tissue deformation error.

5.1.1 Introduction

Percutaneous needle interventions (i.e. biopsy, wire marking, radio frequency ablation, etc) are widely used in medicine as minimally invasive alternatives to open surgical interventions. Such procedures are typically performed based on structural volumetric datasets, as for example computed tomography (CT) and magnetic resonance imaging (MRI). However, medical imaging has changed fundamentally with the introduction of functional modalities such as Single Photon Emission Computed Tomography (SPECT) and Positron Emission Tomography (PET). By using combinations of structural and functional modalities (SPECT/CT and PET/CT), image understanding and therefore diagnosis can be optimized [11, 12]. With these techniques even suspicious lesions without morphological correlation, i.e. not evident in structural datasets, can be identified and verified histologically [14]. In multimodal image interventions, the functional image (e.g. PET and SPECT) provides information about the target, while the structural image (e.g. CT, MRI, etc.) provides anatomical information for geometric instrument guidance. Such procedures can be performed using a step-by-step technique (similar to CT guided interventions). Currently, the intervention is planned based on a reference image comprising a single-bed PET/CT acquisition of the patient already positioned for needle intervention. This reference CT includes a reference grid placed on the patient's skin that is used to facilitate the guidance of the needle (i.e. cannula with appropriate puncturing instrument) to the lesion. After identifying the grid and the lesion in the reference dataset, the needle is, then, oriented and introduced in small steps. Each step is alternated with control CT acquisitions to ascertain the needle current position and orientation in respect to the grid. The control scans are performed until the target is reached. In case of bone punctures, the trocar (i.e. sharply pointed end instrument that fits in the cannula and used to puncture soft tissue) is replaced by a drill (i.e. drilling instrument that fits in the cannula and used to penetrate the bone) as soon as the needle reaches the bone surface, allowing the physician to drill to the target. The depth of the drill is controlled with the help of distance holders (provided with the drilling kit) which assists in the prevention of drilling deeper than a specified value. Though effective, the step-by-step approach requires excessive control CT scans and lacks a registration between patient and image datasets that must then be mentally performed by the clinician. In consequence, the radiation burden to the patient is increased, as well as the procedure time.

Stereotactic instrument guidance is a technique used to provide increased procedural accuracy in anatomical areas that cannot be directly viewed by the human eye. It relies on the position-sensing of instruments and a known patient anatomy inside a navigated space in order to co-display virtual models of the instruments in a context of registered medical image datasets. The general principles of this technique were described in [27] and [28], and have been applied to different clinical areas. Today, navigation systems rely mainly on two different tracking technologies, optical and magnetic, to track or estimate the pose of a dynamic reference (DR) in space. A comparison between the two methodologies [51] shows that optical methods present higher accuracy, but require a continuous line of sight between the tracked instruments and the camera. Alternatively, the electromagnetic tracking does not require line of sight, but has lower accuracy and requires a wired connection to the tracked instruments. Moreover, the later method is sensitive to ferromagnetic material present in the tracking environment and is therefore less robust than the first. In the area of needle guidance applications, many navigation systems were developed to solve specific clinical problems, such as: liver puncture [52, 56], vertebroplasty procedures [33], as well as general biopsy procedures [39, 42]. While some of these groups [39, 42, 63] rely on well established rigid approaches for registering the patient to the

image and therefore are limited to target static anatomical regions; other groups investigate non-rigid methods to gate breathing [52] or to model deformation [56] in order to target organs that can considerably deform during the procedure. A recent review performed by Cleary and Peters [30] shows that even though non-rigid methods are making progress for interventions of the thorax and abdomen, but most of the current work is still based on the rigid approach. Regardless of the method used, systems for interventions based on PET/CT images, which require manipulation and real time visualization of multimodal datasets, are still unavailable. In order to address this problem, Militz *et al.* [43] demonstrated that needle guidance using multimodal datasets is feasible with standard commercial navigation systems, although manipulation of such images and operational flexibility is decreased. Other groups also reported multimodal approaches using combinations of pre- and intra-procedural image datasets for needle guidance [44, 45]. Phantom experiments have demonstrated the feasibility of using such navigation systems with multimodal images. However, handling of multiple acquisitions of structural images as well as different sets of metabolic images while following clinically approved protocols for oncologic needle interventions, such as [14], still demand investigation. Additionally, most of the presented systems do not clearly distinguish between lesions located in bone or soft tissue. Each puncture type follows a different clinical protocol and therefore cannot be treated equally by the navigation system, especially due to the challenge of navigating the drill in case of bone lesion. Integration of a DR into the drill can be difficult considering their shape and functionality. Consequently, when lesions are located in soft tissue, the needle can be guided to the target, whereas for lesions located in bony tissue, the needle guidance can only be used until the bone surface. Thereafter, the orientation of the drill is known due to the tracked cannula; however, no information about the depth of the drill is provided. The distinct requirements of each puncture type might change the relevance of the error sources as well as the outcome associated with each of lesion type. Studies comparing results of navigation systems dealing with these two types of punctures are still needed.

To address these problems, we have developed an optical navigation system for percutaneous needle interventions based on PET/CT images, which can handle multiple datasets as well as both types of punctures and which follows clinically approved protocols. The system software provides viewers for guiding the physician to the target with real time visualization of PET/CT datasets, and for estimation of the final drill position in case of bone interventions. In addition, the system workflow is compatible with standard clinical protocols for needle interventions, and thus does not increase setup time or personnel as the system is operable by a single person even during transition to the sterile phase. The preliminary version of this system, as presented in this paper, was designed to target static anatomical regions (not affected by breathing, e.g. pelvic region). Therefore, it could be evaluated within an initial set of pre-clinical experiments of simulated soft tissue and bone lesions in swine cadavers. Herein, we present a detailed description of the system design, workflow and evaluation methods. Finally, we present an analysis of the system accuracy based on an error decomposition approach, which enables us to investigate the different steps involved in the process and the particularities related to soft tissue and bone punctures.

5.1.2 Material and Methods

A navigation system for percutaneous needle intervention based on PET/CT images and the workflow necessary for navigated interventions aiming bony and soft tissues were designed. In order to quantify error sources involved in the navigation process, a series of experiments involving bone and soft tissue punctures based on PET and CT modalities were performed in animal cadavers. A detailed description of the system along with the performed validation experiments can be found in the following sections.

System Description

The navigation system consists of a computer, an optical position sensor (NDI Vicra camera, Northern Digital Inc., Waterloo, Canada), two touch screens (and/or wireless mouse), a moveable cart, and a DR set. The later comprises a needle DR to be attached to the needle shaft (i.e. back part of the cannula) in order to provide a tracking reference to the actual needle, a patient DR to be attached to the patient skin in order to provide a tracking reference to the patient, as well as a calibration unit used to calibrate the needle tip and shaft positions in relation to the needle DR. In general, the navigation sys-

tem tracks the pose of each DR with the position sensor, and co-displays a model of the needle along with the PET/CT image by applying the set of transformations described in Figure 18. This technique provides the physician with visual feedback for instrument guidance assistance. The passive optical tracking technology chosen relies on infrared retro-reflective spheres to estimate the pose of each tracked DR and thus avoids wired connections to the tracked instruments. A set of clamps provides quick connections between a wide variety of needle shafts and the needle DR. The DR set and the clamps were manufactured in medical grade titanium and are therefore sterilisable.

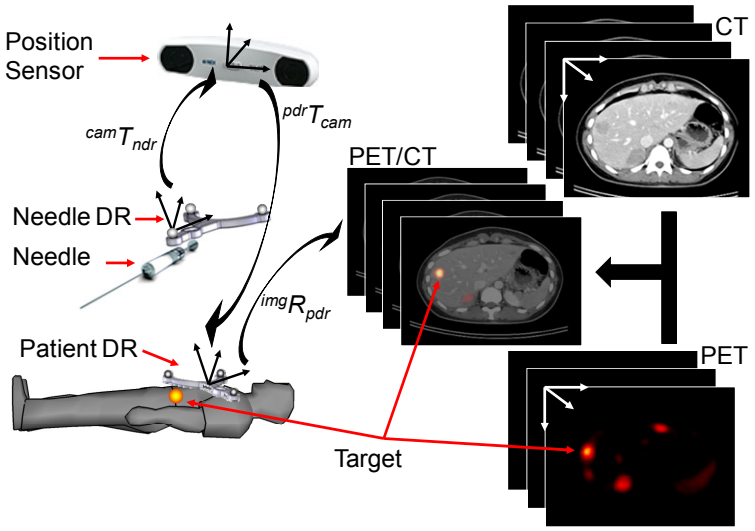

Figure 18: Navigation system overview. The transformations $^{cam}T_{ndr}$ and $^{pdr}T_{cam}$ are measured by the position sensor, whereas the $^{img}R_{pdr}$ is the patient-to-image registration.

The system software is divided in to three modules: *planning*, *calibration and registration*, and *instrument guidance*. Each module is described below.

Planning: Three standard PET/CT planar viewers (Coronal, Sagittal, and Axial) provide the same functionality used in clinical routine, and one 3D viewer (see Figure 19a) provides an overview of the procedure plan. Using the planar viewers, the user can precisely set the target location, and through the 3D viewer a needle entry point can be quickly chosen by selecting a position on the patient's skin. These two locations define the planned trajectory that can be verified on the trajectory viewer (Figure 19b). This viewer displays structures surrounding the planned path which helps in the localization of possible anatomical obstacles and critical structures. The patient DR pose is defined in the image coordinate system by selecting the centre of the retro-reflective spheres in the CT. With the aid of the 3D viewer for coarse definition and the planar viewers for fine definition, this procedure takes less than 1.5 minutes. After planning, the user gains visual access to the tracked DR set, and a 3D viewer provides information about the camera viewing volume so that the camera optimal position can be found prior to the intervention.

Calibration and registration: The calibration unit is used together with the specific needle calibration adaptor for calibrating the needle tip location and axis orientation with respect to the needle DR. The calibration is performed by acquiring a set of poses of both, the needle DR and the calibration unit, and by then transforming the average calibration vector (defined by the calibration unit construction data in the CNC-machine) to the needle DR (see Figure 19d). To reduce and simplify the software interaction, the calibration process triggers automatically, as soon as the calibration unit is shown to the position sensor in the calibration configuration (as in shown Figure 19d). The clamp used to attach the needle DR to the needle shaft defines a region of probable location of the needle. The system continuously verifies that this region matches the calibration vector of the calibration unit and triggers the start of the calibration procedure whenever such condition remains fulfilled for a couple of seconds. Thereafter, a set of poses for calibration is acquired. The calibration process is aborted when the user varies the position of the tip relative to the calibration vector during the pose acquisitions. After needle calibration, the patient-to-image registration $^{img}R_{pdr}$ is automatically calculated (as described in [76]) once the patient DR is visible. This transformation maps the position of the patient DR spheres de-

tected by the position sensor to their pre-defined positions in the CT image, described above in planning. The whole process takes approximately 10s.

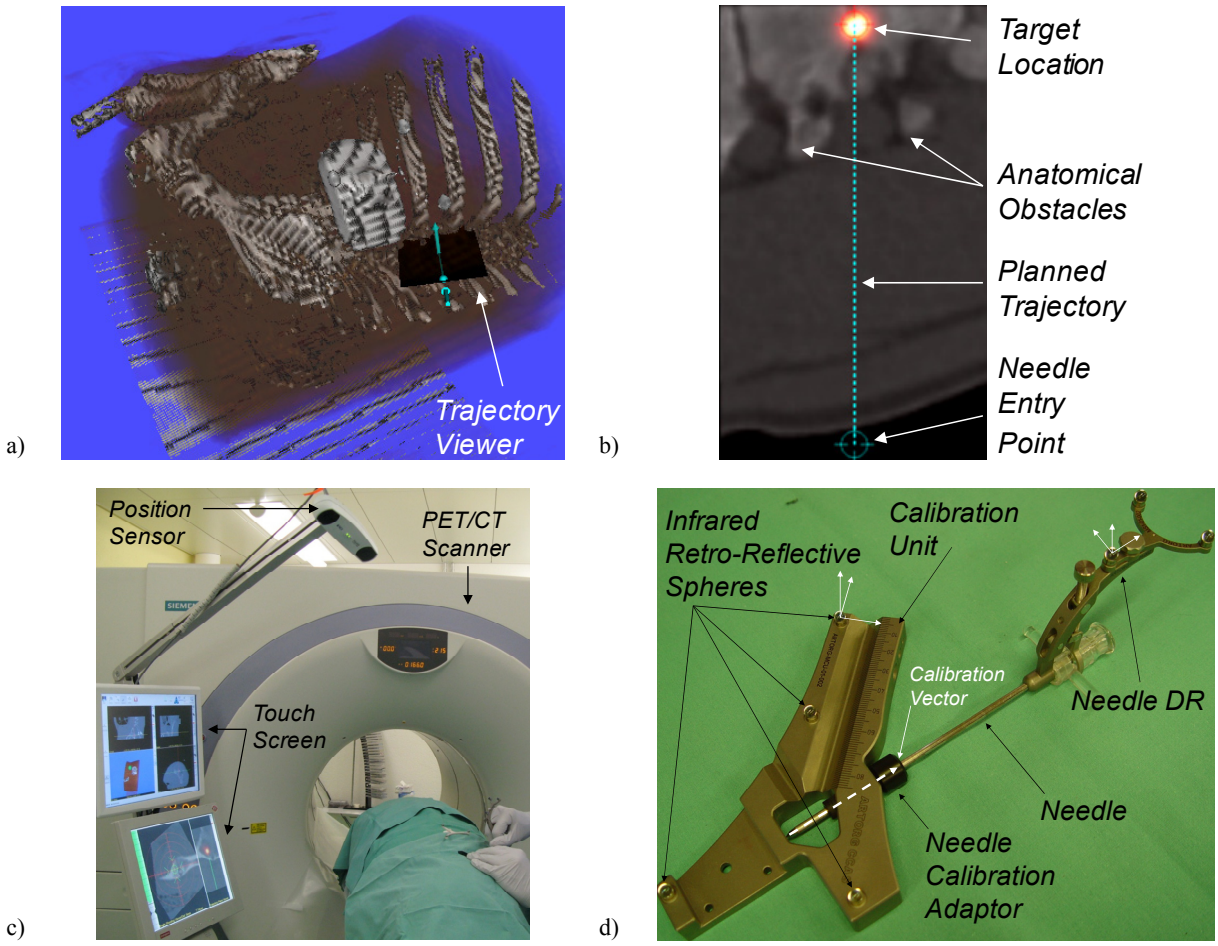

Figure 19: a) 3D viewer showing an overview of the planned situation and the orientation of the trajectory viewer. b) Trajectory viewer showing the planned trajectory and possible obstacles. c) Navigation platform beside the PET/CT scanner table. d) Needle and calibration unit in calibration position.

Instrument guidance: Three main viewers; the 3D viewer, the targeting viewer and the needle plane viewer, provide visual information to help guide the needle to the target according to the planned trajectory. The 3D viewer (similar to Figure 19a, but also including the virtual needle) shows an overview of the intervention scenario which facilitates the localization of the planned needle entry point. The targeting viewer (see the schematic in Figure 20a and an example in Figure 21a) helps the user to align the needle with the planned trajectory and to navigate to the target. In addition, the viewer allows the physician to assess the risk to structures around the planned trajectory. The viewer also shows the needle tip and shaft within a crosshair aligned to the planned trajectory, in addition to the remaining distance to the target. The needle alignment with the planned trajectory is achieved by bringing both, tip and shaft to the centre of the crosshair. The needle plane viewer (see the schematic in Figure 20b and an example in Figure 21b) helps the user to foresee upcoming structures and to estimate the final position of the needle. It shows the virtual needle and its projection to the target on the PET/CT plane that is vertically aligned with the needle and horizontally parallel to the x axis of the needle DR. The needle projection displayed by this viewer is especially important for bone interventions, in which physicians can only navigate the trocar needle up to the bone surface having no further information about the drill tip depth while penetrating the bone. By combining the projection and the required drilling depth (i.e. distance from cannula tip to the target), the physician can estimate where the drill will end up after drilling the remaining distance.

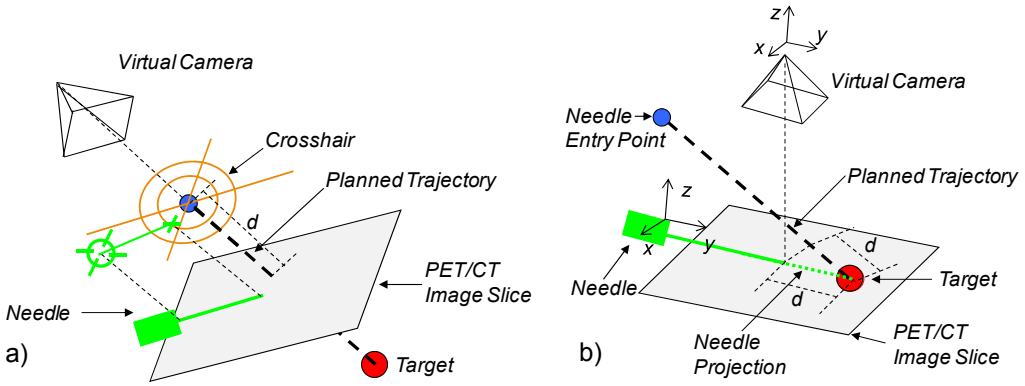

Figure 20: a) Shows the targeting viewer schematic. The virtual camera is aligned with the planned trajectory and looks to the target. The needle tip and the needle shaft are projected back to the crosshair plane, and are respectively displayed as a cross and a circle that is complementary to the cross. Both are connected through a line. The viewer background displays the fused PET/CT slice orthogonal to the planned trajectory at the depth of the needle tip d, or alternatively 10 mm beyond the tip, $d + 10$. b) Shows the needle plane viewer schematic. The virtual camera looks to the needle tip, has its y axis parallel to the needle and its x axis parallel to the cross product between the needle and the z axis of needle DR. The viewer background displays the PET/CT slice surrounding the needle axis. In order to aid the physician in predicting the final tip position if the needle continues in the current direction, a projection of the needle along the remaining distance d is displayed.

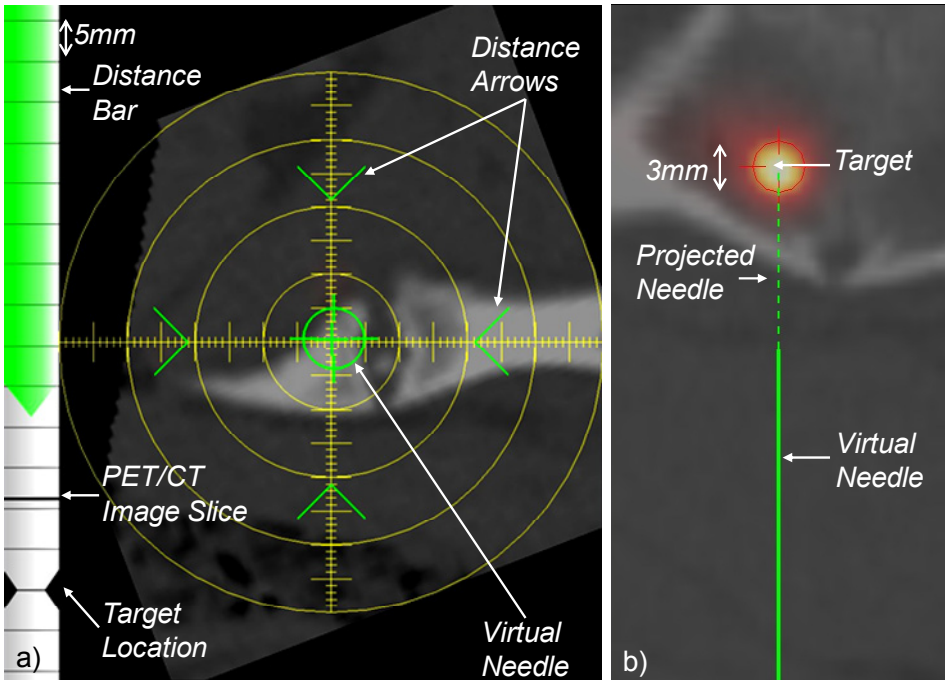

Figure 21: a) Shows the targeting viewer with the needle aligned with the planned trajectory and moving towards the target. The distance to the target is displayed in the left bar, and is also represented by the distance arrows approaching the centre of the cross hair target, which removes the necessity to deviate ones attention from the centre of the viewer. b) Shows the needle plane viewer displaying the needle, its projection to the target, and the PET/CT slice along the needle axis.

The system is setup inside the intervention room, beside the scanning table as shown in Figure 19c, and it is connected to the hospital network. A sterilized DR set is kept ready for use, in case a biopsy is required.

The system workflow, like the standard non-navigated PET/CT intervention [14], begins after diagnoses and continues until the target is reached. The process is divided in two phases: non-sterile and sterile. The sterile phase commences at needle calibration (see Figure 22). The system software was designed such that there is no need for manual interaction with the mouse or touch screen during the

sterile phase, which allows the whole procedure to be performed by a single person. The individual steps can be described as follow:

Non-Sterile Phase:

- **Patient Preparation**. The patient is positioned, prepared and stabilized by means of a vacuum mattress on the scanner table, as presented in [71]. At this point in time, the lesion and the likely needle entry point positions are coarsely known by the physician, and therefore the patient DR can be placed near the intended target. This minimizes the effect of errors between the patient DR and the target such as the tracking error in the target (*TRE*), as described by Fitzpatrick *et al.* [80]. The physician is also advised to place the patient DR in regions not affected by respiration movement, which limits the system use to specific regions, e.g. pelvic region. The patient DR can be attached to the patient's skin by means of surgical tape, requiring no more time than the standard reference grid attachment. Lastly, the system cart is placed on the opposite side of the patient to the physician.
- **Image Acquisition**. A small PET/CT image volume including the patient DR and the potential lesion is acquired. The dataset is assumed co-registered, as provided by most currently available PET/CT scanners (e.g. Siemens Biograph 16 Hi-Rez).
- **Image Transfer:** The image is exported from the scanner station to the navigation system through the network. No additional time to that required for the normal export of data to a planning station is required by this step.
- **Planning**. The planned trajectory composed of planned target and needle entry point, as well as the patient DR spheres are precisely chosen using the viewers described in the planning module. As the final steps before entering the sterile phase, the physician aligns the monitor with the planned trajectory, and adjusts the camera to ensure that the patient DR and the needle will be visible during the entire intervention.

Sterile Phase:

- **Needle Calibration.** Based on the trajectory length, the appropriate needle length and strength are selected. The needle DR is clamped to the chosen needle's shaft, and the needle tip position and axis of orientation are calibrated relative to the needle DR.
- **Patient-to-Image Registration.** At this point, the patient is automatically registered to the image datasets in order to transform points from the patient anatomy to their corresponding position in the image dataset.
- **Instrument Guidance**. The physician, then, uses the visual feedback provided by the navigation system to steer the needle to the bone surface or target, in case of bone or soft tissue interventions respectively.
- **Bone Surface.** From this moment on, the trocar cannot continue because the target is placed inside the bone. Thus, the physician has to exchange the trocar for the drill.
- **Check Projection.** Using the needle projection provided by the needle plane viewer, the physician re-orients the drill to make sure it will hit the target. Subsequently, the missing distance is checked in order to determine the required drill depth. The navigation system has no information about the tip depth, thus the drill depth is controlled by the physician only.
- **Drill to Target.** Finally, the physician drills the missing distance towards the target.
- **Target Reached.** The physician decides whether the target was sufficiently reached, and finishes the procedure (i.e. takes a sample, places the marking wire, etc).

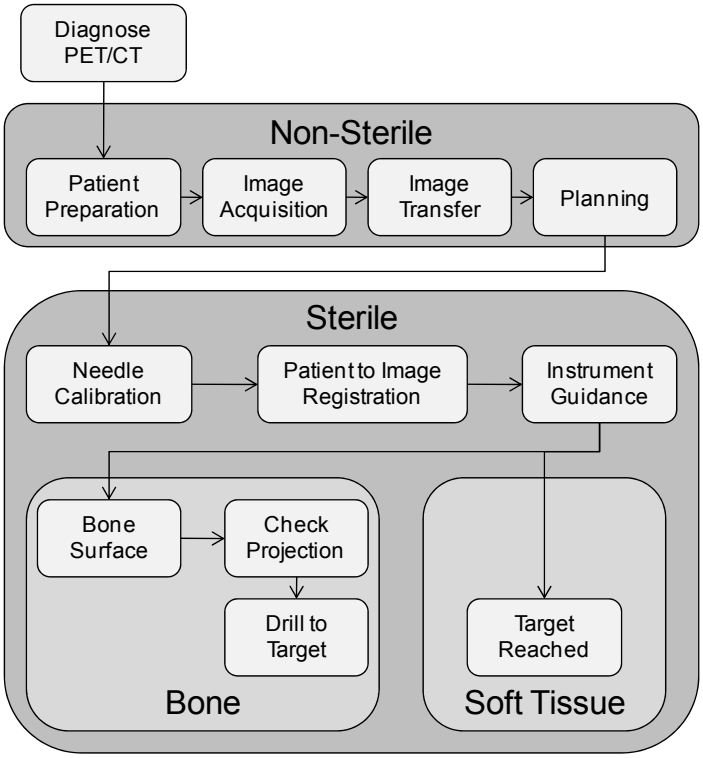

Figure 22: System workflow emphasizing the non-sterile and sterile phases, and the particularities of bone and soft tissue interventions.

Experiments Description

A navigated PET/CT pilot study using 4 swine cadavers (S1, S2, S3, and S4) prepared with radioactive spots (1 mm diameter cotton wool balls with ca. 0.5 MBq ^{18}F solution placed inside bone and soft tissue) was performed on site considering the constraints faced during daily clinical routine (e.g. available space, sterility phase, and available procedural time). The first two swine were used for the simulation of 23 bone punctures, while the last two were used for the simulation of 18 soft tissue punctures. The lesions were distributed along the swine anatomy, excluding legs and head.

Cadaver puncturing procedure: The animal was laid down on the scanner table and a set of punctures were performed according to the workflow described in section 0. In order to ensure the repeatability of the target definition during the validation phase, the radioactive spot in the PET modality was adjusted to about 5 mm diameter size (using the window/level functionality) and the target was defined by visually fitting a circle around it using the three views (coronal, sagittal and axial). During the instrument guidance step, the physician was asked to decide the final position of the needle. After releasing the needle, a final image acquisition (PET/CT) with the needle in place was then performed. In total, two datasets (each containing co-registered PET/CT) were obtained per puncture: a planning dataset used for planning the puncture and guiding the needle, and a validation dataset for checking the actual needle position. This process was repeated for every lesion.

Equipment: Image acquisition was accomplished with a Siemens Biograph 16 Hi-Rez with voxel size set to 1.37 × 1.37 × 1 mm and 2.67 × 2.67 × 2 mm (intrinsic spatial resolution of approximately 5 mm), for CT and PET respectively. Both image modalities share the same coordinate system and were acquired right after each other. To eliminate or at least to make insignificant the needle bending effect [65], a bone biopsy set with a coaxial needle of 3.4 mm outer diameter (10 G), 130 mm length and distance holder of 5 mm, and a soft tissue biopsy set with a coaxial needle of 2.1 mm outer diameter (14 G) and 145 mm length was chosen for this study. The drill used for bone punctures was the same during the whole experiment.

Error decomposition: A common way of reporting the accuracy of navigation systems for needle guidance is by presenting the achieved overall error, e_{ova}, i.e. the distance between the target to the needle tip in the validation dataset. Unfortunately, this measure does not provide detailed information about the accuracy of the different system components involved in the process. In order to better understand the system behaviour and to indentify its particularities when applied to bone and soft tissue, we decomposed the overall error in to individual sources. In this study, we divided the overall error in to the following sources: e_{pdr}, i.e. the error introduced by a patient DR movement, e_{tde}, i.e. the internal tissue deformation error, and e_{usy}, i.e. the user-system error. The first source, e_{pdr}, appears when the patient DR moves relatively to the target after the CT acquisition, which consequently causes a shift in the target as seen from the navigation system point of view. This error source has the same effect as the *TRE*. Nevertheless, it is conceptually different because *TRE* is defined as target shift caused by an inaccurate registration of a pair of points in a rigid structure containing the target. In this system however, the points (i.e. spheres in the patient DR) are not rigidly connected to the target. This may result in an e_{pdr} which is additional to the registration error. The second source, e_{tde}, is introduced by the interaction of the needle with the surrounding tissue [65], which also might cause a target shift not detected by the navigation system. The last source, e_{usy}, represents the user error based on the provided instrument and target tracking accuracy. The user error is determined by the physicians ability to define the patient DR spheres used for registration and to follow the guidance information provided by the system. The instrument and target tracking accuracy comprises the DR tracking accuracies achieved by the position sensor, calibration accuracy and the *TRE*, as defined in [80], after registering the spheres defined by the user. The relation of the overall error vector to these individual source vectors is illustrated in Figure 23 and is formulated as follows:

$$e_{usy} + e_{pdr} + e_{tde} = e_{ova} \tag{2}$$

Individual error sources measurement: In a second step, the datasets acquired during the punctures were post-processed to quantify components of the error involved in the process. The target was redefined in the validation dataset, as P_{vat}, and the planned target, P_{plt}, was projected from the planning dataset to the validation dataset. A simple projection of P_{plt} using the common machine coordinate system transformation, R_{mcs}, is not sufficient to transfer the planned target to the validation dataset because it does not consider a possible movement of the animal from the planning acquisition to the validation acquisition (e.g. due to the physician-animal interaction while puncturing, see Figure 23 for an illustrative example). Hence, P_{plt} was projected using a transformation, R_{rig}, based on a common reference within the body (assumed to be a rigid structure in the body, e.g. vertebra, see Figure 23). In order to project P_{plt} to the validation dataset as seen from the navigation system, a transformation, R_{pdr}, based on the pose of the patient DR from both datasets was used (see Figure 23). Finally, the actual needle tip, P_{ntp}, was defined in the validation dataset, and each error source was calculated as follows:

$$P_{ntp} - R_{pdr}\, P_{plt} = e_{usy} \tag{3}$$

$$R_{pdr}\, P_{plt} - R_{rig}\, P_{plt} = e_{pdr} \tag{4}$$

$$R_{rig}\, P_{plt} - P_{vat} = e_{tde} \tag{5}$$

$$\text{Where, } e_{usy} + e_{pdr} + e_{tde} = P_{ntp} - P_{vat} = e_{ova} \tag{6}$$

The transformation R_{rig} was calculated by registering a vertebra from the planning dataset to its corresponding position in the validation CT dataset. The transformation R_{pdr} was calculated by registering the patient DR from the planning dataset to its corresponding position within the validation CT dataset. The accuracy of the registrations were assessed by generating a surface of each structure (vertebra and patient DR) in both datasets, and by measuring the distance between them. The average and standard deviation distances between the surfaces of all registrations performed were below 0.1 mm for vertebra and patient DR.

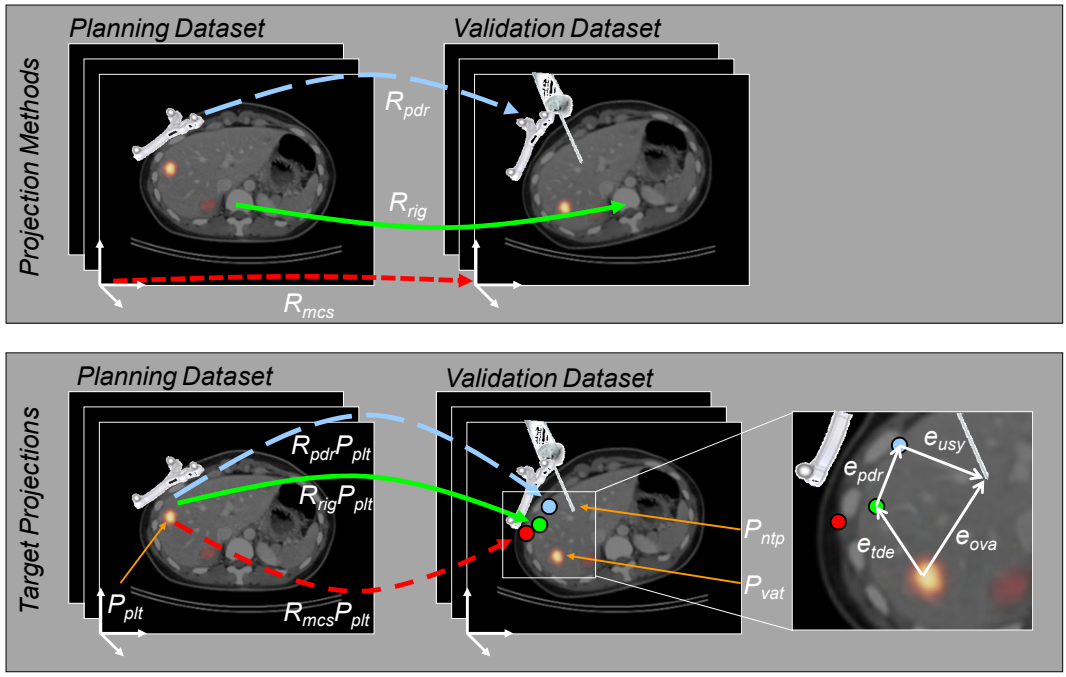

Figure 23: Illustration of the target projection and error components. a) Shows different projection methods: patient DR registration transformation R_{pdr}, rigid structure registration transformation R_{rig}, and machine coordinate system transformation R_{mcs}. b) Shows locations of the target projected with different methods: patient DR registration transformation $R_{pdr}P_{plt}$, rigid structure registration transformation $R_{rig}P_{plt}$, and machine coordinate system transformation $R_{mcs}P_{plt}$. Additionally, the picture on the right illustrates how the different error vectors correlate to each other.

The individual error sources measurement was performed using the planning dataset acquired prior to puncturing and the validation dataset acquired immediately after puncturing. This limited the evaluation to the scenario seen in the validation image, i.e. after releasing the puncturing needle. Therefore, the measured tissue deformation error, e_{tde}, captured only the permanent deformation caused in the tissue around the target, whereas the deformation present throughout the puncture would appear as part of the user-system error. In the same line, the error due to patient DR motion, e_{pdr}, included only the permanent motion of the DR, any movement present throughout the puncture would appear as part of the user-system error. In addition, the user error could not be directly quantified by measuring the distance from the needle tip to the planned target according to the navigation system because for bone punctures the drill and its tip are not navigated. Finally, the *TRE* that represents the discrepancy between the patient-to-image registration could not be isolated based only on the acquired datasets. Consequently, any target error resultant from a miss-registration between the patient and image was also captured as part of the user-system error.

5.1.3 Results

The navigation system based on multimodal images was developed and evaluated with a pilot study using swine cadavers. The navigation platform, which stands beside the PET/CT scanner, did not interfere with the standard image acquisition procedure nor with the normal activity within the biopsy room. The data was successfully transferred from scanner to the navigation platform through the network. The time required to transfer and to load the images into the system was on average 4 min., which is equal to the time required to export the data to a planning station in the standard procedure. The preparation and planning of the intervention could be accomplished beside the patient and with complete separation from the sterile phase. The physician could operate the system without additional help. The actual instrument guidance time during puncture averaged 7.5 min. and 5.5 min. for targets located in bone and soft tissue respectively. The bone punctures showed an increased time due to the drilling part of the procedure. The overall error and the individual error components were also measured for each puncture of the different swine, and are presented below.

The system presented an average overall accuracy of 3.7 ± 1.8 mm, which would be considered sufficient for the PET/CT scenarios. The average overall accuracy achieved for bone and soft tissue procedures were 4.2 ± 2.0 mm and 3.1 ± 1.2 mm respectively. The best result of each puncture type is presented in Figure 24. Table 1 shows the average and standard deviation values of each measured error source. These results show that the system is applicable to both types of punctures, though its performance is better in soft tissue than in bone. The user-system error was the most prominent source for both types of punctures with an average value of 3.9 ± 1.7 mm for bone punctures and an average value of 2.1 ± 0.7 mm for soft tissue. The error due to patient DR motion was more evident in the bone punctures with an average value of 1.2 ± 1.0 mm, whereas the error due to tissue deformation was more evident in the soft tissue punctures with an average value of 1.4 ± 0.9 mm.

Table 1: Average and standard deviation of the error sources presented in millimetres.

	$\|\|e_{ova}\|\|$		$\|\|e_{usy}\|\|$		$\|\|e_{pdr}\|\|$		$\|\|e_{tde}\|\|$	
	AVG	**STD**	**AVG**	**STD**	**AVG**	**STD**	**AVG**	**STD**
S1	3.5	1.4	3.3	1.1	1.3	1.1	0.7	0.5
S2	5.3	2.3	4.8	2.2	1.1	0.7	1.0	0.6
S3	3.1	1.1	2.1	0.8	0.1	0.1	1.5	1.2
S4	3.0	1.4	2.1	0.7	0.4	0.5	1.2	0.7
Bone	4.2	2.0	3.9	1.7	1.2	1.0	0.8	0.6
Soft Tissue	3.1	1.2	2.1	0.7	0.3	0.4	1.4	0.9
All	3.7	1.8	3.1	1.6	0.8	0.9	1.1	0.8

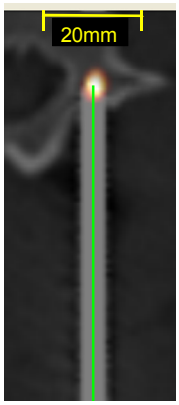

a)

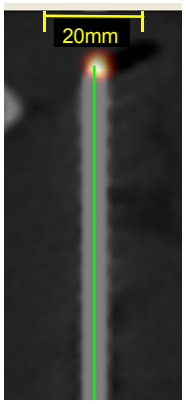

b)

Figure 24: a) Shows the best result for bone punctures, puncture 14 in S1 with a planned trajectory length of 81 mm. b) Shows the best result for soft tissue punctures, puncture 2 in S3 with a planned trajectory length of 98 mm.

To facilitate a better understanding of how each individual error sources contributes to the overall error, the correlation between them and the overall errors are presented graphically in Figure 25, and are discussed below.

Tissue deformation error analyses: The difference in tissue deformation behaviour for both types of punctures is highlighted by Figure 25c and d. The trend line of this error shows a very weak correlation with the overall error for bone punctures, whereas for soft tissue this correlation is prominent. The effect of this error source, $\|e_{tde}\|$, can be well seen in punctures 6 and 7 of S3 that were performed in soft tissue. It indicates an attempt to correct the needle direction when it is closer to the target, which causes tissue deformation and target motion due to the interaction with the needle. The tissue deformation was less evident for bone punctures, as a bone structure was harder to deform or dislocate. Nevertheless, this deformation is also evident in punctures 10 of S1 and 1 of S2, which were performed in flexible bones, rib and the internal part of the tail respectively. Hence, the interaction between needle and bone caused the whole bone to move.

Patient DR error analyses: Although the average error due to patient DR motion, $\|e_{pdr}\|$, is higher for bone punctures, the correlation between this error source and the overall error is not evident for either puncture type (see Figure 25c and d). The trend line of this error shows a very weak correlation between these errors in both cases. Moreover, it shows a scattering of this error around the trend line

of the bone punctures. The punctures in which this error was most evident were 2 and 12 of S1. Further analyses on the CT image datasets showed that the patient DR location (abdomen) of these punctures was not optimal. The formation of gases expanded the abdomen from the time of planning CT acquisition to the time of puncturing (including the validation CT acquisition) which consequently moved the patient DR. This effect together with the longer time needed for puncturing bone, increased the effect of $\|e_{pdr}\|$ in this type of puncture. In addition, the necessary forces applied to the needle while puncturing and drilling in bone were higher, causing consequently, a motion of the surrounding tissue and of the patient DR. Despite not being the most significant error source, care should be taken to avoid the special cases faced here. The error analyses performed for this source indicates that the used patient DR can be effective, if well positioned (e.g. on regions not affected by respiration).

User-system error analyses: The values obtained for $\|e_{usy}\|$ show the ability of the physician to use the system with the provided tracking accuracy. The trend line of this error (see Figure 25c and d) shows a strong correlation with the overall error for both types of punctures. However, bone puncture results present a more evident correlation than soft tissue punctures. Two factors appear to have contributed to this difference: the lack of instrument guidance of the drill and a possible slide of the drill while penetrating the bone surface (as described by the physician during the experiment). The first factor is associated with the method the physician uses to ensure the correct depth of the drill in standard bone interventions. Five millimetres distance holder rings are added to the drill to ensure a maximum depth, and the missing depth (< 5 mm) is measured with bare eyes. The effect of not carefully verifying the drilling depth is highlighted by punctures 2, 3, 5 and 7 in S2. In these cases, the decomposition of $\|e_{usy}\|$ values presented the greatest error component in the drilling direction (see Figure 26 for examples). The second factor is associated with the sharpness of the drill and with the direction of drilling, which is optimal at 90 degrees to the bone surface. The depth of the target inside the bone appeared to have emphasized the sliding of the drill. Small changes in the needle orientation can cause a big deviation for targets placed deep within the bone (see Figure 26c). These problems however, are expected to be reduced by providing the physician with smaller size distance holder rings and sharper drills for penetrating the bone surface. A special case appeared in puncture 4 in S2. The planned trajectory of this trial passed through connective tissue or ligaments (not known by the physician in the swine anatomy) that deviated the needle from the planned trajectory. Even though, the physician tried to correct the needle orientation, this unexpected tissue pushed it out of the planned path. This needle misplacement resulted in the greatest user-system error of our experiments, and demonstrated the importance of good trajectory planning. The soft tissue punctures did not present user errors as high as the bone punctures, nevertheless the results show that there is still room for improvement. One point that remains to be investigated is the learning curve of the physician using the system, which might reduce the user error and consequently the user-system error.

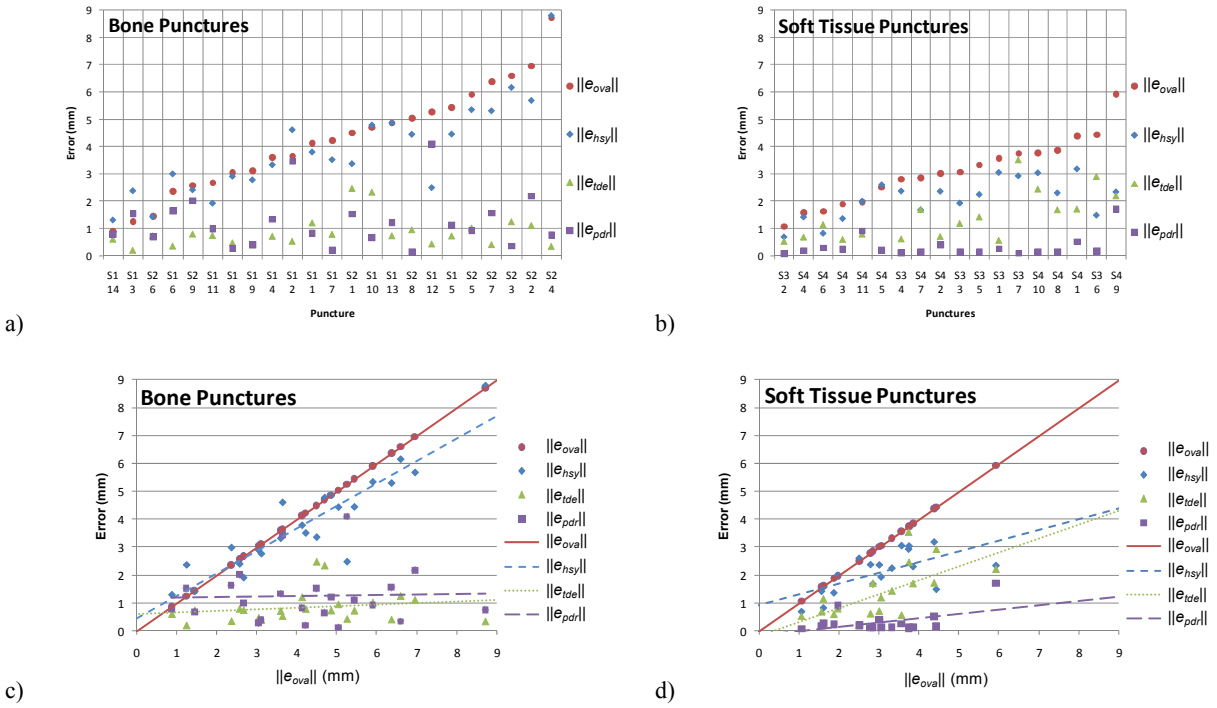

Figure 25: The figures a) and b) show the different error sources per puncture for bone and soft tissue punctures respectively, ordered by the overall error. The figures c) and d) show the correlation between the error sources and the overall error for bone and soft tissue punctures respectively. The lines represent the linear fitting of each error source.

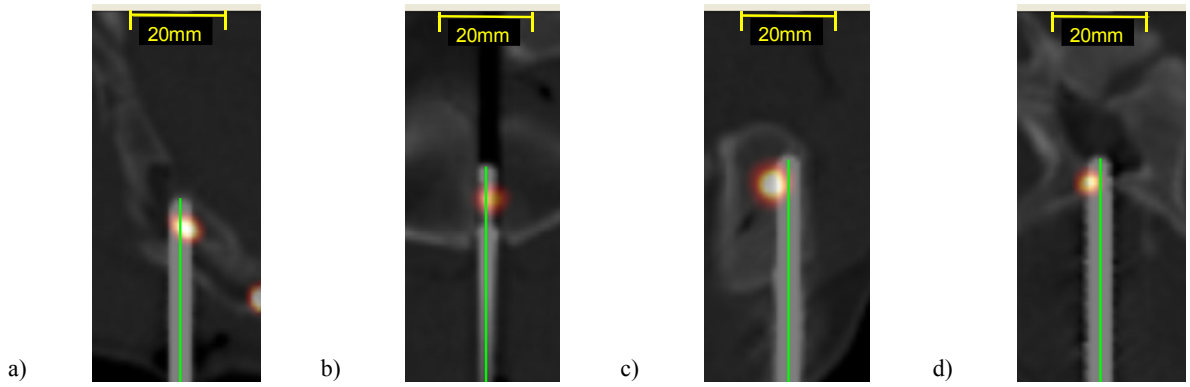

Figure 26: Results of punctures in S2 with high error in the drilling direction. a) Puncture 2. b) Puncture 3. c) Puncture 5. d) Puncture 7.

The mean patient DR centroid to target distance for bone and soft tissue procedures were 137.3 ± 24.0 mm (ranging 90.9 mm to 194.6 mm) and 193.9 ± 47.8 mm (ranging from 107.0 mm to 299.l6 mm) respectively. The mean planned trajectory length for bone and soft tissue were 65.6 ± 17.8 mm (ranging 26.6 mm to 99.1 mm) and 94.0 ± 20.6 mm (ranging from 56.3 mm to 125.2 mm) respectively. The detailed correlation between these distances and each error source is presented graphically in Figure 27, and is discussed below.

Error per patient DR to target distance: The large scattering of the points around the trend line of the overall error and the user-system error of the bone punctures (see Figure 27a) makes it difficult to correlate them with this distance. This indicates that other factors are more influential to these errors than this distance. The error due to patient DR motion though, shows a considerable increase with such distance. For the soft tissue punctures (see Figure 27b), a correlation can be seen for all error sources. The patient DR motion effect as well as the user-system error increase with increased distance. These graphs show the estimated increase of error when the patient DR is placed sub-optimally away from the target. Unexpectedly, the soft tissue deformation showed an increase with this distance

for both type of punctures. Nevertheless, no conclusion regarding this correlation could be made from the performed trials.

Error per trajectory length: The graphs in Figure 27c and d show no clear correlation between the length of the planned trajectory and most of the error sources for both puncture types. However, the user-system error shows a tendency to decrease with increasing target depth. Further data analyses showed that, coincidently during our experiments, targets with short trajectory length were mostly located in flexible bones (e.g. ribs or close to the tail), while targets with long trajectory lengths were mostly located in stable bones (e.g. vertebra or pelvis). The fact that flexible bones are usually located closer to the skin is a possible explanation for the observed decrease in user-system error with increased path length. Any movement of flexible bones while drilling would cause the system to provide inaccurate depth information to the physician, thus increasing the user error during drilling. Moreover, it would not appear as a tissue deformation error because the validation of this study is limited to the image acquisition performed after the puncture and most of the flexible bones can partially recover their initial state after the forces applied for drilling are removed.

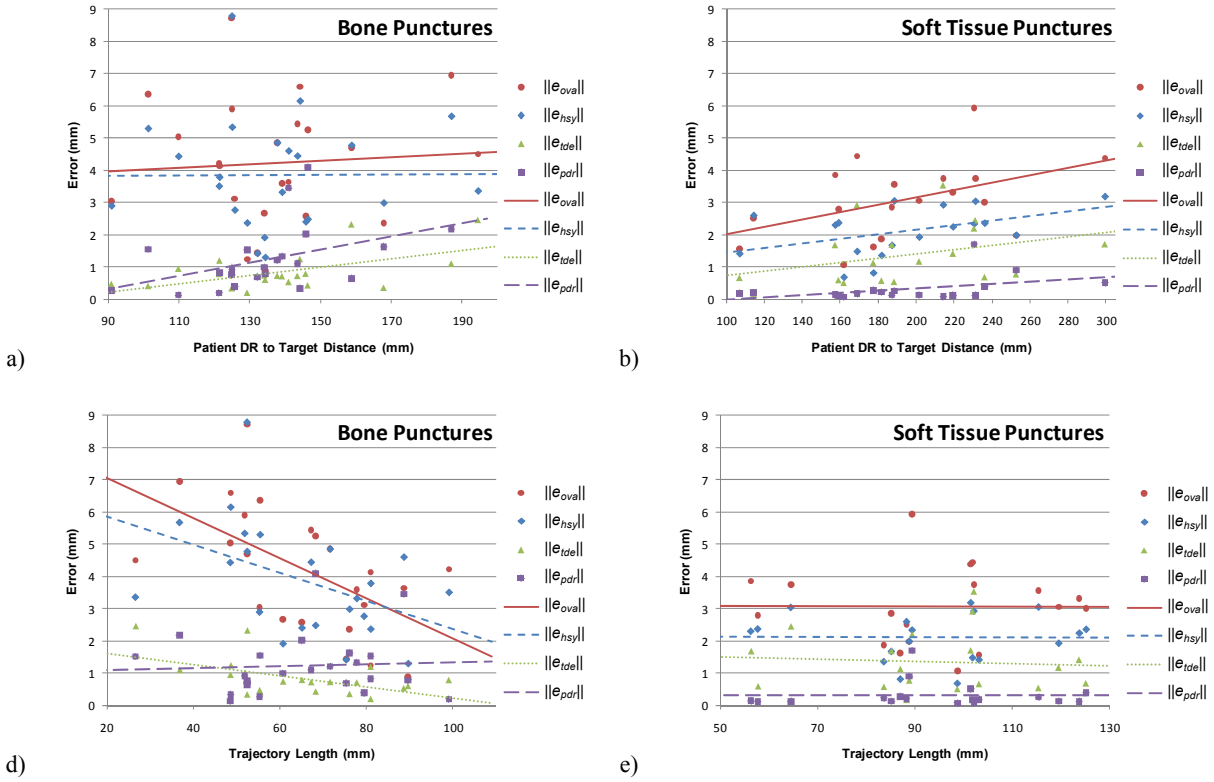

Figure 27: Shows the different error sources per: a) patient DR to target distance for bone punctures, b) patient DR to target distance for soft tissue punctures, c) trajectory length of the bone punctures, d) trajectory length of the soft tissue punctures. The lines represent the linear fitting of each error source.

5.1.4 Discussions and Conclusions

We present an optical navigation system for percutaneous needle interventions based on multimodal images containing separate anatomical and target information such as PET/CT. The proposed system workflow integrating planning, calibration and registration, as well as instrument guidance as part of the intervention were considered effective and proved to reduce the necessary number of CT acquisitions. Within this study, only one image acquisition was required for instrument guidance. During the experiments, the software showed to support the clinically applicable workflow by separating preparation and planning from sterile phases and therefore allowing the system to be managed by a single person. A comfortable arrangement between the system and the physician could be found for most of the punctures. However, to achieve such a configuration, the platform position had to be considered during the planning of the trajectory. The needle guidance was found to be more intuitive when the monitor with the visual information was aligned with the planned trajectory. The image data

could be easily transferred from the scanning station to the navigation system through the network, requiring no additional work compared to the standard procedure. According to the physician, the planning module provided more reliability on the trajectory choice, as well as the possibility of defining paths out of the axial planes, which was not possible with the conventional approach. The structures surrounding the planned trajectory could be identified and considered during the planning process to ensure a safer path definition. The real-time multimodal visualization of the access path along with the region around the needle provided reliable spatial guidance, as well as the recognition of eminent obstacles (e.g. surrounding bones or important anatomical structures). The needle plane viewer was especially important for the bone punctures, helping to guide the drill with the projection of the needle. The automatic needle calibration supported the workflow by removing the need for physical interaction between the physician and the GUI during the sterile phase. Finally, we presented an analyses of the system accuracy based on a pilot study with swine cadavers. The results showed the feasibility of using the navigation system for interventions with targets located in regions not affected by respiration. During the experiments, punctures in soft tissue performed slightly better than those in bone, nevertheless both types presented promising results. The error decomposition provided a better understanding of the source of each error, and helped to identify points for system improvement. It facilitated the comparison between the two puncture types, pointing out the particularities of each of them, as well as supporting the prediction of expected error estimations in different scenarios. We believe that this comparison between needle guidance for targets within these two different types of tissues, provides the research community with crucial considerations for the development of a navigation system for such interventions. Examples of such considerations are: the difficulty of penetrating the bone surface, which increases the final user error and consequently the user-system error; and the significance of the individual error sources for each different puncture type.

Our preliminary results motivated us to further develop the presented system and to commence clinical trials. In addition to improving the points identified in this study, work has been done to modify the rigid patient DR to a set of single markers in order to incorporate deformation detection in to the system.

5.2 Local Bone Registration for PET/CT Target Displacement Correction

The work presented in this section was published in: T. Oliveira-Santos, T. Weitzel, B. Klaeser, T. Krause, L. Nolte, S. Weber, M. Reyes., "Multimodal target correction by local bone registration: A PET/CT evaluation," in Conference Proceedings of Engineering in Medicine and Biology Society (EMBC), 2010 Annual International Conference of the IEEE, Buenos Aires, Argentina, 2010, vol. 1, pp. 5616-5619 . ***Copyright © 2010 IEEE****. The original publication is available at: http://ieeexplore.ieee.org/xpls/abs_all.jsp?arnumber=5626797&tag=1*

Abstract. PET/CT guidance for percutaneous interventions allows biopsy of suspicious metabolically active bone lesions even when no morphological correlation is delineable in the CT images. Clinical use of PET/CT guidance with conventional step-by-step technique is time consuming and complicated especially in cases in which the target lesion is not shown in the CT image. Our recently developed multimodal instrument guidance system (IGS) for PET/CT improved this situation. Nevertheless, bone biopsies even with IGS have a trade-off between precision and intervention duration which is proportional to patient and personnel exposure to radiation. As image acquisition and reconstruction of PET may take up to 10 minutes, preferably only one time consuming combined PET/CT acquisition should be needed during an intervention. In case of required additional control images in order to check for possible patient movements/deformations, or to verify the final needle position in the target, only fast CT acquisitions should be performed. However, for precise instrument guidance accounting for patient movement and/or deformation without having a control PET image, it is essential to be able to transfer the position of the target as identified in the original PET/CT to a changed situation as shown in the control CT. Therefore, we present a pipeline for faster target-position correc-

tion by isolating and registering the bone of interest, as shown in the control CT, with the CT dataset of the original PET/CT acquisition. Challenges such as the masking of the bone of interest and registration robustness in the presence of the needle and its associated metal artefacts are also addressed in this work. Our results confirmed the feasibility of clinically using this technique for target correction on PET/CT bone intervention, and motivated us to incorporate it as part of our IGS for multimodal intervention.

5.2.1 Introduction

Percutaneous image-guided bone needle interventions (i.e. biopsy, wire marking, radio frequency ablation, etc.) are widely used in medicine as a minimally invasive alternative to open surgical interventions. Such procedures are typically performed based on structural volumetric datasets, as for example, computed tomography (CT) and magnetic resonance imaging (MRI). However, medical imaging has changed fundamentally with the introduction of functional modalities such as Single Photon Emission Computer Tomography (SPECT) and Positron Emission Tomography (PET). Using combinations of structural and functional modalities (PET/CT, SPECT/CT), image understanding and diagnosis can be optimized [11, 12]. With these techniques even suspicious lesions without morphological correlation, i.e. not evident in structural datasets, can be identified and verified histologically, following biopsy [14].

In multimodal image interventions, the functional image provides information about the target (e.g. PET and SPECT) while the structural image provides information for instrument guidance (e.g. CT, MRI, etc.). Such procedures are usually performed using a step-by-step technique (similar to CT guided biopsy): Typically, the intervention is planned based on a single-bed co-registered PET/CT acquisition of the patient already positioned for intervention. The needle is then introduced in small steps alternated with repeated control CT acquisitions to ascertain its current position. After the trocar reaches the bone surface, the drilling towards the lesion starts. However, because of the increased time demand for regional PET acquisitions (2-4 min. for image acquisition plus 3-6 min. for image reconstruction), the step-wise control of the needle position is usually not performed as complete PET/CT, but as CT only acquisitions. These CT images may be co-displayed with the first acquired PET image, nevertheless it does not account for possible displacement of the lesion between the first PET/CT acquisition and the control CT scans. These displacements can occur because of patient movement, by the interaction between the needle and the bone when drilling [65], or by an involuntary rearrangement on the scanning table. Independent of their cause, these shifts may produce a significant target displacement in the co-displayed PET and control CT images during the intervention (according to clinical observations often 5-10 mm), potentially leading to an erroneous needle placement. Consequently, the number of necessary punctures and CT image acquisitions increases which causes discomfort and unnecessary radiation exposure to the patient. This misalignment affects not only the standard PET/CT image guided procedure, but also a computer navigated guided intervention, which uses control CT images to update the current navigated scenario. In this type of system, the target position would be wrongly displayed and would therefore lead the physician to puncture in the wrong position. One way of correcting the target position without new PET acquisitions is by registering a control CT with the first acquired CT.

Rigid and non-rigid image registration has been widely used for many years to address problems in the medical field, and has its basic concepts well described in [31]. In the bone PET/CT needle intervention scenario described above, the region of interest (ROI) is compounded of non-rigid and rigid structures (e.g. soft tissue and bones) that move independently to each other. In addition, control CT images contain the puncturing needle and metal artefacts that are not present in the first image and might affect the accuracy of standard registration algorithms, see Figure 31g and Figure 31h.

In order to address these problems and be able to perform a real-time registration during clinical routine, this paper presents a registration pipeline capable of: extracting the bone of interest (BOI) without the needle and therefore turning the registration scenario into a rigid problem; registering a control CT with the first acquired CT; and finally, correcting the target location inside the bone. This paper also validates the method under different conditions (e.g. registration metrics, ROI sizes and initializations) using image data from a navigated PET/CT pilot study with pig cadavers. The imple-

mented pipeline will be incorporated into our PET/CT image based instrument guidance system (IGS) [81] to allow for intra-procedural target position update without the need of a new PET acquisition.

5.2.2 Materials and Methods

In this section, detailed description of the implemented pipeline and the validation experiments are presented.

Implemented Pipeline

The registration pipeline presented here, was implemented with the open source Insight Toolkit (ITK) [82], and is mainly comprised of three parts (Figure 28): reference mask generation, moving mask generation and registration. Its expected inputs are the first acquired CT, i.e. reference image, I_{ref}, a control CT, i.e. moving image, I_{mov}, and the target location in the reference image, P_{tpl}. The main difference between the proposed method and a standard registration (SR) approach is the addition of masks to restrict the registration to the BOI. A detailed description of the registration pipeline components is shown below:

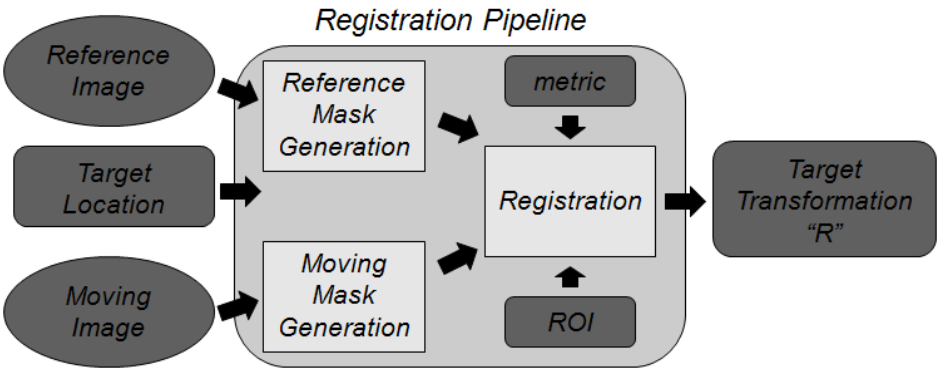

Figure 28: Illustration of the registration pipeline.

Reference mask generation: In the reference image, one might find several structures not rigidly connected to the BOI that might affect the registration. To filter out all of these unwanted objects, a binary mask, I_{rfm}, is generated around the BOI. As a first step, a binary image is created by applying a lower threshold in the reference image to retain only the bone structures, Figure 29b. Care is taken when choosing this value to ensure that different bones generate one binary blob per bone. In this study, an optimal threshold value covering most of the experiments and equal to the bone surface intensity was empirically found. Using P_{tpl} as a seed point, the closest blob of the threshold image is automatically selected as the BOI, Figure 29c. This blob is then dilated (by an empirical radius of 6 mm) to ensure the edges and the inner parts of the bone were included in the mask, Figure 29d.

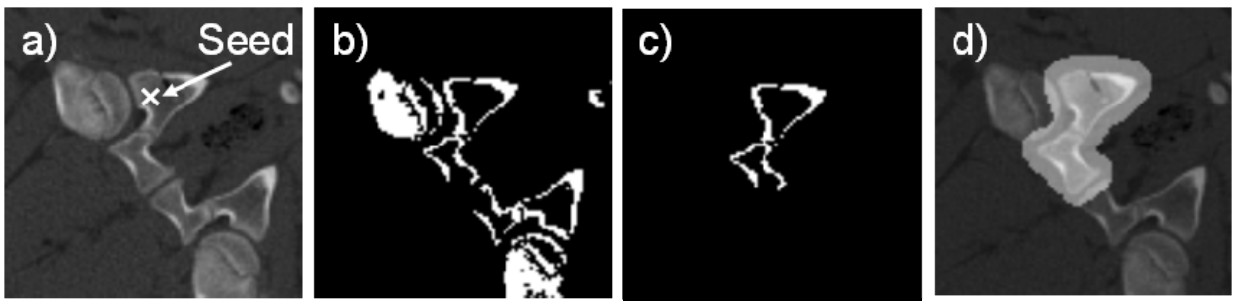

Figure 29: Reference mask generation example. a) Original reference image. b) Binary bone outer surface threshold of image a). c) Seed point (cross) closest blob selected from image b). d) Resulting reference mask overlaid with image a).

Moving mask generation: The presence of the puncturing needle and its associated metal artefacts make the moving image different from the reference image. To reduce this difference, these objects

are filtered out through the application of a binary mask, I_{mvm}. As a first step, a binary image is generated with an upper and a lower threshold. Whereas the upper threshold is used to filter out needle and artefacts with high intensity values, the lower threshold is used to filter out shadow artefacts with low intensity values. In this study, the definition of these thresholds was performed assuming that the needle and its more prominent metal artefacts have intensity values higher than the bone values and lower than the soft tissue values, respectively. Therefore, the highest bone intensity value of a calibrated scanner was set as the upper threshold and the lowest soft tissue value was set as the lower threshold. To ensure the needle is completely masked out, an erosion filter with the empirical radius of 2 mm (based on the needle thickness) is then applied to the mask.

Registration: The registration is the core part of the pipeline and utilizes the generated masks to constrain the registration metric to the BOI of the input images. Furthermore, it uses a regular step gradient descendent optimizer to calculate a 3D rigid transformation, R, that maps the reference image ROI (centred in the target location) to the moving image. Linear interpolation is used for re-sampling during registration.

Input Data Generation

The data from a navigated PET/CT biopsy pilot study using pig cadavers prepared with radioactive spots (lesions simulated by 1 mm diameter cotton wool balls with ca. 0.5 MBq 18F solution placed inside bone) was used as input for the registration experiments. The image data was acquired with the animal cadaver lying down on the scanner table and in alternation with biopsy punctures. Two datasets (each containing co-registered PET/CT) were obtained per puncture: a planning dataset and a validation dataset. The planning dataset was acquired prior to each puncture. Its PET image was used here to define P_{tpl}, and its CT image was used as the reference image for the registration pipeline. The validation dataset was acquired right after each puncture with the needle in place. Its PET image was used to define the validation target location, P_{tva}, and its CT image was used as the moving image for the registration pipeline. The target positions were manually defined in every puncture using standard axial, sagittal, coronal viewers fusing PET and CT images.

Image acquisition was accomplished with a Siemens Biograph 16 Hi-Rez with voxel size set to 1.37 × 1.37 × 1 mm and 2.67 × 2.67 × 2 mm, for CT and PET (intrinsic spatial resolution of 5 mm) respectively. Both image modalities share the same coordinate system. A bone biopsy set with a coaxial needle of 3.4 mm outer diameter (10 G) and 130 mm length was used.

Experiment Description

To validate the different components of the implemented pipeline, three experiments were performed: the *reference mask generation test* to assess the correctness of the BOI selection; the *pipeline parameters test* with the purpose of measuring the robustness against the metal artefacts not fully removed by masking, quantifying an optimal ROI size (feasible computational time with minimal information loss), and accessing the masking effect in the registration result; and finally, the *repeatability test* to measure the registration robustness against the initial deformation.

Reference mask generation Test: Besides the automatic masks (seed in P_{tpl}) generated while testing the registration pipeline, 40 additional masks were created with seed points manually selected in random locations of the BOI. Each additional mask was pixel-wise compared with its respective automatic mask to ensure the repeatability of the mask generation. A visual inspection, Figure 29d, was also performed to verify the BOI selection.

Pipeline parameter test: The registration pipeline was compared to the standard registration using four bone lesion datasets and different parameters, such as different ROI sizes (starting from 40 × 40 × 40 mm and increasing 10 mm in each axis up to 110 × 110 × 110 mm) and different metrics (Mattes mutual information (MI) [83, 84] and normalized correlation (NC)). The experiment was performed as follow.

- For each puncture dataset, the I_{rfm} and I_{mvm} masks were generated for I_{ref}, and I_{mov} respectively.

- A set of registration transformations, R, were estimated with the registration pipeline (with I_{rfm} and I_{mvm} masks) and with the standard registration (without masks), using all different parameter combinations (ROI sizes and metrics).
- The accuracy evaluation was performed using the voxel-wise sum of absolute differences (SAD). However, in order to restrict the evaluation to the BOI and to generate a normalized value, only voxels inside the masks were considered in the sum. The SAD calculation was restricted by the masks even for the standard registration transformation that was estimated without masks. See the SAD formulation below:

$$I_{ad} = abs\left(I_{ref} - R \circ I_{mov}\right), \quad I_{cbm} = I_{rfm} - R \circ I_{mvm} \tag{7}$$

$$SAD = \left(\sum \left(I_{ad} \cap I_{cbm}\right)\right) / fnum\left(I_{cbm}\right) \tag{8}$$

Where, *abs* is the voxel-wise absolute value, ○ applies a transformation to an image, ∩ is the voxel-wise multiplication, *fnum* is the number of foreground voxels in the mask, and the mask images have background value 0 and foreground value 1.

Repeatability test: To simulate distinct target movements, a total of 31 different initial transformations, T_{ini}, with translations of up to 11 millimetres and rotation of up to 11 degrees in each axis were applied to the moving image and to the P_{tva} of each puncture. The initial target distance, D_{ini}, was calculated ($|P_{tpl} - T_{ini}P_{tva}|$) for each different initial transformation. The registration R was then estimated for each $T_{ini} \circ I_{mov}$ using the parameters configuration (ROI size and metric) with a good trade-off between computational time and registration accuracy (from the *pipeline parameter test*). Finally, the final target distance was calculated ($|P_{tpl} - RT_{ini}P_{tva}|$) per registration in order to assess the robustness against different target movements. Convergence was assumed for final target distance smaller than 1 mm. The tests ran on a PC, Intel Core 2, 2.16 GHz, 2 G RAM.

5.2.3 Results

The reference mask of each puncture was repeatedly generated with the correctly BOI selection for most of the tested seeds, Figure 29 illustrates one case. However, some seeds placed on rib parts bordering the spine wrongly selected a small portion of the rib which was not sufficient for registration.

The results of the *pipeline parameters test* are presented in Figure 30 and one example is illustrated in Figure 31. The MI standard registration curve when compared to the MI and NC registration pipeline curves show the importance of the masks for cases like Puncture 1 and Puncture 3. One can see the standard registration accuracy decreasing with the increasing of the ROI size contrary to the registration pipeline curves. In these cases, bigger ROI sizes increased the presence of deformed regions in the registration. The standard registration NC peak in puncture 1 also shows the instability of the registration without mask when the ROI includes part of deformed regions. The effect of the needle and its metal artefacts can be verified through the NC standard registration curve in which the accuracy was affected for all four cases. The increase of the ROI size behaviour is well illustrated by the registration pipeline curves in which an increase of accuracy is seen before reaching a more stable value. The registration pipeline with MI and NC did not show significant accuracy differences for the studied cases. However, the computation time of the used MI metric was more efficient than the NC, and therefore was chosen for further tests.

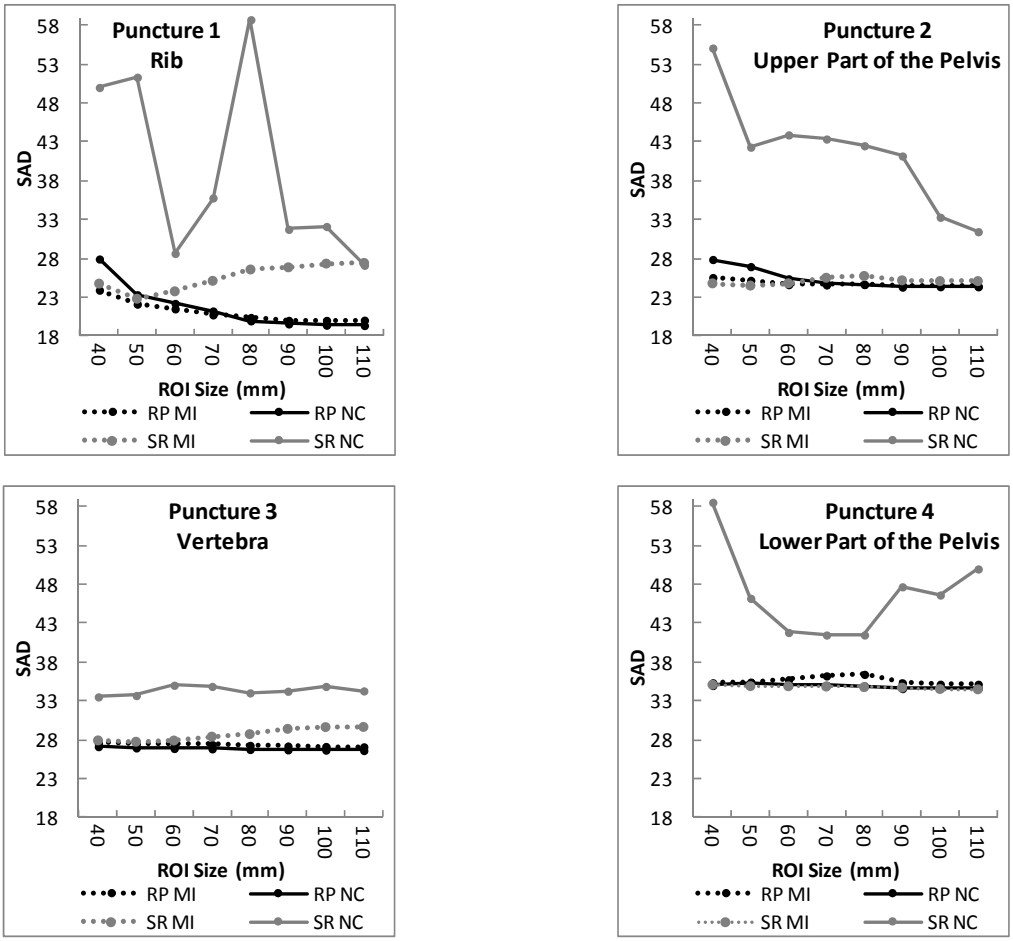

Figure 30: Puncture graphs comparing the SAD behaviour of the registration pipeline (RP) against standard registration (SR) using ROI sizes using MI and NC metrics.

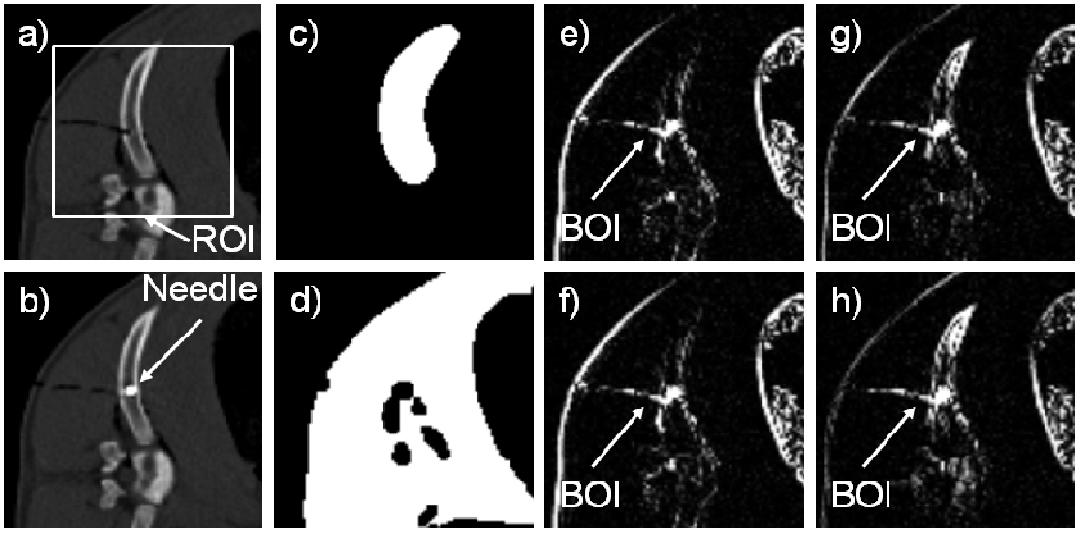

Figure 31: Registration example for ROI size 90 mm. a) Reference image. b) Moving image. c) Reference mask. d) Moving mask. e) Subtracted registration pipeline MI results. f) Subtracted registration pipeline NC results. g) Subtracted standard registration MI results. h) Subtracted standard registration NC results. Subtracted images are the absolute difference between reference and transformed moving image displayed with window/level equal to 200/100.

The *repeatability test* results for MI metric and ROI size 90 mm are presented in Table 2. It shows the convergence percentage (CP) and registration time per D_{ini} range.

Table 2: Convergence Percentage per Initial Distance. Average time is given in seconds.

Puncture	1		2		3		4	
D_{ini} up to:	CP	Time	CP	Time	CP	Time	CP	Time
10 mm	71	210 ± 62	100	170 ± 57	100	232 ± 73	100	79 ± 45
20 mm	5	248	88	144 ± 47	87	196 ± 41	35	155 ± 156

5.2.4 Discussions and Conclusions

The reference mask correctly dissociated the surrounding structures of the BOI for most of the tested cases. However, a better segmentation would be desirable to cover all cases.

The *pipeline parameters test* demonstrated the importance of having a mask around the BOI even with the limited pig cadavers' deformation. The masking effect is expected to be even more evident with the greater deformation of real patients. The results also show that a small ROI size with the MI standard registration is enough for cases in which the ROI contains a BOI portion with enough information for registration and no deformed structures. The masking of the needle and its associated metal artefacts played an important role on NC metric and indicate a possible benefit for other linear metrics (e.g. sum of absolute differences). As the computational performance is an important factor, investigation with faster linear metrics should be performed.

The *repeatability tests* showed the robustness against the initialization for most of the cases in the range up to 10 mm which is sufficient for clinical routine. However, each bone presented a different D_{ini} range limit and would require a more detailed investigation for precise identification of each limit. Based on the tried transformations, puncture 1 (rib) could not stand big perpendicular shifts (8 mm) or big angle deformations (11º), as it is a fine bone and its overlapped portion was compromised. More freedom was shown for punctures 2 and 3 that coped with D_{ini} of up to 19 mm with only a couple of non converged cases. Puncture 4 converged stably for D_{ini} of up to 12 mm. Computational time is still not ideal, however applicable to the studied scenario and open for optimizations not considered in this study.

The results obtained were encouraging and demonstrated the feasibility of the presented registration pipeline for correcting target positions during bone needle interventions based on multimodal images (e.g. PET/CT). This technique, allows for a more precise visualization of targets in a control CT image without having to acquire a new PET image which would also benefit IGS relying on such datasets.

5.3 Percutaneous Nephrolithotomy Requirements and Workflow

The work presented in this section was published in: T. Oliveira-Santos, M. Peterhans, B. Roth, M. Reyes, L. Nolte, G. Thalmann, S. Weber, "Computer aided surgery for percutaneous nephrolithotomy: Clinical requirement analysis and system design," in Conference Proceedings of Engineering in Medicine and Biology Society (EMBC), 2010 Annual International Conference of the IEEE, Buenos Aires, Argentina, 2010, vol. 1, pp. 442-445. ***Copyright © 2010 IEEE****. The original publication is available at: http://ieeexplore.ieee.org/xpls/abs_all.jsp?arnumber=5627387*

Abstract. Percutaneous nephrolithotomy (PCNL) for the treatment of renal stones and other related renal diseases has proved its efficacy and has stood the test of time compared with open surgical methods and extracorporeal shock wave lithotripsy. However, access to the collecting system of the kidney is not easy because the available intra-operative image modalities only provide a two dimensional view of the surgical scenario. With this lack of visual information, several punctures are often necessary increasing the risk of renal bleeding, splanchnic, vascular or pulmonary injury, or damage to the collecting system, which sometimes makes the continuation of the procedure impossible. In order

to address this problem, this paper proposes a workflow for introduction of a stereotactic needle guidance system for PCNL procedures. An analysis of the imposed clinical requirements, and a instrument guidance approach to provide the physician with a more intuitive planning and visual guidance to access the collecting system of the kidney are presented.

5.3.1 Introduction

Percutaneous nephrolithotomy (PCNL) is a surgical procedure to remove stones from the kidney through a small puncture wound through the skin after intra-corporeal lithotripsy. PCNL has proved its efficacy and has stood the test of time compared with open surgical methods [85] and extracorporeal shock wave lithotripsy [86]. Developments in instrumentation, radiological imaging, and urologist skills have helped this type of surgery to achieve new frontiers in terms of safety and efficacy. This method has acquired a reputation of a low failure rate and has been a superior alternative to shock wave lithotripsy.

PCNL is typically performed with the patient in the standard prone position allowing a large surface area for the puncture site, less tissue along the way to the kidney, and a wide space for instrument manipulation. It has been presumed that a posterior puncture possibly minimizes the risk of splanchnic, vascular injury, haemorrhage (with a rate of 3 % to 12 %) and bowel injury (with a rate of 0.2 % to 0.5 %) [87]. For these procedures, the initial planning is based on a pre-operative Computer Tomography (CT) scan acquired prior to the intervention. After planning the access points to the collecting system of the kidney, the actual puncture is performed. Thereafter, a guide wire is placed through the needle and the puncture channel is dilated to place a 30 French dilatators sheath (Amplatz), so that the stone can be fragmentized and removed in pieces by minimally invasive instruments.

The most difficult point of the procedure is the access to the collecting system of the kidney. Ultrasound (US) guided puncture provides only a two dimensional view of the surgical scene and the exact site of the puncture is sometimes very difficult to reach. Consequently, several punctures are often necessary increasing the risk of renal bleeding, injury or damage to the collecting system with subsequent perforation and inability of continuing the procedure. Moreover, the prone position also has inherent drawbacks, for example, it is risky for patients with cardiopulmonary ailments and markedly obese patients due to compression of the vena cava with concurrent reduced back flow. These problems in addition to the time spent/risk taken to turn the patient to prone position shows the benefits of puncturing sometimes in supine position. However, this requires a precise way of avoiding anatomical obstacles and a better visualization of the final aim. One way of addressing these problems is by means of stereotactic instrument guidance.

The general principles of computer navigation were described in [27] and [28], and have been applied to many different clinical areas. Among others, needle guidance applications are highlighted, in which systems have been developed to address liver puncture [36], vertebroplasty [33, 39], and general biopsy procedures [39]. All these systems are able to navigate needles; however, none of them studied the feasibility of navigation applied to renal calculi. In this field, Mozer *et al.* [59] present a system that relies on the registration of CT and US to provide the physician with precise needle guidance. Nevertheless, the use of US images is not always possible, e.g. obese patients, or patients in supine position with a long distance to the target.

Hence, this paper describes a workflow for introduction of a stereotactic needle guidance system for PCNL interventions which conforms to clinical requirements. Based on this analysis, an instrument guidance system using a standard fiducial based registration method [80] is presented. This solution aims to provide better procedure planning and more intuitive visual guidance during the access to the collecting system of the kidney.

5.3.2 Materials and Methods

This section describes the technical and clinical requirements for a PCNL navigation system and the necessary workflow for incorporating computer navigation in this type of procedure.

Technical Requirement analysis

PCNL is performed in a sterile OR environment with fluoroscopy and ultrasound imaging support. The high technical complexity and the usage of different imaging devices require a navigation setup which is flexible to use and can be integrated in the existing OR environment. The work space for instrument tracking is limited to the area of surgical actions where the positions of needles and the patient need to be measured. Interaction with the navigation system and efforts for patient tracking are to be reduced to a minimum in order to avoid additional complexity in the surgical workflow.

Workflow Description

In order to introduce navigation in the PCNL workflow, some additional steps are necessary. For example, skin markers must be applied to the patient before the pre-operative CT scan. A detailed description of the procedural workflow is presented below:

1) **Imaging Patient Preparation.** Radio-opaque fiducial markers (Beekley PinPoint#128, Figure 32) are placed on patient skin surrounding the approximated puncture area.
2) **Pre-operative Imaging.** A pre-operative CT image including the fiducial markers and the kidney is acquired with patient lying in the intended surgical position. After imaging, the precise location of the markers are drawn onto the skin with a surgical marking pen and the radio-opaque markers are removed from the patient.
3) **Surgical Planning.** The planning procedure is accomplished offline prior to the intervention. The kidney and surrounding critical structures are segmented from the CT data and the access path is defined using the volumetric CT data and segmented 3D representations thereof. Paths composed of a point-pair defining the target location and the needle entry point are chosen, such that critical anatomical structures are avoided. The planned data is then saved for later use during the intervention.
4) **Patient Preparation.** Anaesthesia and retrograde, transurethral insertion of a urethral catheter for filling of the collecting system in the kidney is administered with the patient in the supine position. The patient is then placed in the final surgical position, and an optical reference is attached on his skin - near the marks drawn after pre-operative imaging.
5) **Needle Calibration.** The needle optical reference is attached and its tip position and axis orientation are calibrated relative to the needle tracker coordinate system.
6) **Patient-to-Image Registration.** The patient is registered to the pre-operative image data using the fiducials in order to establish the correspondence between the surgical scenario and the planning data.
7) **Needle Guidance.** During the actual needle insertion, the physician steers the needle to the kidney using the visual feedback provided by the navigation systems graphical user interface. The needle insertion is visualized in the segmented 3D data and reformatted CT slides showing the needle insertion plane are calculated in real-time.
8) **Position Validation.** During the needle insertion process, fluoroscopic images are acquired in order to validate the correctness of the needle insertion path (2D validation). The target is considered reached when the standard fluoroscopy images together with contrast agent injection ensure that the needle is inside the kidney collecting system.
9) **Stone Removal.** The inserted needle is used to prepare the path for the nephroscope. Kidney stones are broken in small pieces and removed by special graspers.

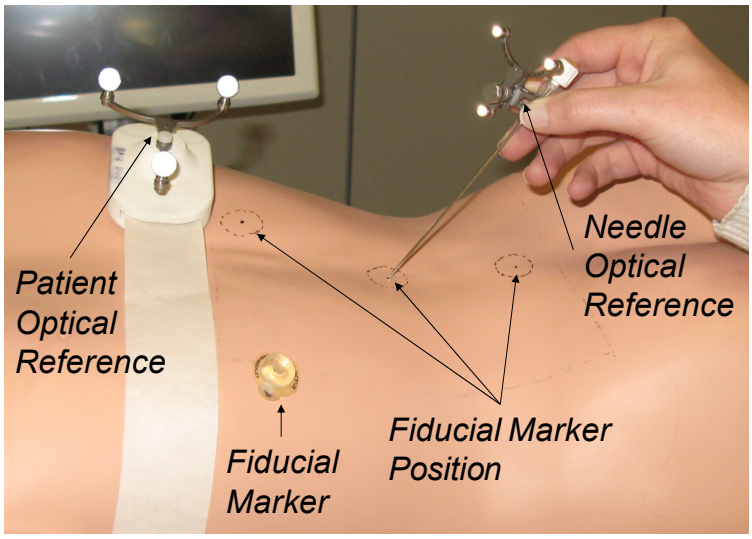

Figure 32: Patient optical reference setup with the fiducial marker used for imaging and their respective positions marked with a surgical pen.

Navigation System

The instrument guidance system (Figure 33) consists of an optical tracking camera (NDI Vicra camera, Northern Digital Inc., Waterloo, Canada), two touch screens and a computer which are fixed onto a transportable support. The tracking camera provides a working volume of around 0.125m^3 which is sufficient to cover the entire working space. The use of passive optical tracking technology allows for high flexibility in the choice of the needles and avoids additional complexity introduced by wired connections to the navigated instruments. The touch screens are packed into sterile covers and facilitate easy user interaction. The navigated instrumentation set (Figure 32) consists of an optical needle reference, a calibration device, and an optical patient reference to be attached to the patient by means of a belt or through sterile tape.

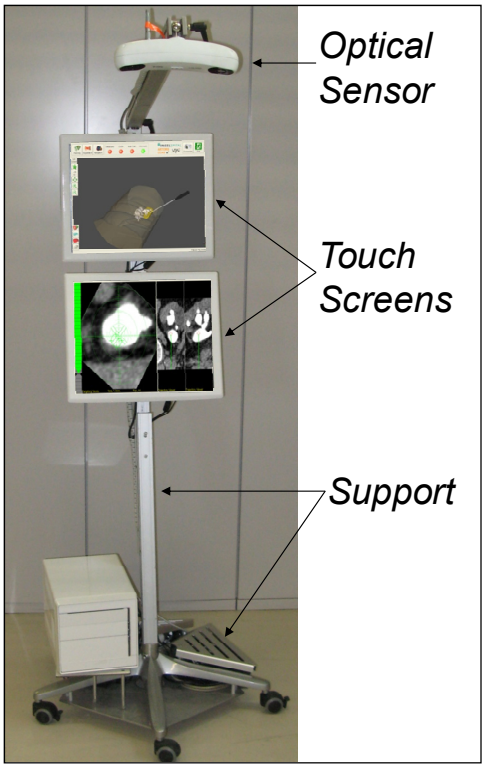

Figure 33: Instrument guidance system.

Software design and interaction concept

The system provides the following functionalities: 1) intervention planning, 2) instrument calibration, 3) registration, and 4) instrument guidance.

The planning of the procedure is based on the CT datasets and can be performed prior to the surgery. This enables the use of interaction devices such as mouse and keyboard for precise localization of different insertion paths. The planned procedure can be saved, and quickly loaded to the system during the intervention.

Calibration, registration and guidance are performed intra-operatively. Therefore, within this phase, sterile components are required, and system interaction is kept minimal in order to avoid disturbing the usual surgical workflow. For this purpose, automatic detection of surgical actions is integrated into the system and allows for touch-free instrument calibration and patient registration. Once registration is confirmed, the needle guidance application is started.

Experiments

In order to get the physicians feedback about the developed system, an experiment with a rapid prototyped (Figure 34) phantom was setup. Physicians were asked to interact with the system and to give their opinion about the functionalities provided. The steps required for incorporation of computer navigation in PCNL interventions were explained to them and the proposed workflow was validated to look for points incompatible with clinical routine. Moreover, to quantify the accuracy of the proposed system, a set of punctures were performed using the phantom presented in Figure 34. Four targets were defined on the surface of the kidney stones and a set of 6 trials (with two different needle entry points) were realized per target. The soft tissue was simulated with a thick layer (approximately 10 cm) of wax in gel placed over the phantom. The final needle tip to target distance was measured with ruler using the mark produced by the needle tip on the phantom surface. The time required for navigation was also recorded.

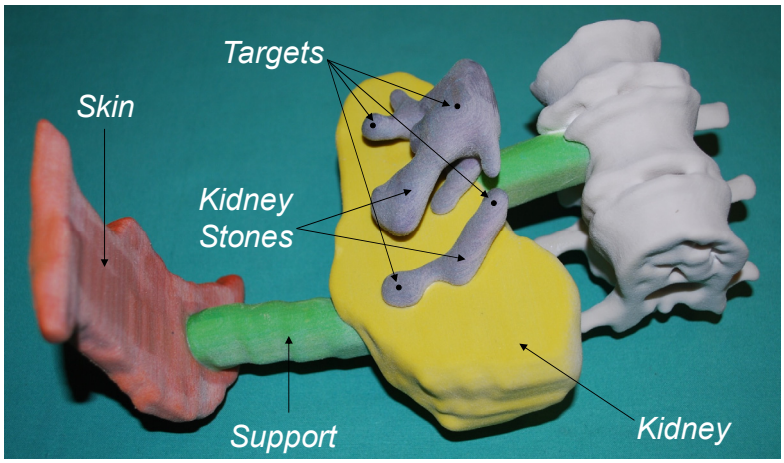

Figure 34: Rapid prototype model used to demonstrate the system to the physicians.

5.3.3 Results

Surgical Planning

In the planning module (Figure 35), three standard planar views (Coronal, Sagittal, and Axial) provide the same functionality as used in clinical routine, and one 3D viewer provides an overview of the planned situation. Using the planar viewers the user can precisely set the target location, and through the 3D viewer a needle entry point can be quickly chosen by selecting a position on the patient skin. These two locations define the planned trajectory that can be verified on the trajectory viewer. This viewer can be rotated around the planed path to help find possible anatomical obstacles. Additionally, the fiducial markers are defined in the CT for later registration.

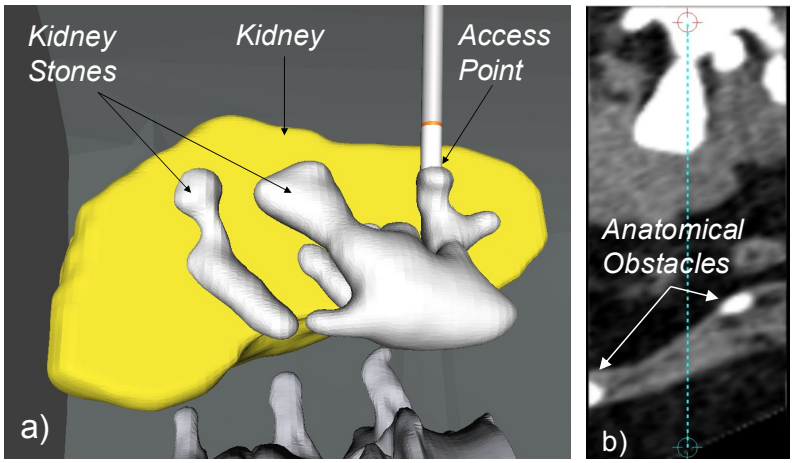

Figure 35: a) 3D viewer showing the planned access point. b) Trajectory viewer showing the planned trajectory with possible anatomical obstacles.

Calibration and Registration

For calibrating the needle tip and its axis orientation, the needle is simply placed in the calibration device and displayed to the optical tracking system. The calibration process triggers automatically, as soon as the needle and the calibration unit are in their ultimate calibration configuration. To register the patient anatomy with the available imagery, the surgeon digitizes the fiducial markers using the navigated needle. A conventional pair-point matching algorithm is then applied to calculate the patient-to-image registration transformation. The complete process takes between 20 and 30 seconds.

Needle Guidance

The navigation functionality (Figure 36) provides visual information to guide the needle to the target according to the planned trajectory. It consists of three main viewers: the 3D viewer offering an overview of the intervention scenario for needle entry point localization; the targeting viewer offering a view along the planned trajectory and looking towards the planned target, together with distance information; and, the needle plane viewer displaying a plane aligned vertically with the needle axis that is useful for obstacles detection.

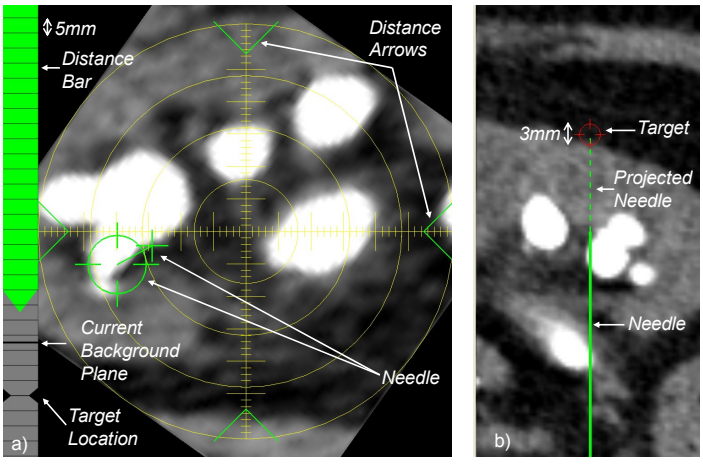

Figure 36: a) Target viewer. b) Needle plane viewer.

Accuracy Experiment

An average distance of 1.63 mm and an average navigation time of 01:09 minutes were achieved for the 24 trials. A detailed result description is presented in the Table 3.

Table 3: Average distance and time per target.

Target	1	2	3	4
Distance (mm)	1.33 ± 0.85	1.67 ± 0.52	2.17 ± 1.47	1.33 ± 0.52
Time (min.)	1:02 ± 0:15	1:06 ± 0:10	1:27 ± 0:23	1:03 ± 0:15

5.3.4 Discussions and Conclusions

This paper presented an instrument guidance system aimed at high precision percutaneous nephrolithotomy, and a dedicated workflow for instrument guidance in PCNL interventions conforming to specific clinical requirements. An instrument guidance system was developed to guide urologists in accessing the collecting system of the kidney. This system was then validated by clinical experts in a laboratory setup using an anatomical phantom. The complete workflow was reviewed with physicians to identify conflicts with the OR requirements and workflow specifications. The experts' feedback was positive regarding the guidance visibility and planning capability introduced by the system. Accordingly, the guidance solution not only provided spatial orientation inside the body, but also the opportunity to visualize upcoming obstacles. Moreover, the accuracy achieved with the phantom experiment was considered enough for the PCNL scenario. The proposed solution did not interfere with the current adopted clinical workflow, as the stereotactic needle guidance system was considered to be an additional tool. The only steps not actually present in the standard procedure workflow (i.e. needle calibration and patient-to-image registration) were not considered disturbing, as they are fast and require minimum interaction.

Although stereotactic guidance introduces a better sense of orientation when steering the needle to the target, it is known that different effects will contribute to spatial errors in the instrument guidance phase. The main sources of such error are deformations caused by needle-tissue interaction, as summarized by Abolhassani *et al.* in [65], and organ deformations caused by breathing, as showed in [88]. However, during the PCNL procedure the patient is intubated and consequently the respiratory cycle is well controlled allowing a gating at the same respiratory position while puncturing. The needle-tissue interaction can be controlled by teaching the physician to not correct the needle direction by bending it while inside the body. In any case, these deformations can be followed up by the intra-operative image modalities mentioned above.

The positive output of this work allowed and motivated further evaluation of the system under clinical conditions and therefore an experiment with real patient is being planned in the near future. The possibility of incorporating the intra-operative image modalities used in the standard PCNL procedure as an update of the current scenario for the navigation system is also being investigated.

5.4 Clinical Experiment: PET/CT Guided ENT Biopsy Intervention

In this section, a clinical case of biopsy addressed with the developed system is presented. This experiment intended to evaluate the performance and interaction of the system within a clinical environment.

5.4.1 Introduction

A patient with an undifferentiated Carcinoma in the nasal cavity with arrosion of the skull base and meninges was previously treated with radical radiotherapy. After completion of the treatment and clinical full remission of the large tumour, the diagnose was performed based on PET/CT images. The activity showed in the PET (see Figure 37) suggested that traces of the tumour were still present. Therefore, a biopsy was necessary to confirm the diagnose.

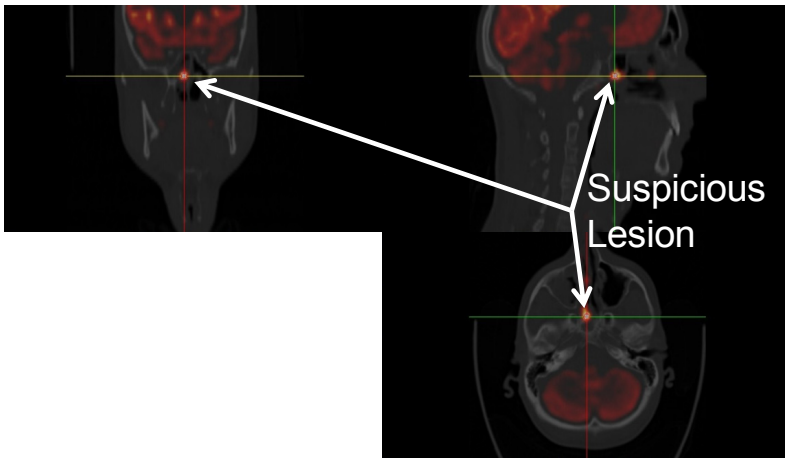

Figure 37: Suspicious lesion location displayed in the axial (lower right), sagittal (upper right), and coronal (upper left) slices with fused PET and CT of the patient's head.

5.4.2 Materials and Methods

The system presented in the previous sections have been slightly adapted to support the mentioned intervention. The clamps and dynamic references developed to track needles were used to enable tracking of a needle like instrument (see Figure 38a). A calibration unit was used to determine the tip location and axis orientation of the tracked instrument. The patient was tracked by means of a rigid dynamic reference attached to his head via a band (see Figure 38b). The dynamic references, clamps and calibration unit were sent along with the standard instruments to sterilization. The image guided biopsy was performed in the following order.

Pre-Intervention phase:

- **Image Transfer.** The PET/CT datasets used for diagnose were loaded into the navigation system prior to the intervention.
- **Planning**. A trajectory comprising a target and a needle entry point was planned (see Figure 39a). The trajectory viewer showed in Figure 39b was used to ensure there was no obstacles along the planned trajectory. In addition, five anatomical landmarks including two points in between the teeth and three close to the eyebrow region (see Figure 40) were defined.

Intra-Intervention Phase:

- **Patient Preparation**. The patient was positioned for surgery and prepared with general anaesthesia. The patient tracker was attached to the patient forehead via a band. The system was placed beside the patient as showing in Figure 41a.
- **Instrument Calibration.** The instrument dynamic reference was clamped to the instrument shaft, and the instrument tip position and axis of orientation were determined using the calibration unit. The calibration is automatically performed by showing the instrument dynamic reference and the calibration unit to the tracking camera for a few seconds.
- **Patient-to-Image Registration.** Subsequently, the patient was registered to the image datasets by putting the tip of the instrument on the correspond landmark location on the patient. Each point is automatically acquired after maintaining the tip of the instrument at the same location for a few seconds.
- **Instrument Guidance**. The surgeon used the visual feedback provided by the navigation system to steer the instrument tip to the target according to the planned trajectory.
- **Target Reached.** The correct location of the instrument tip was confirmed with endoscopic images. Finally, a sample of the tumour region was taken and sent to biopsy.

a) 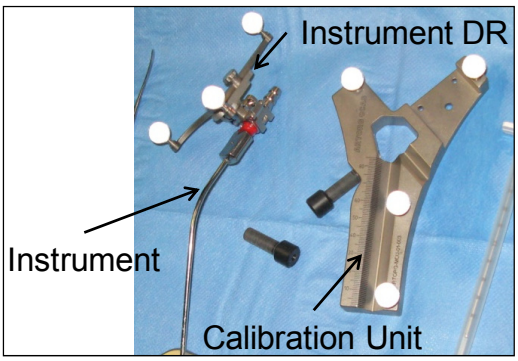

b) 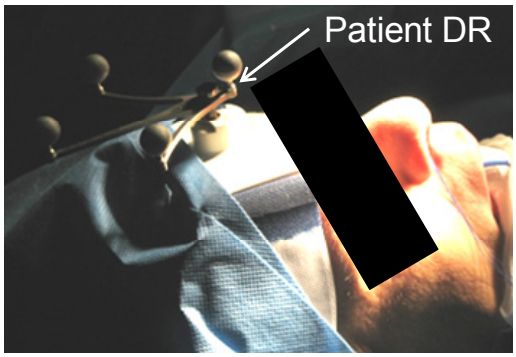

Figure 38: Instruments and patient preparation. a) Shows the instrument to be tracked with the respective dynamic reference (DR) attached to the instrument shaft via a clamp, and the calibration unit used to calibrate the instrument intra-operatively. b) Shows the patient dynamic reference attached to the patient forehead via a band in order to provide referencing to the patient.

a)

b) 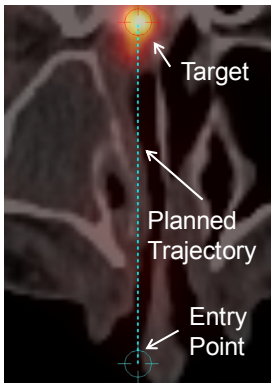

Figure 39: Overview of the planned scenario. a) Volume rendering of the patient's head with the planned trajectory. b) Trajectory plane (located at position showed in a)) showing the planned trajectory comprising a target and an entry point.

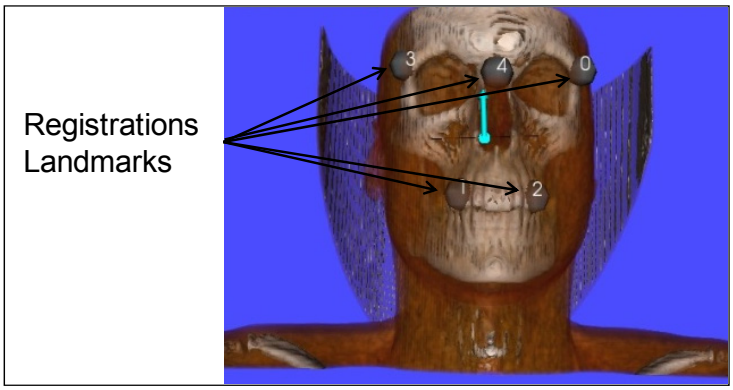

Figure 40: Overview of the five landmarks used during the intervention in order to register the patient to the image.

5.4.3 Results

The endoscopic image showed that the system correctly guided the tip of the instrument to the target. Figure 41a shows an example of the setup during the instrument guidance. Figure 41b shows a close-up to the tracked instrument and patient. Figure 41c and d show the overview of the intervention scenario and the targeting viewer displayed by the navigation system.

a)

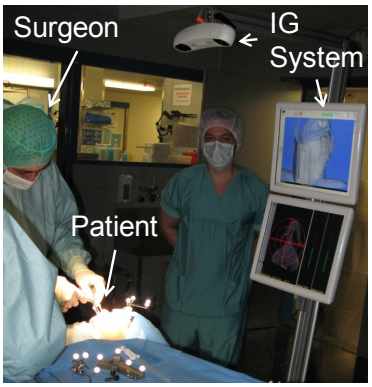

b)

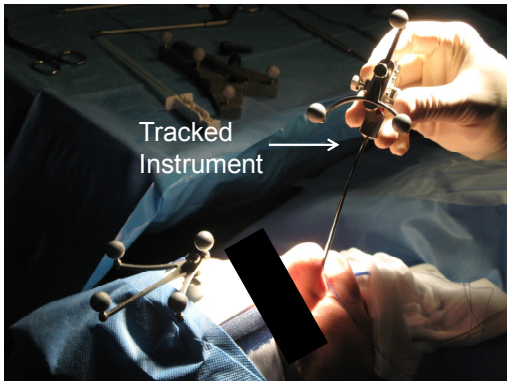

c)

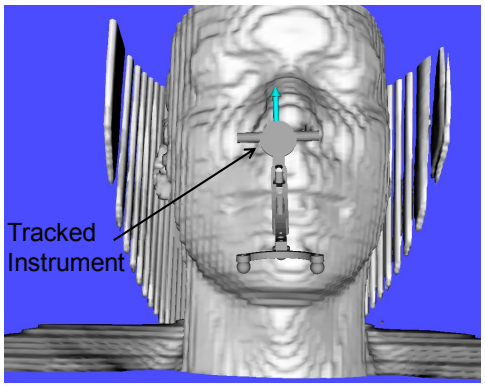

d)

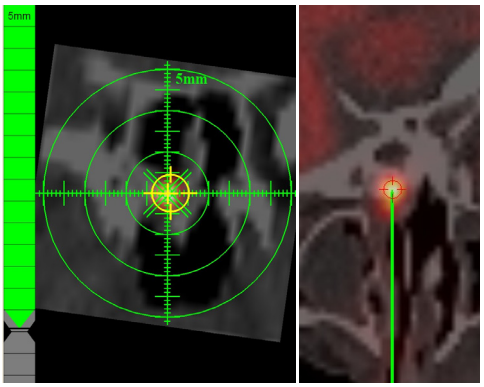

Figure 41: Overview of the instrument guidance. a) Intervention setup with image guidance (IG) system facing the surgeon. b) Close-up to the patient head and tracked instrument. c) Virtual view of the patient head and the tracked instrument displayed in the upper monitor of the image guidance system. d) Targeting viewer (left) and needle plane viewers used to guide the instrument to the target.

5.4.4 Discussions and Conclusions

This experiment evaluated the use of the developed image guidance system within a clinical environment. The qualitative results obtained with the endoscope showed the potential of the system to target such tumours. The interaction between the surgeon and the system could be performed without interfering clinical routine. The tracking capability could be provided to instruments and patient without major modification in the system workflow. According to the surgeon, the system enabled intuitive instrument guidance. The support to multimodal images helped to visualize the target as in standard clinical routine. Although quantitative evaluation is still desired, this experiment showed the feasibility of integration of the developed system in a clinical environment.

6 Tracking of Non-Rigid Anatomical Structures

Brief: In this chapter, an approach for tracking non-rigid parts of the anatomy such as chest and abdomen is proposed. The complete solution is divided in two parts: the first describing a method to provide physical reference to the patient anatomy and to automatically register the patient to the image data (presented in section 6.1); and the second describing a method to track deformable parts of the anatomy using market available tracking systems (presented in section 6.2). In section 6.3, both methods are integrated in the system for percutaneous needle interventions in order to enable a user interaction free patient-to-image registration gated interventions. Finally, section 6.4 presents a clinical case performed with the system in order to evaluate the workflow for using the single markers in percutaneous nephrolithotomy interventions.

The tracking approach proposed in this chapter relies on the placement of single retro-reflective single markers on the patient's skin to provide patient referencing based on discrete spatial surface information (see Figure 42). The retro-reflective spheres are firstly automatically detected in the CT image and thus used to initialize the tracking algorithm. The current spatial positions of the single markers are measured by means of an optical tracking system. After the proper initialization with the single markers configuration found on the CT data, the tracking algorithm can estimate the current patient pose and the current amount of deformation of the patient. Such information is afterwards used to co-display patient image and tracked needle, as well as to display the state of deformation at the region of the single markers. Relying on the visual feedback provided by the system, physicians can perform gated interventions.

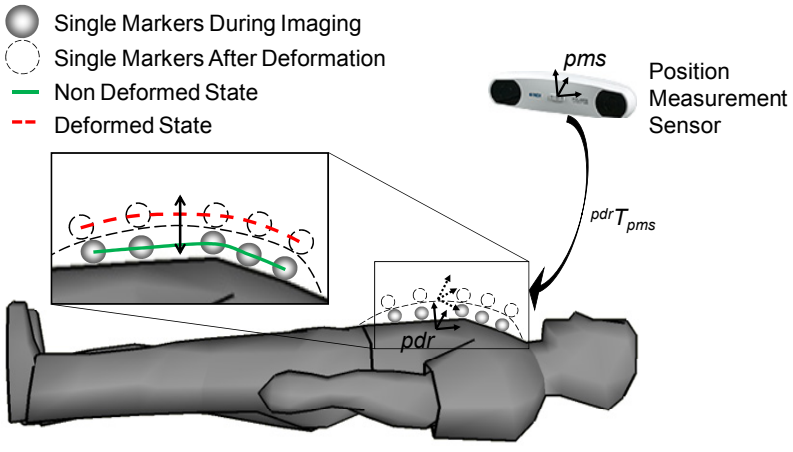

Figure 42: Overview of the patient tracking approach based on retro-reflective single. A set of single markers is placed on the patient's skin, the patient is imaged, and the position of each single marker in the image is used to initialize the tracking algorithm. Based on the position of each single marker measured by the position sensor, the tracking algorithm estimates the current patient pose, ${}^{pdr}T_{pms}$, and the amount of deformation (e.g. during breathing, going from non deformed represented in green to deformed in red).

The tracking approach presented in the section 6.1 was initially developed to track internal organs such as liver during open surgeries, which has more complex clinical environment than percutaneous interventions. Because of the flexibility and robustness of the method, an adaption from a more to a less restrict scenario could be performed without further changes.

6.1 Automatic Patient-to-Image Registration

In the next sections, a proper design and the respective method for automatic detection of single markers are investigated.

6.1.1 Single Marker Design

In order to provide a robust tracking solution, the retro-reflective single markers should be continuously visible throughout the intervention. Therefore, single markers that can be localized by the position measurement system from a wider range of positions are desired. In this section, the visibility range of a set of different single marker designs were evaluated.

Visibility Range

Three types of single markers were built, see Table 4. Type 1 comprised a retro-reflective glass sphere attached to a metal post. Type 2 comprised a retro-reflective film cut in a circular shape. Type 3 comprised a standard retro-reflective plastic sphere (from Brainlab AG, Feldkirchen, Germany) attached to a metal post.

Each single marker type was attached to a trackable metal plate. The plate was placed with its normal facing the position sensor z-axis. The angle between the plate normal and the z-axis was varied until the single markers were invisible. The range of visibility was measured considering the minimum and maximum visibility angles while varying the plate.

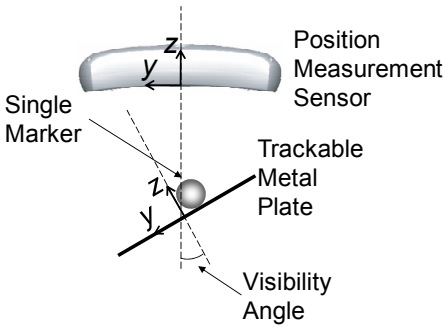

Figure 43: Illustration of the visibility angle experiment.

The results of the range of visibility are shown in the Table 4. The single marker type 3 presented the wider range of visibility.

Table 4: Description of the single marker designs with the respective visibility ranges.

Type	1	2	3
Single Marker Design	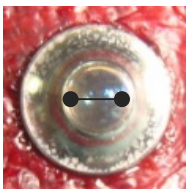	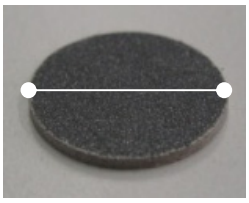	
Size (mm)	5	16	13
Visibility Angle	127°	74°	150°
Reflective Material	Glass	Retro-Reflective Film	Plastic
Post Material	Metal	-	Metal
Shape	Spherical	Flat	Spherical

Single Marker Sterilizability and Attachment

In order to provide a clinically conforming solution, several parameters were taken into account when choosing a design. Firstly, the visibility was used to select the most suitable single marker, type 3 according to Table 4. Secondly, the sterility and means of attachment were analyzed. Sterilization of the posts of the single marker type 3 can be performed with standard hospital procedures. The plastic retro-reflective spheres can be bought sterile (e.g. Brainlab). Hence, no issues were found regarding to sterilization of single marker type 3. Attachment of the single markers can be performed with standard medical tape, see an example of marker attachment procedure in Figure 44.

a) 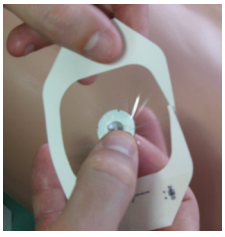 b) 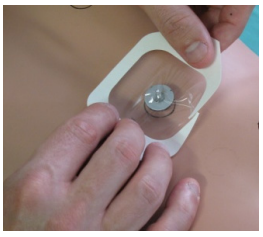 c) d)

Figure 44: Example of attachment of single markers type 3 on the patient skin with 3M™ Tegaderm™ Dressings (from 3M AG, Switzerland). a) Place post under the adhesive side if the tape. b) Place the marker post at the desired position. c) Screw the sphere in the post. d) Single marker attached to the skin.

6.1.2 Single Marker Detection on CT Images

Selection of common landmarks present in the patient and its respective image is necessary to perform a registration and align the two coordinate systems. The single markers used to provide reference to the patient are examples of landmarks that can be used for such a registration. However, a precise localization of the markers is demanded. Both materials comprising the single markers chosen in the previous section, plastic from the retro-reflective sphere and aluminium from the posts, are well visible in CT images (see Figure 45). Although the centre of the spheres can be manually selected, it introduces a level of interaction not necessary during standard clinical protocols. Furthermore, it is susceptible to physicians attention during the selection. In order to provide a patient-to-image registration approach free of interaction, the centre of single markers spheres should be automatically localized in the CT images. In this section, an approach to automatically localize the centre of the single markers retro-reflective spheres is presented.

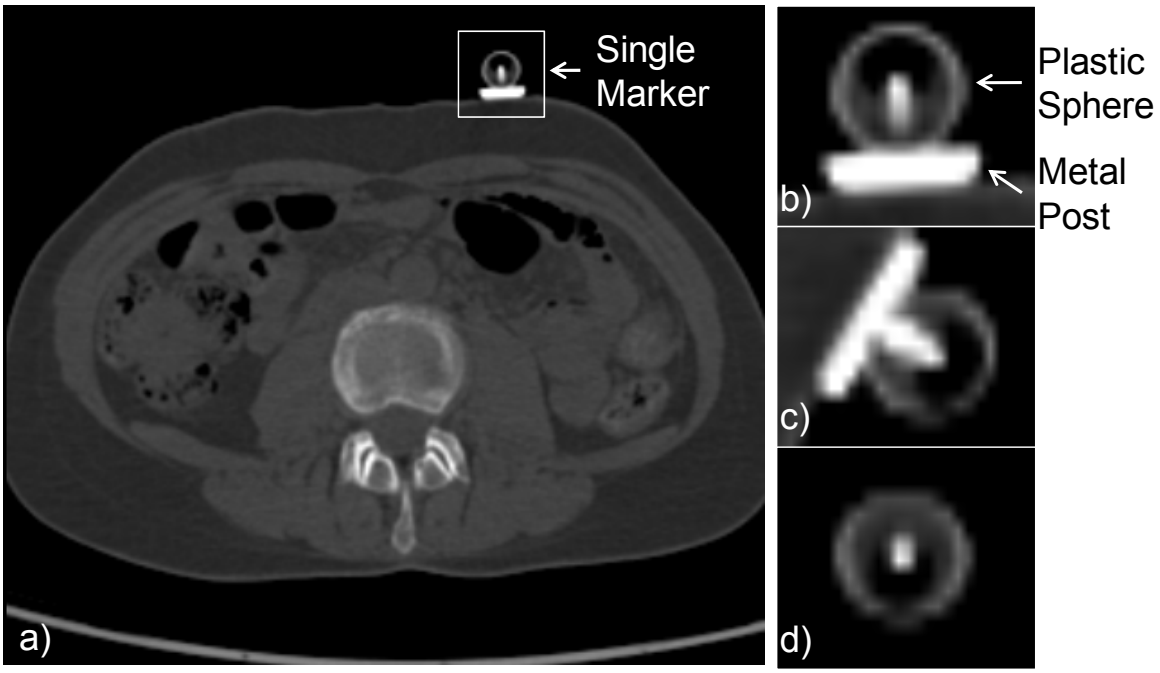

Figure 45: Example of single markers visibility in CT images. a) Axial view of a patient with a single marker attached on the abdomen. b) Axial zoom of the single marker displayed in a). c) Sagittal zoom of the single marker displayed in a). d) Coronal zoom of the single marker displayed in a).

Materials and Methods

The Hough transform [89, 90] is one of the available options to localize shapes in images. It has been mostly used to localize lines and circles in images. The objects are localized via a voting procedure carried out for each pixel of a binary image containing the searched object. The voting results are stored in an accumulator, and the objects are obtained by extracting local maxima of the accumulator. This technique is precise and robust to imperfections in the object instances. However, it demands large storage space to handle the accumulator. Furthermore, the precision of localization is influenced by the size of the accumulator. The big size of the volumetric images used for percutaneous interventions hampers the direct application of the Hough transform to precisely detect the spheres. Therefore, a hierarchical localization pipeline based on a fast 3D Hough transform is proposed.

Localization Pipeline

The localization pipeline receives as input the CT image of the patient containing a set of single markers. To handle the large size of the input image, the pipeline is divided into three steps (see Figure 46): the first in which candidates for single markers are selected; the second in which a region of interest around each candidate is extracted in order to reduce the searching space; and the third in which the sphere centre of each single marker candidate is precisely identified. As an output, a list of 3D positions of the sphere centres, ${}^{img}P_{SC}$, in the input image is given. The list is sorted by a confidence value that indicates the similarity to a spherical object. The fist n positions are chosen to represent the identified n single markers requiring localization (typically six).

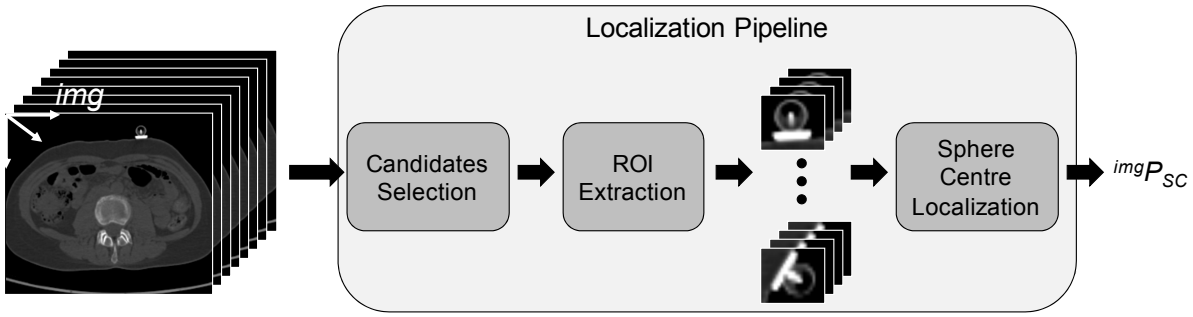

Figure 46: Localization pipeline overview. An image of the patient with the single markers is given as input. The candidate to single markers are identified. The region of interest (ROI) is extracted. The spheres of each selected ROI is identified and a list of 3D positions of the sphere centres, $^{img}P_{SC}$, in the image coordinate system is given as output.

The pipeline was implemented using the Insight Toolkit [82]. Each step of the pipeline is described below.

Candidates selection: The candidates to single marker are selected based on the posts. Because of the large volume sizes, any required pre-processing is computationally expensive. Therefore, simple pre-processing had to be used in order to ensure a feasible detection time. The intensity of metal material of the single marker posts is enough to distinguish the posts from most of the image content. A threshold can be used to quickly segment the posts, but care should be taken with noise and bone having similar intensity to the aluminium posts. The candidate selection was divided in four steps that are illustrated in Figure 47. Firstly, a Gaussian filter smoothes the image to remove possible noise (see Figure 48 for an example of image noise). Secondly, a threshold based segmentation is performed to generate a binary image containing only the single marker posts and bones. The threshold value was empirically chosen considering the maximum value of soft tissue in a calibrated CT scanner (200 Hounsfield units). Thirdly, the remaining blobs are filtered by size. All blobs with size different (within a tolerance of plus and minus the half of the post size) from the physical size of the posts are removed. Finally, a list, $^{img}P_{PL}$, containing the centre of the bounding box of each detected post is given as output.

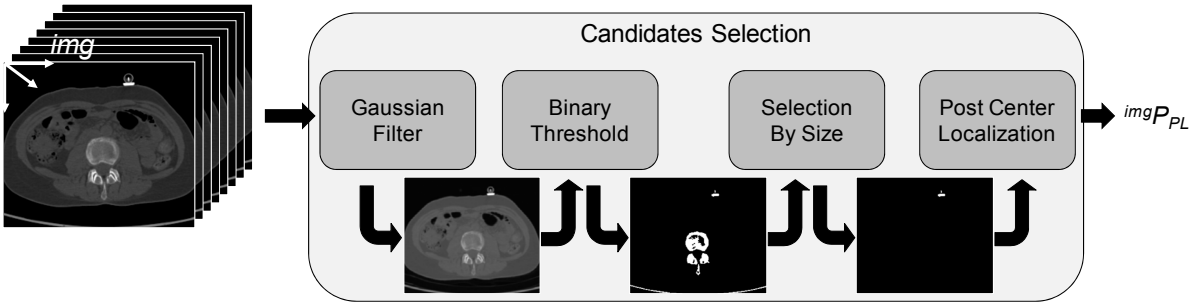

Figure 47: Overview of the steps and outcomes of the process to select candidates to single markers. An image of the patient with the single markers is given as input. A Gaussian filter smoothes the image. A threshold based segmentation eliminates the soft tissue of the image. The posts are selected considering their physical size, and a list containing the 3D position of the centre of each post bounding box, $^{img}P_{PL}$, in image coordinate system is given as output.

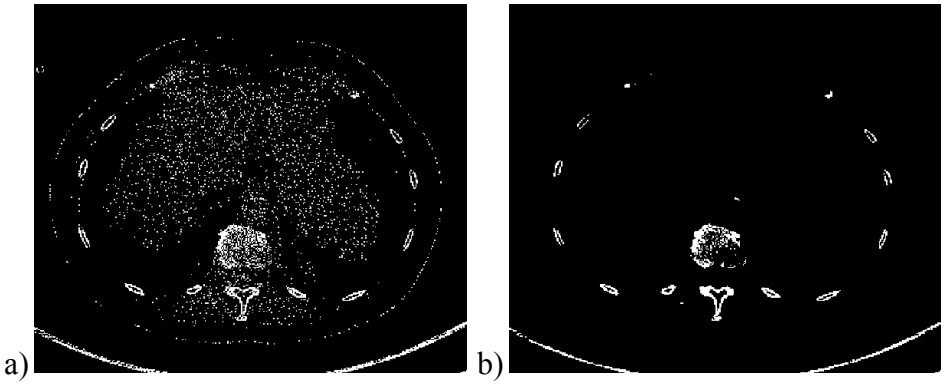

Figure 48: Comparison of threshold applied to remove soft tissue. a) Shows an example of the threshold segmentation directly applied on the image. b) Shows an example of the threshold segmentation after application of the Gaussian filter.

ROI extraction: A region of interest is extracted for each post position in ${}^{img}P_{PL}$. The size of the region of interest was defined considering the sphere radius. A value of four times the sphere radius was empirically chosen for the size of each dimension of the region of interest. Because of physical constraint, two sphere centres cannot be close together. Therefore, marker candidates that were closer than two times the sphere radius were considered only once.

Sphere centre localization: The centre of the spheres are located using a fast 3D Hough transform for spherical objects. The Hough transform typically increments every voxel of an accumulator image that respects a spatial function (of a sphere in this case) with origin in each foreground voxel of the input image. However, such approach demands high computational power and memory. In order to cope with such problems, several researches have proposed modified versions. In [91], a good summary of the improvements proposed for circular Hough transform is presented. As illustrated in Figure 49, the transform is already very computationally expensive when dealing with circles in 2D. For spheres in a 3D space, the problem is amplified even more.

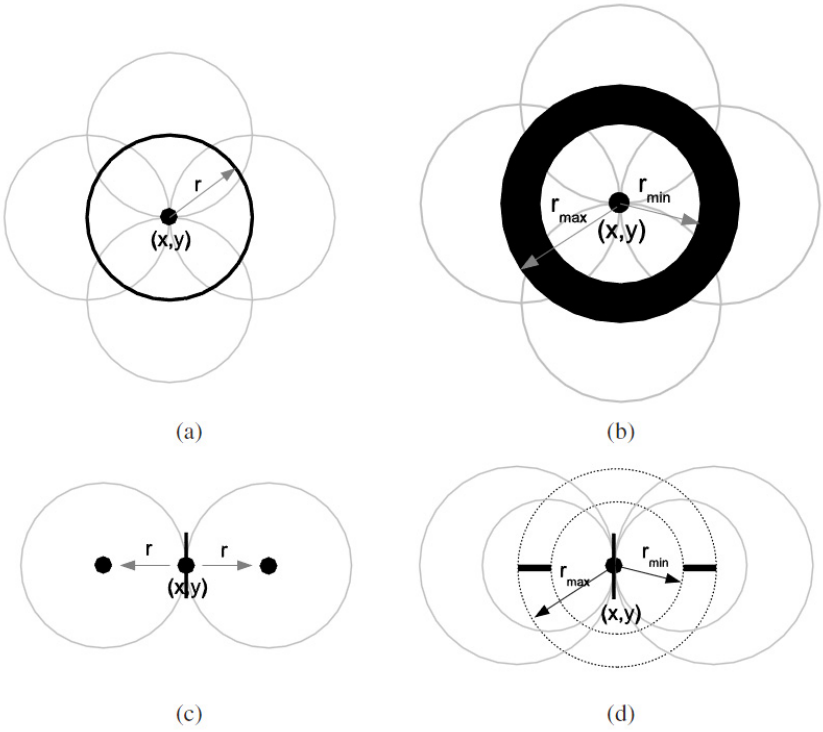

Figure 49: Voting process of a Hough transform. a) Classical circular Hough transform. b) Classical Hough transform considering multiple radii in one parameter space. c) Oriented Hough Transform. d) Oriented Hough transform considering multiple radii in one parameter space. (Source: [91])

Because the sphere to be detected have well defined parameters, several simplifications could be made in the Hough transform. The approach illustrated in Figure 49, was adapted to a 3D space and a gradient was used to define the direction of the centre. Hence, instead of voting in two directions, only one needs to be voted and a faster spherical Hough transform can be obtained. The sphere is assumed to be the foreground object. The gradient is calculated for every surface voxel of the foreground object so that the direction of voting can be decided. However, some pre- and post-processing is required in order to obtain a suitable binary image that can be used by the Hough transform and can be used to estimate the final centre. Therefore, the sphere centre localization has been divided into six steps that are described below and illustrated in Figure 50.

- **Resample**. A small region of the patient image, containing one of the single markers, is received as input. The input image is resampled in order to ensure isotropic voxels and a fixed and higher resolution. The isotropic voxels guarantee that the Hough transform spherical function is in regular 3D space. The higher resolution provides a larger voting space with subvoxel accuracy for the centre location.
- **Binary Threshold**. A threshold based segmentation selects the air content of the image. The threshold value was empirically chosen considering the maximum value for air and the minimum value for soft tissue in a calibrated CT scanner (-400 Hounsfield units).
- **Keep Largest Object**. The largest air object was selected and inverted in order to close possible holes in the sphere. Empty regions within the sphere object can disturb the gradient calculation of the Hough transform.
- **Fast Spherical Hough Transform**. The spherical Hough transform votes for the centre of the sphere in an accumulator image. As the radius of the image is well defined, the accumulator is represented by a 3D image with the same resolution and coordinates as the image of the previous step. Each voxel of the accumulator stores the number of votes for the respective location to be the centre of the sphere.
- **Gaussian Filter**. As the calculation of the centre direction is not very precise, the accumulator stores similar values for a region around the centre of the sphere. A Gaussian filter is used to average the contribution of each region around the centre. The variance was empirically chosen (to 0.5) so that the majority of the contributions are within one third of the sphere radius away from the centre.
- **Find Maxima**. The local maxima of the smoothed accumulator is identified. The voxel containing the local maxima is output as the centre of the sphere. The local maxima value is output as a confidence measurement. The confidence indicates the similarity to a spherical object.

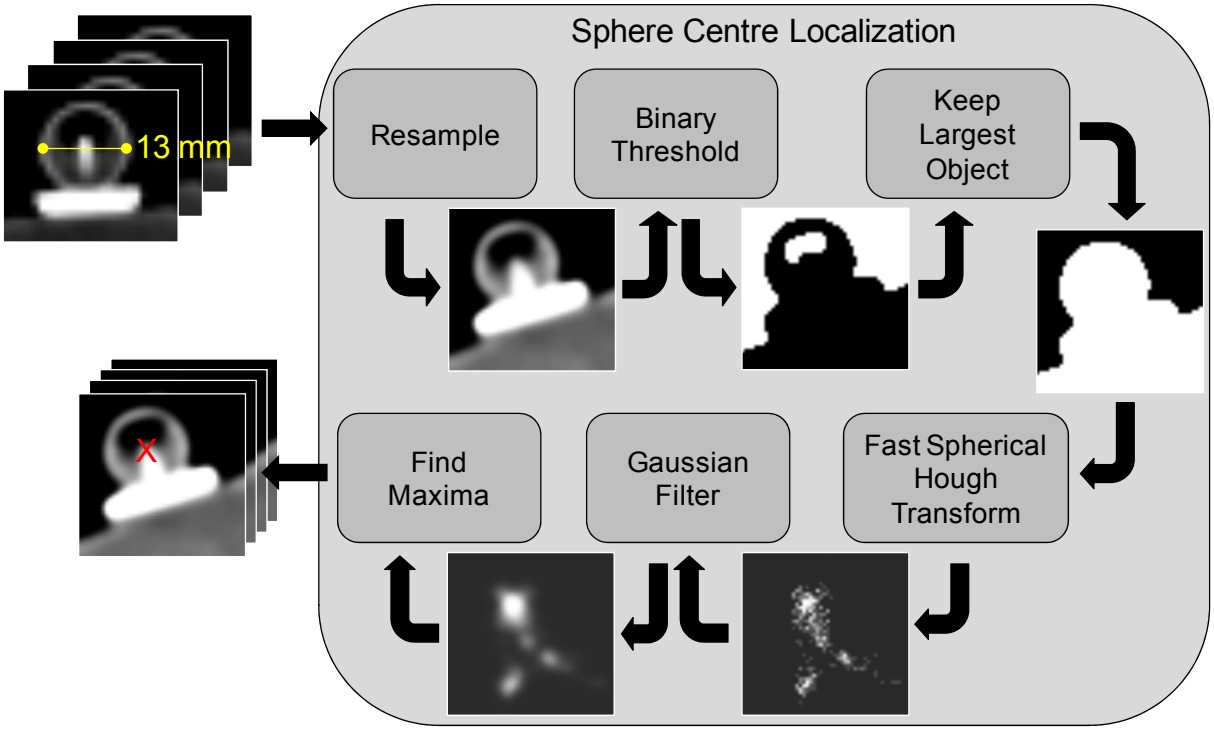

Figure 50: Overview of the steps and outcomes of the process to precisely determine the centre of each sphere. A small region containing one of the single markers of the patient image is given as input. The image is resampled to higher resolution and isotropic voxels. A threshold based segmentation selects the air of the image. The largest blob representing air is kept and inverted to background. A fast 3D Hough transform votes for pixels with high probability of being the centre of the sphere. A Gaussian adjusts the contributions of voxels within a certain region. Finally, the maxima of the smoothed image is located and used as the centre of the sphere (red cross).

Experiments

In order to evaluate the presented method, sphere localization experiments were performed. Single markers were placed on patient undergoing PET/CT intervention. A total of 54 single markers divided among 9 images were used for this experiment. The images ranged from 19660800 to 103284736 voxels with a fixed value of 512 in the x and y axis and different z values (from 75 to 394). The images were reconstructed with isotropic pixels in the axial plane (x and y axes) and with spacing ranging from 0.6 to 0.97 mm. Space between axial slices (z axis) varied from 0.75 to 3 mm. The centre of the spheres were firstly manually identified by an expert. Each sphere was localized three times and the average centre was further used as ground truth. Subsequently, the centre of the spheres were localized using the automatic approach presented above. The distance between the ground truth and each localized centre considering manual and automatic methods were measured. The time required to localize a set of six markers in each image was also measured. Experiments were performed on a computer comprising a Intel quad core i7 processor with 8 G of RAM.

Results

Results show that the localization pipeline could automatically identify the centre of all spheres with an average error of 0.35 ± 0.13 mm when compared to manual ground truth. The overall manual localization presented an average error of 0.14 ± 0.08 mm when compared to manual ground truth. Comparison of the localization error achieved for both methods is presented in Figure 51. Examples of the best and worst localization cases for the automatic method are shown in Figure 52. One marker has been excluded from the experiment because of incorrect imaging. The patient moved during CT image acquisition causing a shadow effect in the marker which hindered precise identification of the sphere centre (see Figure 53). Although the localization pipeline localized the centre of such marker with an error of 1 mm, it was not considered for these results.

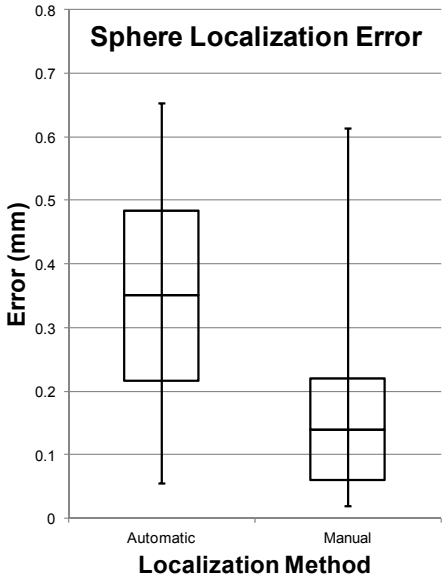

Figure 51: Comparison of sphere localization error for the automatic and the manual methods. The boxes represent the average and standard deviation errors, and the bars represent the minimum and maximum errors.

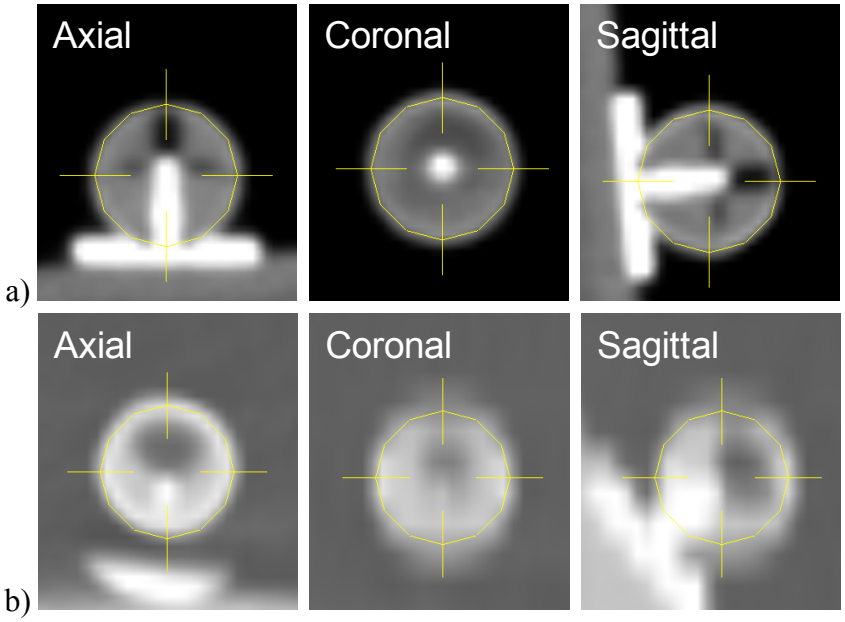

Figure 52: Example of the automatic localization pipeline results. a) Best case with an error of 0.05 mm. b) Worst case with error of 0.65 mm.

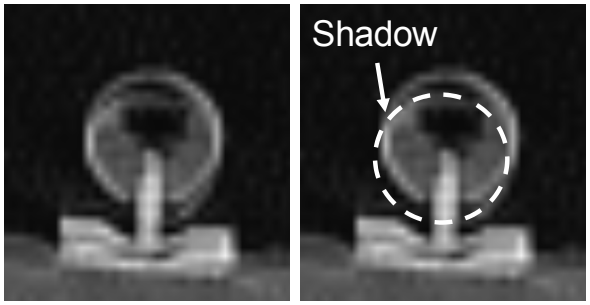

Figure 53: Axial view of the excluded single marker. The original image is showed in the left and a modified version highlighting the shadow produced is showed in the right.

The time necessary to localize six single markers in each image was 8.6 ± 1.4 and 131.0 ± 23.2 seconds for the automatic and manual methods respectively (see Figure 54a). The behaviour of the time for the automatic localization according to the image size is showed in Figure 54b.

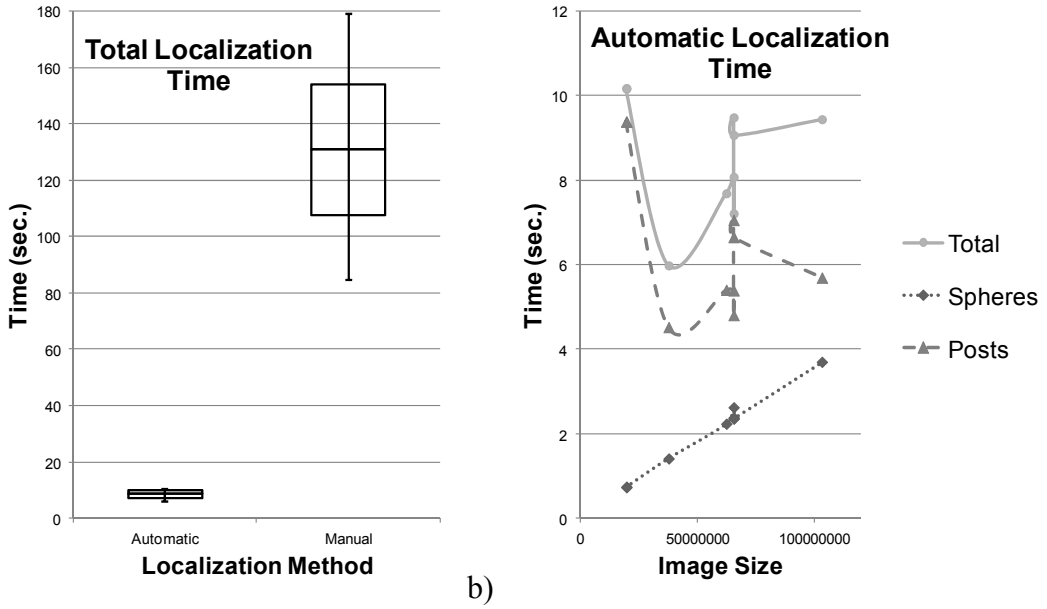

a) b)

Figure 54: a) Comparison of the single marker localization time for the automatic and the manual methods. The time represents the localization of six single markers in one image. The boxes represent the average and standard deviation time, and the bars represent the minimum and maximum time. b) The behaviour of time according to the image size. The total single marker localization time, the spheres localization time, and the posts localization time are displayed as three different curves.

Discussions and Conclusions

This section presented an approach to automatically localize the centre of the single markers retro-reflective spheres is presented. Results showed that the localization pipeline can precisely identify the centre of the single markers proposed in the previous section. The automatic localization not only eliminated the need for interaction, but also made the localization process much faster. The average localization error 0.35 mm is comparable to the order of precision of common passive tracking systems. Even considering the standard deviation of 0.13 mm , the localization error is still below half millimetre. The average automatic localization error is less the 0.25 mm higher than the manual localization. Further analysis of the worst cases showed that images with low spatial resolution contributed to the error. Such images presented blurred information that hampered correct identification of the centre (see coronal and sagittal views of Figure 52b). Even manual definition of the centre was difficult in such cases. Although not an often case, the excluded single marker (see Figure 53) showed that care should be taken to avoid movement during the imaging procedure. Considering the results for time measurements, it can be concluded that the automatic localization is around 15 times faster than the manual localization. The manual localization time is independent of the image size. Although the automatic localization depends on the image size, an extrapolation of the results displayed in Figure 54b suggests that an acceptable time can be achieved for typical clinical datasets. One of the limitations of this study is the assumption of a Gaussian for the manual selection. The ground truth was generated by averaging three different manual localizations.

Future work includes the further validation with more datasets. In addition, the part of the pipeline responsible for detecting the sphere can be used for development of a semi-automatic localization method. Such method could be initialized with a single click on the 3D viewer at the single marker region.

6.2 Anatomy Tracking for Motion and Deformation Detection

The work presented in this section was published in: T. Oliveira-Santos, M. Peterhans, S. Hofman, S. Weber, "Passive Single Marker Tracking for Organ Motion and Deformation Detection in Open Liver Surgery," in Conference Proceedings of Information Processing in Computer-Assisted Interventions (IPCAI), Berlin, Germany, 2011, LCNS 6689, pp. 156-167. ***Copyright © 2011 Springer*** *The original publication is available at: http://www.springerlink.com/content/y60n3jpv70545ug1*

Abstract. Organ motion and deformation are major obstacles hindering the introduction of image guidance into soft tissue surgery. Due to challenges with update rate, invasiveness and intra-operative complexity, there is currently no clinically established solution for deformation measurements on soft tissues. We present a soft tissue tracking approach based on single passive markers as part of a navigation system for open liver surgery. Such markers are minimally-invasive and allow for real-time organ motion measurements using available tracking systems. The absence of correspondence between position measurements over time and the sensitivity to other reflectors present within the workspace inhibit the direct clinical implementation of such technology. Hence, we remove measurement artefacts, establish marker correspondence over time, and achieve robustness against occlusions and presence of other reflecting objects. A thorough experimental evaluation demonstrates reliable motion tracking and motivates its use for deformation detection and respiratory gating in open liver surgery.

6.2.1 Introduction

Computer assistance through surgical navigation systems has been applied in many surgical domains, such as orthopaedic-, neuro-, and ENT (i.e. ear, nose and throat) surgery [24, 29, 92]. With these systems, pre-operative planning data can be co-displayed in a registered virtual context providing surgeons with intra-operative instrument guidance. The motion of rigid anatomical structures (e.g. bone, head) can be easily tracked by means of an attached dynamic reference base (DRB). Soft tissue structures, however, deform significantly during surgical interventions and this deformation cannot be detected or represented by the attachment of a DRB.

To address this problem, Vetter *et al.* [93], used electro-magnetic position measurement devices to determine the position of navigation aids anchored to the liver in order to monitor possible liver deformations. Such electro-magnetic technology, although suitable for biopsies and ablation scenarios, may be very sensitive to ferromagnetic material present in open surgeries. With a similar approach, Maier-Hein *et al.*, [56, 57, 94], proposed the use of optical position measurement devices to track needles placed in the liver and to estimate the deformation around the target. Their ex-vivo results [94] show the technique copes well with deformations present in CT-guided minimally invasive interventions. However, its applicability in a scenario where the liver is manually handled and deformed, as in open liver surgery, was not evaluated. Using a video based tracking system, Nicolau *et al.* [37, 52, 53] proposed methods for tracking and registering a radio-opaque marker set attached to the patient skin. With such techniques, soft tissue tracking can be achieved and used for radio frequency hepatic tumour ablation [37]. With a more complex setup, Cash *et al.* [74, 95] integrated a laser range scanner intra-operatively in order to digitize the exposed liver surface. The intra-operative data was then registered with the pre-operative model and a finite element approach was used to account for organ deformations. By means of available tracking systems, Markert *et al.* [96] proposed a method to track and estimate liver deformation during open surgery based on a retro-reflective single marker (SM) set placed on the liver surface. The position of each SM is detected with an optical tracking system and the liver position and deformation is estimated. The results demonstrated the feasibility of calculating the position of points on the liver surface using a SM set. Nevertheless, the robustness of the tracking algorithm was not evaluated in the study. Due to challenges with update rate, invasiveness and intra-operative complexity, there is currently no clinically established solution for soft tissue tracking.

In this work, we propose a solution to track deformable structures (e.g. liver) based on retro-reflective SMs. The differences to [96] lie in the strong focus on clinical usability and in the detailed description of a scalable and fast implementation of SM tracking using readily available position measurement systems. Such markers are minimally-invasive and allow for real-time measurement of organ surface motion while using available passive optical tracking systems. Two main disadvantages associated with this tracking technology are addressed in this work: the presence of phantom positions (i.e. position of markers not really present in the scene) and the lack of correspondence between SM positions across different tracking frames. The robustness of our SM tracking algorithm against different conditions that might be faced in the Operating Room (OR) is assessed in a lab setup. As the tracking system used to track the instruments and the organ is the same, the algorithm should handle: deformation of the organ, the presence of unexpected markers and other instruments as well as recover from partial and total occlusions. The use of pair-point rigid registration for deformation detection is also investigated. In addition, a workflow for clinical integration of the SM tracking in open liver surgery is presented.

6.2.2 Materials and Methods

The proposed solution relies on data provided by a NDI Vicra (Northern Digital Inc., Waterloo, Canada) position measurement system (*pms*) which tracks a set of SMs attached to the surface of an organ. Each SM comprises a retro-reflective sphere fixed to a post which is attached directly to a soft organ. The Vicra *pms* is configured to supply data containing the pose of each tracked DRB, plus any detected position of stray markers that are reflected in the scene and do not belong to a tracked DRB, i.e. ${}^{pms}P_{STR}$. The Vicra *pms* works as a black box that returns the transformations of the detected DRBs and positions of the detected stray markers without providing real time access to the captured images. Therefore, any possible image processing (segmentation, rectification, etc) is performed internally and is not accessible during tracking. The SM tracking algorithm uses the data supplied by the Vicra to estimate the organ (*org*) pose, i.e. the rigid transformation ${}^{pms}T_{org}$ from *org* to *pms*, as well as a set of vectors, i.e. ${}^{org}V_{SM}$, representing the deformation of the SMs in the organ (see Figure 55).

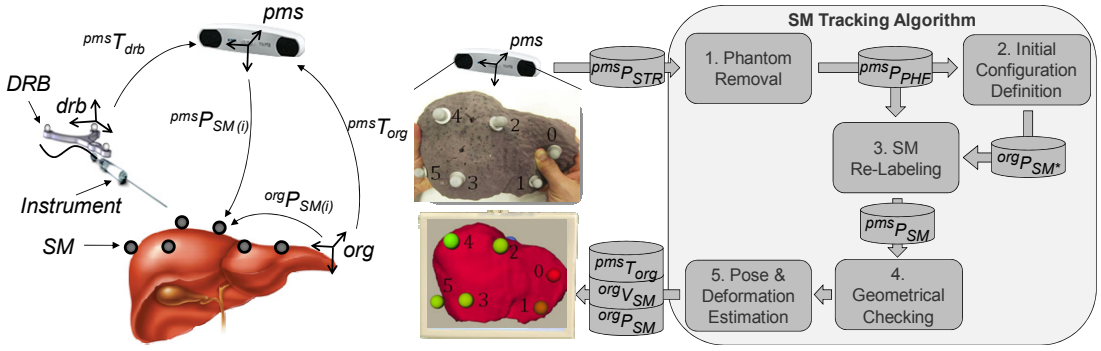

Figure 55: Illustration of the coordinate systems and transformations (left). Illustration of the data flow within the SM tracking algorithm (right).

As mentioned before, ${}^{pms}P_{STR}$ requires special handling. Firstly, phantom positions are removed. These occur when the Vicra cannot find a unique correspondence between the detected markers in both sensor images. The ambiguity appears whenever two or more markers reflecting in the scene share the same epipolar line. Theoretically, the number of phantom positions increases with the number of SMs meeting these conditions, i.e. *n* SMs in the same epipolar line would create up to $n.(n-1)$ phantom positions. Therefore, the set of positions ${}^{pms}P_{STR}$ includes not only the SM positions in the viewing volume, but also all phantom positions created according to the criteria above. Once phantom markers are removed, the correspondence between SMs of different frames needs to be established. As the *pms* relies only on information of the current frame to estimate the 3D position of a marker, the same SM on the organ surface might have a different indexes (i.e. labels) in the set of positions ${}^{pms}P_{STR}$ of different frames.

In order to evaluate the proposed solution, a navigation system [97] developed to assist open liver surgery was augmented with the SM tracking algorithm and used in our experiments.

SM Tracking Algorithm

The tracking algorithm is based on the assumptions that a non-symmetrical SM placement is chosen (e.g. not a regular grid) and that an initial configuration, i.e. the initial SM positions ${}^{org}P_{SM*}$ in the organ coordinate system, can be defined. The positions ${}^{org}P_{SM*}$ represent a tracking state without deformation. The actual SM tracking algorithm comprises 5 modules (see Figure 55 right): **1) Phantom Removal**: is continuously applied to ${}^{pms}P_{STR}$ in order to create a phantoms free set of positions, i.e. ${}^{pms}P_{PHF}$; **2) Initial Configuration Definition**: is performed once, prior to the commencement of SM tracking in order to define ${}^{org}P_{SM*}$; **3) SM Re-Labelling**: is performed at each frame to find the current corresponding SM positions ${}^{pms}P_{SM}$ in ${}^{pms}P_{PHF}$; **4) Geometrical Checking**: ensures ${}^{pms}P_{SM}$ respects the geometrical constraints set by ${}^{org}P_{SM*}$; **5) Pose & Deformation Estimation**: calculates ${}^{pms}T_{org}$ and ${}^{org}V_{SM}$ based on ${}^{pms}P_{SM}$ and ${}^{org}P_{SM*}$.

1) Phantom Removal. The SMs are assumed to lie at a similar distance to the *pms* (i.e. with the liver surface is oriented perpendicularly to the *pms*). Therefore, this module treats the situation where SMs lie more or less in plane perpendicular to the *pms* depth direction (z-axis), illustrated in Figure 56b**,** and disregards alternative situations illustrated in Figure 56a (configurations with one SM behind another from the *pms* point of view). The module relies on the CCD sensor locations within the stereoscopic *pms*, ${}^{pms}P_{S1}$ and ${}^{pms}P_{S2}$ (see Figure 57), to identify and remove the phantom positions. For every frame, a line connecting each position measurement in ${}^{pms}P_{STR}$ and the *pms* origin is calculated. The intersection between these lines and a plane (defined in front of the sensors and with normal pointing to *pms z* direction, see Figure 56) generates a set of corresponding intersection points ${}^{pms}P_{STR}'$. A phantom position $C \in {}^{pms}P_{STR}$ is likely to be generated whenever two real positions, A and $B \in {}^{pms}P_{STR}$, have their corresponding A' and $B' \in {}^{pms}P_{STR}'$ with similar x values (within a tolerance of 5 mm that was empirically chosen to capture all phantoms generated within the viewing volume of the *pms*). C is considered a phantom candidate whenever the x component of the corresponding C' has a similar value to A' or B'. Every position in ${}^{pms}P_{STR}$ has a confidence measure for being a real SM and another confidence measure for being a phantom. The confidence measure for the positions A and B to be real SMs and the position C to be a phantom are incremented by one every time the lines passing through (A,B), (B,C), and (C,A), i.e. $L_{(A,B)}$, $L_{(B,C)}$ and $L_{(C,A)}$ respectively, meet the following requirements: $L_{(A,B)}$ crosses the camera sensor plane in the *pms*'s lateral region and each of $L_{(B,C)}$ and $L_{(C,A)}$ crosses the camera sensor plane in one of the sensor regions (see Figure 57 for the definition of the regions). After evaluating all positions, the those with higher confidence measures for being real than for being phantom are assigned to the set of filtered positions ${}^{pms}P_{PHF}$. This approach eliminates phantom positions of up to two SMs sharing the same epipolar line, however it cannot remove all whenever more than two SMs meet this condition. In order to eliminate the remaining phantom positions when three SMs share the same epipolar line, the procedure described above is applied a second time to ${}^{pms}P_{PHF}$.

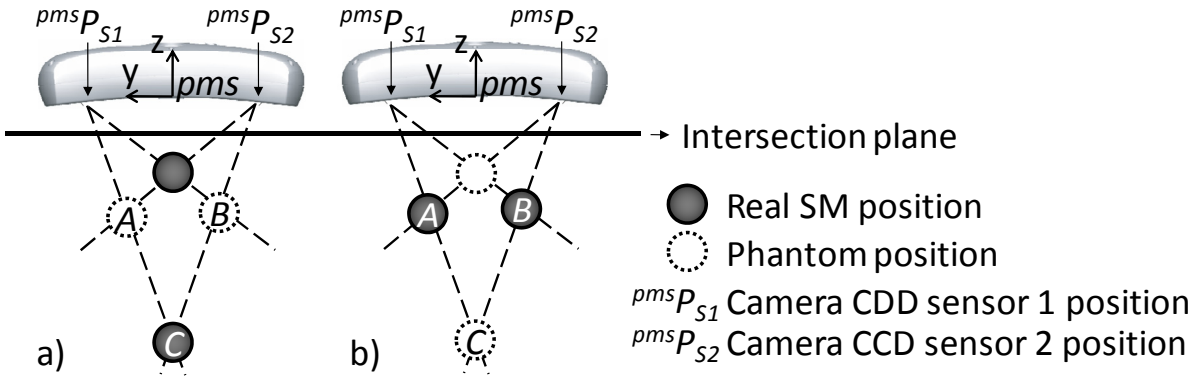

Figure 56: Illustration of two situations**,** a) and b), where phantom markers are created.

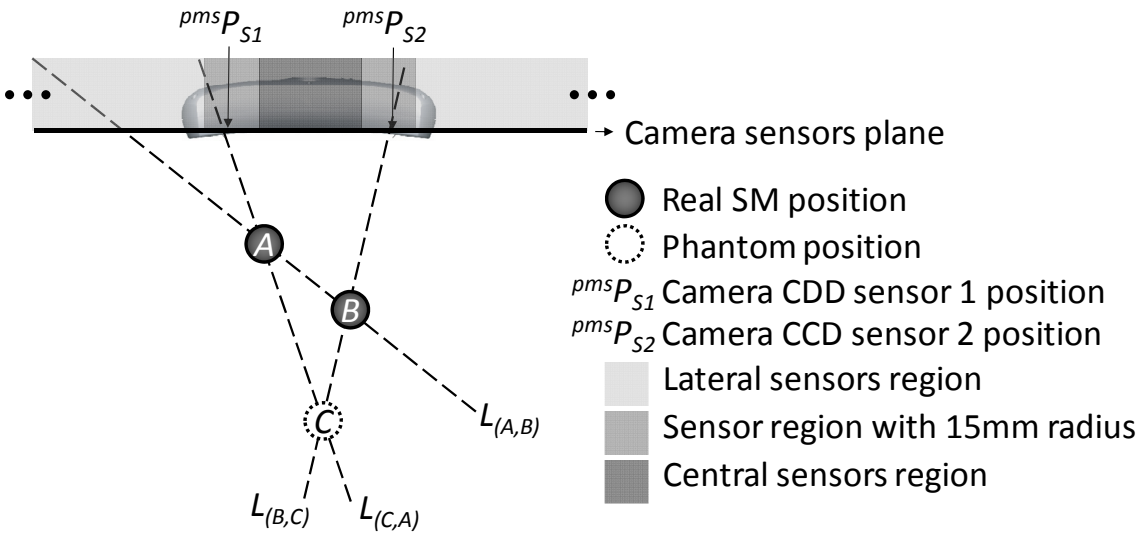

Figure 57: Illustration of the phantom removal.

2) Initial Configuration Definition. The SM configuration, ${}^{pms}P_{PHF}$, at the start of the tracking algorithm is assigned to ${}^{org}P_{SM*}$. This initial arrangement specifies a local coordinate system *org* to the tracked organ, defines a label for each SM, and imposes the geometrical constraints between them.

3) SM Re-Labelling. To re-label the positions in the current frame ${}^{pms}P_{PHF}$ according to ${}^{org}P_{SM*}$, two methods are used: *distance based labelling* and *previous-frame based labelling*. In order to give preference to the initial configuration spatial arrangement, the former is tried first and in case of failure, the latter is used.

The *distance based labelling* requires that all SMs are visible and therefore contained in ${}^{pms}P_{PHF}$. The labelling compares the distances between a position to be labelled and all the other detected positions with the possible sets of corresponding distances in the initial configuration. The label is finally assigned to the position with the most similar distances. The similarity is calculated through a cost function based on the distances $D_{SM*(i,j)}$ between every pair of SMs in the initial configuration ${}^{pms}P_{SM*}$, and the distances $D_{PHF(m,n)}$ between every pair of current measured positions ${}^{pms}P_{PHF}$, as follows:

$$c_2_{(a,b,c,d)} = \sum_{m\neq a, m\neq c}^{M} min_{n\neq b, n\neq d}^{N}(|D_{SM*(a,m)} - D_{PHF(b,n)}|) \tag{9}$$

$$c_1_{(i,j)} = \sum_{m\neq i}^{M}(min_{n\neq j}^{N}(|D_{SM*(i,m)} - D_{PHF(j,n)}|) + c_2_{(m,n,i,j)}) \tag{10}$$

$$n_c_1_{(i,j)} = \frac{c_1_{(i,j)}}{\sum_{m}^{M} c_1_{(i,m)}} \tag{11}$$

where, M and N are the number of elements in ${}^{pms}P_{SM*}$ and ${}^{pms}P_{PHF}$ respectively. The functions *c_1*, c_2 and *n_c_1* calculate the cost of position *j* to correspond to a label *i*. The cost is represented by the sum of the differences between the distance of the searched *i* and each of the remaining SMs in the initial configuration ${}^{pms}P_{SM*}$ and the most similar distance between the searched *j* and the remaining positions in the current detected positions ${}^{pms}P_{PHF}$. While *c_1* calculates the cost of the distances in the first level (from the evaluated *i* to the remaining positions *n*), *c_2* adds a second level of confidence by considering the distances from the position *n* (selected in *c_1* as the best distance to *i*) to the remaining positions. The addition of *c_2* makes the tracking more robust to ambiguous assignments. Finally, the function *n_c_1* normalizes the cost to ensure that positions with significantly smaller cost values for a certain label have higher priority. Subsequently, an exhaustive search finds the pair *(a, b)* with the minimum value in *n_c_1* and the position ${}^{pms}P_{PHF(a)}$ is assigned to ${}^{pms}P_{SM(b)}$.

Two additional terms are evaluated while assigning a position to an SM. Firstly, the difference between the distances in ${}^{pms}P_{SM}$ and the respective distances in ${}^{pms}P_{SM*}$ should be within a threshold (an empirical value of 40 mm was chosen to safely allow for organ deformation that is consistent with the

literature [98]). Secondly, the new position should not differ excessively from its corresponding position in the previous frame if it was visible (an empirical limit of 30 mm was chosen based on a maximum speed of the surgical actions and the update rate of the *pms*). The first factor limits the amount of deformation allowed, whereas the second gives priority to positions more similar to the SM location in the previous frame.

In *previous-frame based labelling*, the current position of each SM ${}^{pms}P_{SM(i)}$ is updated to the closest position in ${}^{pms}P_{PHF}$, as follow:

$$\text{If } {}^{pms}P_{SM(i)} \text{ was visible, } {}^{pms}P_{SM(i)} = closest({}^{pms}P_{SM(i)}, {}^{pms}P_{PHF}) \tag{12}$$

$$\text{If } {}^{pms}P_{SM(i)} \text{ was invisible, } {}^{pms}P_{SM(i)} = closest({}^{pms}T_{org} \cdot {}^{org}P_{SM^*(i)}, {}^{pms}P_{PHF}) \tag{13}$$

where, $closest(P_{(i)},P_{PHF})$ returns the position in P_{PHF} that is the closest to $P_{(i)}$ within a radius (set to 30 mm as above); and, ${}^{pms}T_{org}$ is the previous pose of the organ. In cases where there is no position within the defined radius, the SM is set to invisible.

4) Geometrical Checking. This module ensures that at least a minimum number (set to 4 in this study) of SMs are visible, and that the distances between the new SM positions are still below a tolerance $Threshold_{dist}$. The check is performed by comparing the distances between every two subsequent visible SMs and the corresponding distance in the initial configuration, as below:

$$|D_{SM(i,\ mod((i+1),\ M))} - D_{SM^*((i,\ mod((i+1),\ M)))}| < Threshold_{dist} = 40 \text{ mm} \tag{14}$$

In case of failure, the organ is set to invisible.

5) Pose & Deformation Estimation. In this module, the pose ${}^{pms}T_{org}$ is estimated by minimizing the square distances between SM positions in ${}^{org}P_{SM^*}$ and their corresponding positions in ${}^{pms}P_{SM}$, as proposed in [76]. The deformation represented by fiducial registration error is then calculated as:

$${}^{org}V_{SM} = {}^{org}P_{SM^*} - {}^{pms}T_{org}^{-1} \cdot {}^{pms}P_{SM} \tag{15}$$

Surgical Workflow

The surgical workflow is divided into 4 steps illustrated in Figure 58.

1) **Planning.** The surgical planning is performed pre-operatively based on a CT dataset. The liver is segmented (using MeVis Distant Services, Germany) to generate a 3D model that is uploaded to the navigation system prior to surgery.

2) **Surgical Setup.** Once the liver is stable, the SM set is attached to the organ surface with biocompatible cyanoacrylate glue [99] (tested on ex-vivo liver). A total of six SMs are placed (mostly in the area to be ressected) in order to keep a good trade-off between organ representation and the remaining working space for the surgical intervention.

3) **Registration.** Once the SM set is in place, the surgeon performs a registration of the real liver to its virtual 3D model. The point-wise registration between the 3D model and the real liver is accomplished using liver anatomical landmarks. Alternatively, other more advanced methods such as ultrasound based registration could be used. At this point, the initial configuration is defined.

4) **Instrument Guidance.** After the initial setup, the 3D model of the liver is co-displayed with the other tracked instruments. A colour coding is used to represent the deformation, $|{}^{org}V_{SM(i)}|$, of each SM (see Figure 55 right). The surgeon uses the deformation information provided by the system to identify an optimal tracking situation, i.e. where the deformation from the initial configuration is minimal.

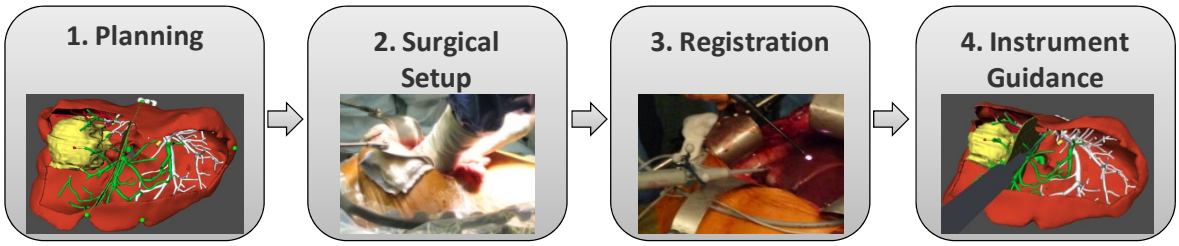

Figure 58: Surgical workflow overview.

Evaluation Experiments

A set of experiments was performed to validate the presented approach.

Organ tracking: A silicon liver was tracked by means of six SMs attached to its surface in different arrangements. Firstly, the liver was rotated in front of the position measurement system five times (each with a different SM set arrangement) by 360° so that phantom positions were produced (see Figure 59a). The rate of phantom positions produced and the efficiency of the phantom removal were measured. In a second step, the silicon liver was tracked 10 times (each with a different SM set arrangement) while evaluating different scenarios (see Table 5). A scenario was considered problematic for an arrangement if there was an error *ERR* (i.e. wrong markers assignment) at any point during tracking. The percentage of arrangements with error for each scenario was then calculated. Additionally, the processing time for the SM tracking algorithm was assessed while tracking different number of SMs.

Table 5: Scenarios applied during tracking.

M_{RIG}	Rigid Motion	Liver was moved in front of the Vicra
DEF	Deformation	Liver was deformed as illustrated in Figure 59b and c
OCC_{PAR}	Partial occlusion	Liver was partially occluded considering different SMs
OCC_{TOT}	Total occlusion	Liver was totally occluded from different sides
UR	Unexpected reflection	Four extra SMs were added to the scene
DRB	Presence of a DRB	DRB placed between the camera and the SMs

Pose estimation: To validate whether the liver pose estimated with the SM is comparable to its pose estimated with a DRB in an optimal rigid scenario, a rigid liver was tracked by means of six SMs as well as by a DRB. Four target points in the liver surface were defined relative to the DRB ${}^{drb}P_{TAR}$ and relative to the tracked organ ${}^{org}P_{TAR}$. The liver was systematically moved up and down, as well as rotated in two axes (Figure 59d). The target registration error *TRE* of these points was measured for each tracked frame using the following:

$$TRE_i = | {}^{drb}P_{TAR(i)} - {}^{pms}T_{drb}^{-1} \cdot {}^{pms}T_{org} \cdot {}^{org}P_{TAR(i)} | \quad (16)$$

Deformation identification: To show that deformation of the tracked organ can be identified, a set of seven SMs were attached to the silicon liver. One SM was used as target ${}^{pms}P_{TAR}$, whereas the remaining six were used for organ tracking. The liver was then tracked under two different scenarios illustrated in Figure 59b and c (representing diaphragm and handling respectively). The changes of ${}^{pms}P_{TAR}$ (i.e. distance from its current position to its position at the time of the initial configuration definition) were continuously measured and compared to the changes in the average deformation value $|\overline{{}^{org}V_{SM}}|$.

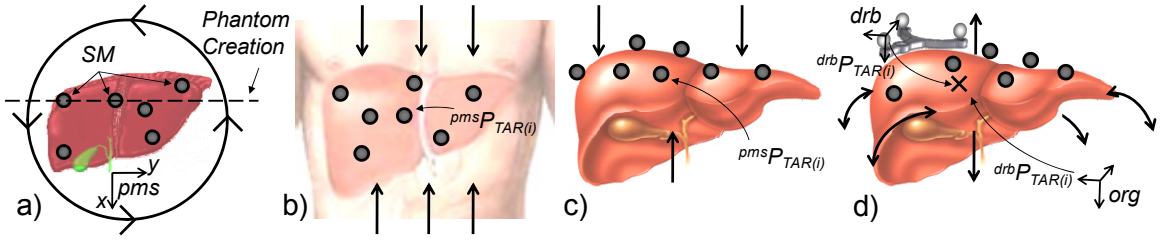

Figure 59: a) Phantom experiment: arrows represent the liver rotation. b) Axial compression: arrows represent the direction of forces applied. c) Handling: arrows represent the direction of forces applied. d) Rigid motion: arrows represent the direction of motion. Target point is represented by the x.

6.2.3 Results and Discussion

Organ tracking: The results of the first experiment in Figure 60a show that phantom positions are quite often produced by the Vicra *pms*. It can be seen that roughly one peak is obtained for any angle where one pair or three markers are coplanar with the camera centres. For all five arrangements tested, phantom positions were present in 15 % (average) of the cases while rotating the liver by 360° (1, 2, 3 and 4 phantom positions were produced in 6 %, 8.5 %, 0.3 % and 0.2 % of the cases respectively). Further analyses of the ${}^{pms}P_{PHF}$ generated during these experiments showed that the phantom removal algorithm efficiently eliminated all phantom positions produced. The results of tracking under different scenarios, presented in Table 6, show the SM tracking was robust enough to handle most of them when tracking 10 different SM arrangements. The results of the processing time experiment show that the complete SM tracking algorithm performs in 1.17, 5.01, 9.75, 12.82 and 22.84ms for 6, 7, 8, 9 and 10 SMs defining the organ respectively (on an Intel Core 2 Quad 3 GHz with 4 G RAM).

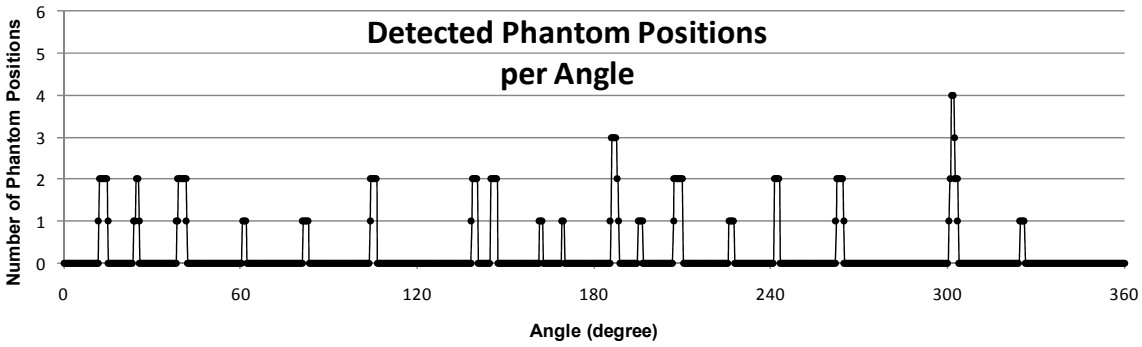

Figure 60: Frequency of phantom positions produced during one 360° rotation of the liver in front of the *pms* for one of the SM set arrangements.

Table 6: Percentage of errors (i.e. wrong marker assignments) for 10 different SM arrangements under different tracking scenarios.

Scenario	*ERR* (%)	*ERR* (%) per Scenarios Combination					
		M_{RIG}	*DEF*	OCC_{PAR}	OCC_{TOT}	*UR*	DRBs
M_{RIG}	0		0	0	0		
DEF	10			0	0		0
OCC_{PAR}	0					10	0
OCC_{TOT}	0					100	0
UR	100						
DRBs	0						

In the scenario *UR*, tracking was mostly stable whilst moving the extra SM in the scene. Errors occurred in 100 % of the arrangements when one extra SM was close (less than 50 mm) to one of the SMs on the organ and between its line-of-sight with the Vicra. In this case, the extra SM took over the label of the covered organ marker. Nonetheless, the label was again correctly assigned as soon as the extra maker stopped occluding the SM on the organ, and therefore was not considered a major concern. In the scenario combination *UR* + OCC_{TOT}, errors were also present in 100 % of the cases when

recovering from a total occlusion with extra SMs continuously placed close to the SMs on the organ. The extra SMs assumed the label of some of the organ SMs which were still occluded and the correct label assignment could only be recovered after occluding the extra SMs. However, this is not expected to happen very often in the OR and can be avoided by identifying and covering the unexpected reflections in the scene. The same case also occurred with partial occlusion of the organ SMs (scenario combination $UR + OCC_{TOT}$), but only for one arrangement. Confusion of the organ SMs with the DRB geometries defined in the position measurement system occurred for one SM arrangement while deforming the liver (scenario *DEF*). However, it only caused the organ to be invisible for a few milliseconds because the respective SMs could not be detected by the position measurement system in this case. This situation as well as possible wrong label assignment due to bad SM arrangement choice, can be avoided by providing position profiles to the surgeon. Such profiles can guide the surgeon roughly during the SM attachment in order to have a pre-optimized SM arrangement.

Pose estimation: The results in Figure 61 left show that the average differences in the localization of 4 target points by a rigid DRB and by a set of SMs are below 0.2 mm. The maximal differences of 0.9 mm could be attributed to tracking errors (i.e. fitting error to the pre-defined geometry) on both, the DRB (*DRB Err*) and the SMs (*SMs err*). These errors are not correlated with each other (correlation value of 0.2), but are correlated with the TRE of the target points on the organ (correlation values of 0.6 and 0.59 respectively). Figure 61 right illustrates the correlation between the TREs and the *DRB Err* and shows how the localization error is propagated to the targets.

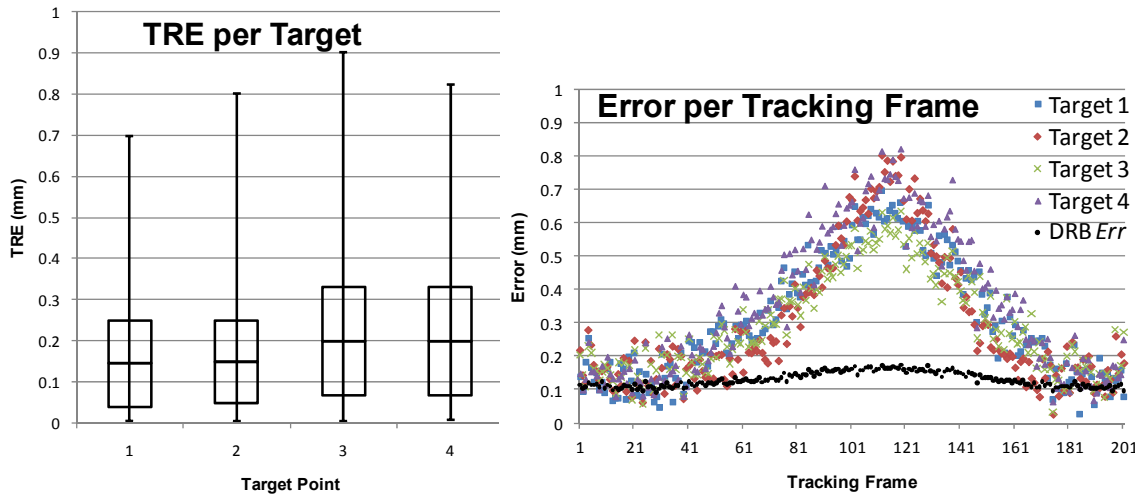

Figure 61: (Left) Boxplot of TRE values for the 4 targets for 5 SM arrangements. (Right) Difference in target localization and DRB fitting error for one of the SM arrangement.

Deformation identification: The curves in Figure 62 show a comparison between deformation measurements obtained from averaging the SM errors and the local motion measurement on a single point of the silicon phantom. The strong correlation of 0.98 and 0.96 between the two curves in Figure 62a and b respectively indicates that organ deformation can be reliably detected using SMs.

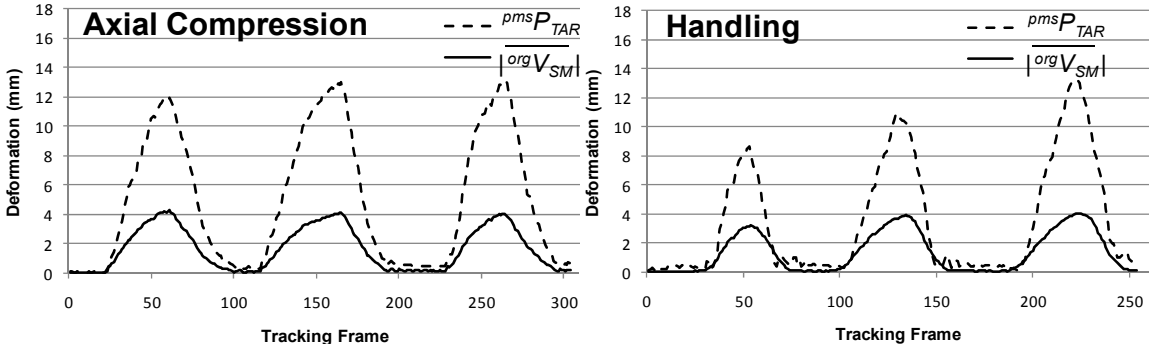

Figure 62: Comparison of deformation measured by single markers and one evaluation point under axial compression and simulated surgical handling of a silicon liver phantom.

6.2.4 Conclusions

This paper presents an approach for soft tissue tracking based on passive single markers attached to an organ surface that are tracked by an optical sensor. Our experiments demonstrated that our approach is capable of tracking deformable organs, such as the liver, in real time and under different constraints, representing real OR conditions. It was also demonstrated, that a tracking accuracy, comparable to rigid reference bases (i.e. tracker) could be achieved throughout real world conditions. The evaluation scenarios were chosen with focus on the clinical application and considering the experience gained in previous navigated liver surgeries [97]. Additionally, tracking of a soft organ using single optical markers allows for precise detection of its deformation state. Although, deformation of the soft organ can be detected using the described approach its compensation must still be addressed in the future. An algorithm is described to identify false positive phantom markers that are detected by the optical tracking system. These phantom markers are successfully neglected throughout the further processing of the tracking information. To cope with the dynamic OR environment, our approach can recover from occlusions of some or even all the single markers. A main advantage is the possibility to combine single markers and rigid references together in one workspace, allowing for a simultaneous tracking of instruments and the organ in real time.

Although this approach to soft tissue tracking was evaluated only under laboratory conditions, we believe that it will be possible to transfer into a clinical environment and ultimately deploy in computer-assisted liver surgery.

6.3 Integration into Percutaneous Needle Guidance

In order to integrate the methods presented above in the developed navigation system, modification of the some system modules presented in the section 5.1 was required.

Firstly, new guidance information was included in the instrument guidance module to provide visual feedback about the current patient deformation. The 3D viewer was equipped with the virtual spheres representing the current state of the single markers and with a surface mesh connecting each sphere centre. The mesh was generated using a 2D Delaunay triangulation algorithm (see the visualization toolkit (VTK) [100]) with the plane defined by three of the tracked spheres. The fiducial registration error obtained for each single marker, $|^{org}V_{SM}|$, is used to colour code the each corresponding virtual sphere and the mesh. A second deformation viewer provides information about the overall patient deformation around the tracked region. The deformation viewer display the average fiducial registration error, $|\overline{^{org}V_{SM}}|$, over time. The cyclic error visualization provided by this viewer during tracking of regions affected by breathing allows physicians to give voice command to the patient in order to obtain an optimal static scenario for puncturing.

a) 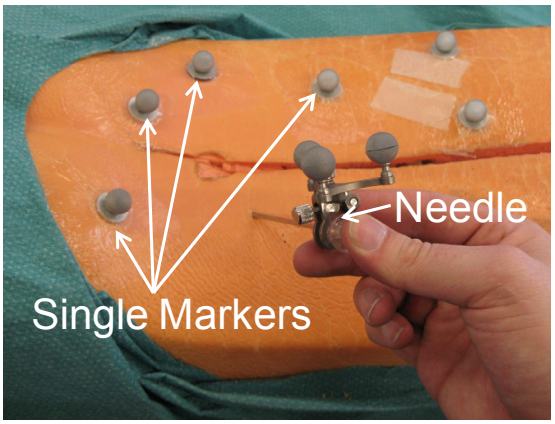

b) 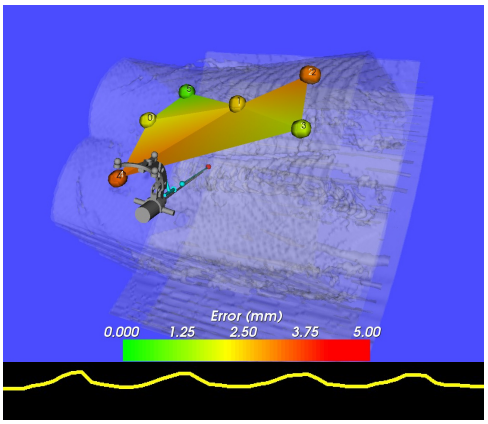

Figure 63: Example of tracking under deformation. a) Deformable phantom with a set of six single markers and a needle being guided to the target. b) Viewers displaying the guidance and deformation information. The top viewer displays an overview of the intervention scenario with the needle and the individual error of each marker. The bottom viewer displays average fiducial registration error over time.

Finally, four points of the system workflow were changed to incorporate the new methods. The modification eliminated the need user interaction when locating the spheres centres in the CT, and introduced the deformation information during the instrument guidance. The changes in the system workflow are described in detail below and illustrated in the Figure 64.

- **Patient Preparation.** Mostly, the patient preparation is accomplished in the same manner as before. However, the single markers are placed on the patient skin instead of a rigid DR.
- **Marker Detection.** After loading the images in the system, the single marker spheres centre are automatically recognized. The set of positions detected is used as the initial configuration required by the tracking algorithm presented in section 6.2.
- **Patient-to-Image Registration.** The patient-to-image registration is no longer performed as a separate step. After the initialization of the tracking algorithm, the registration is performed by the tracking algorithm after every tracking frame obtained by the position measurement system.
- **Instrument Guidance.** Firstly, the physician uses the deformation visual feedback provided by the navigation system to find the best point in time to ask the patient to hold the breath. Finally, the physician steers the needle to the bone surface or target, in case of bone or soft tissue interventions respectively. More than one breath hold commands might be necessary before reaching the target.

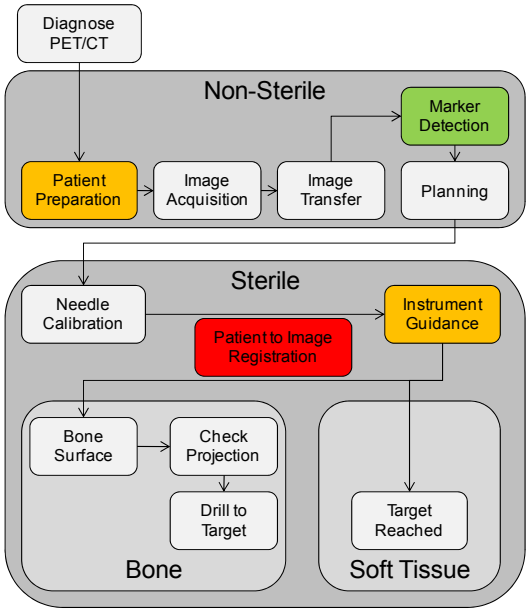

Figure 64: Overview of the changes performed in the system workflow to incorporate the tracking of non-rigid structures approach presented above. The patient preparation was altered (orange) to include the single markers placement. The automatic single marker detection was added (green) to reduce the necessary user interaction. Patient-to-image registration (red) is now continuously performed in the during instrument guidance. Instrument guidance (orange) was altered to include deformation information.

6.4 Clinical Experiment: Percutaneous Nephrolithotomy Intervention

In this section, a clinical case of percutaneous nephrolithotomy addressed with the developed system is presented. Percutaneous nephrolithotomy intervention is not performed with the patient in the same location and position as the image acquisition. Such changes might introduce additional deformation to the intervention scenario. In this experiment, a passive evaluation was performed in order to validate the workflow of single markers placement during percutaneous nephrolithotomy intervention. Additionally, the intra-intervention deformation according to the imaged scenario was measured. Al-

though needle guidance was provided by the system, such information was not used by the surgeon during this experiment.

6.4.1 Introduction

A patient was diagnosed with stones accumulated in the kidney (see Figure 65). Therefore, percutaneous nephrolithotomy was necessary to access the kidney collecting system and remove the stones.

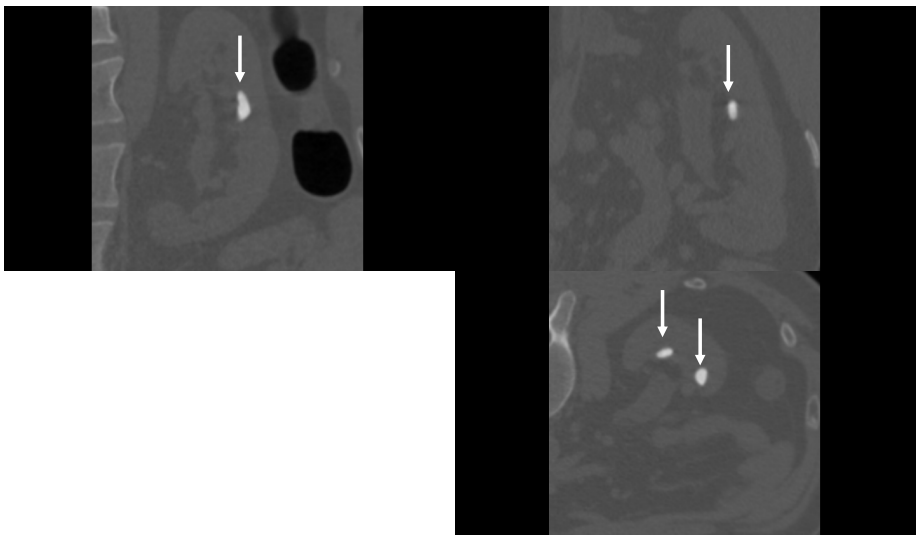

Figure 65: Kidney stones (arrows) showed in the axial (lower right), sagittal (upper right), and coronal (upper left) slices of a diagnose CT of the patient.

6.4.2 Materials and Methods

The system presented in the previous sections have been used to support the mentioned intervention. The dynamic references, clamps and calibration unit were sent along with the standard instruments to sterilization. The image guided percutaneous nephrolithotomy was performed in two steps: a pre-interventional and a intra-interventional. The first was realized one day before the intervention, whilst the second was realized at the day of the intervention. Each step is described in detail below.

Pre-Interventional Step:

- **Single Markers Placement.** The single markers were placed on the patient skin according to Figure 66. The location of the each single marker was kept for the intervention day.
- **Image acquisition**. A CT image of the patient with the single markers was acquired (see Figure 66d).
- **Image Transfer**. The CT image was transferred to the navigation system.
- **Planning**. Trajectories comprising a target and a needle entry point were planned (see Figure 67 for an example). The trajectories were saved for later access.

Intra-Interventional Step:

- **Patient Preparation**. At the day of the intervention, anaesthesia and retrograde, transurethral insertion of a urethral catheter for filling of the collecting system in the kidney was administered with the patient in the supine position. The patient was then placed in the final surgical position, and the single markers were attached on his skin at the same positions as the image acquisition (see Figure 68).
- **Planning**. The planned trajectories were loaded in the system.
- **Instrument Calibration.** The needle optical reference was attached and its tip position and axis orientation were calibrated relative to the needle tracker coordinate system.
- **Instrument Guidance**. The system automatically detected and registered the patient to the image. The surgeon performed the procedure as usual. The needle guidance information was

not used by the surgeon. The tracked position of the single markers as well as the deformation information have been stored during several points of the intervention.

a) 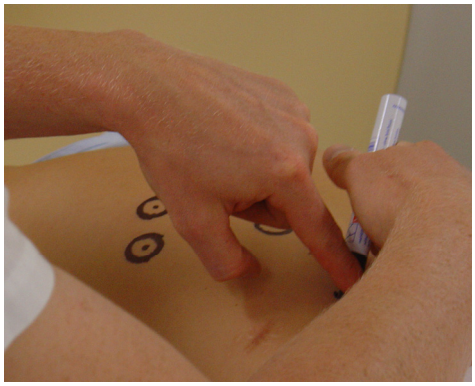

b) 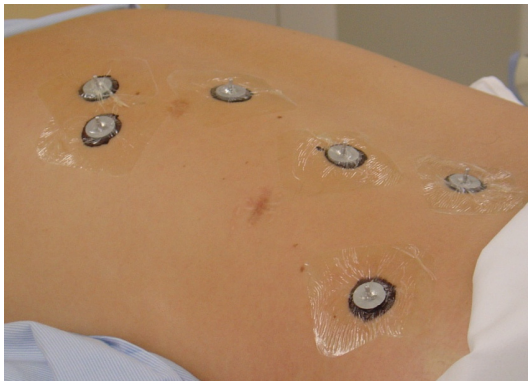

c)

d) 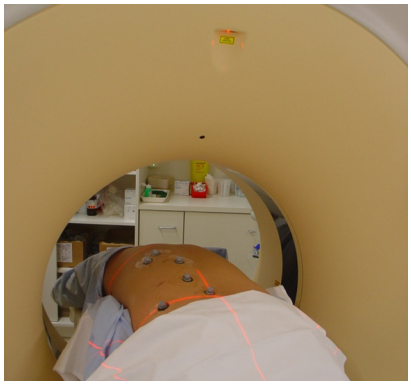

Figure 66: Overview of process to attach the single markers for image acquisition of percutaneous nephrolithotomy interventions. a) Draw the position of each single marker with a surgical pen. b) Attach the single marker posts with 3M™ Tegaderm™ Dressings. c) Screw spheres on the posts. d) Acquire CT image of the patient including single markers and kidney.

a) 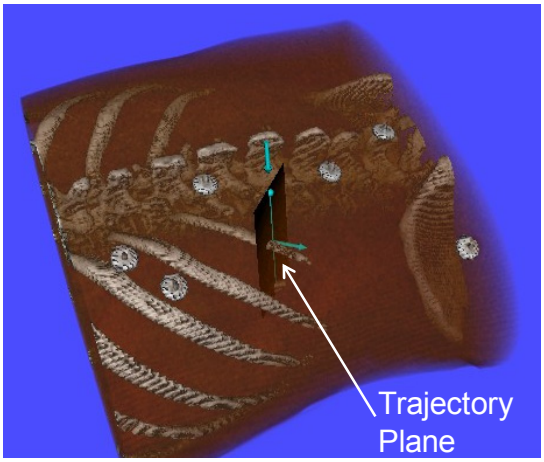

b) 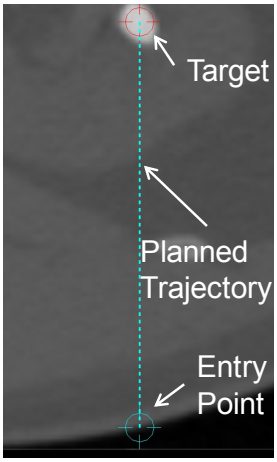

Figure 67: Example of a planned trajectory. a) Volume rendering of the patient with the planned trajectory. b) Trajectory plane (located at position showed in a)) showing the planned trajectory comprising a target and an entry point.

a) 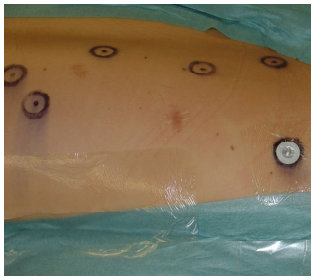 b) c) 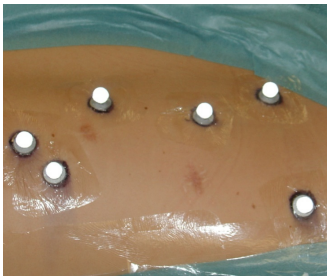

Figure 68: Overview of process to attach the single markers for patient referencing during percutaneous nephrolithotomy interventions. a) Attach the single marker posts with 3M™ Tegaderm™ Dressings at the marked positions. b) Screw sterile spheres on the posts. c) Final sterile single markers arrangement.

In addition to the clinical percutaneous nephrolithotomy case, two other experiments were performed in a laboratory setup: one to determine the error related to the single markers re-attachment at the day of the intervention, and another to determine the error of re-positioning the patient on the intervention table according to the imaging day. For the first additional experiment, a set of six single markers were attached on a volunteer similarly to the image acquisition. A state of normal expiration was defined as the initial configuration of the single markers. Finally, the single markers were re-attached 5 times and tracked for three breathing cycles. The point of lowest fiducial registration error of each re-attachment was chosen as the best match. For the second additional experiment, a set of six single markers were attached on a volunteer lying on a table. A state of normal expiration was defined as the initial configuration of the single markers. The volunteer as asked to stand up and lay down five times. The position of the volunteer on the table was adjusted by user of the navigation system according to the visual feedback provided by the single markers tracking. Finally, the single markers were tracked for three breathing cycles after each re-positioning. The point of lowest fiducial registration error of each re-attachment was chosen as the best match. Both experiments were performed on a operation room table simulating the position of the patient during percutaneous nephrolithotomy interventions.

6.4.3 Results

A suitable configuration for the navigation system and workflow could be found (see Figure 69a). The average fiducial registration error of the 33 measurements stored during the intervention was 9.0 mm (see Figure 69b for an overview of all measurements).

a) 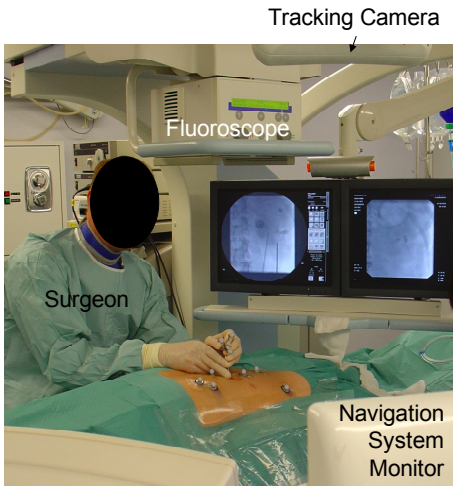

b) 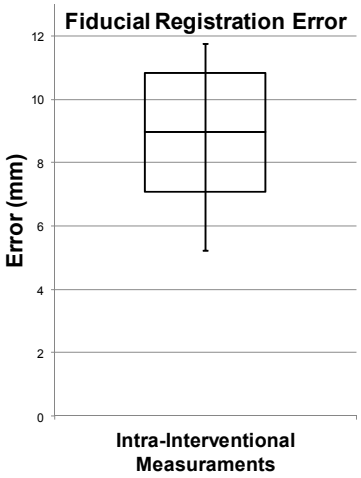

Figure 69: Overview of the percutaneous nephrolithotomy intervention. a) Surgeon guiding the needle to the kidney collecting system. b) Fiducial registration error of the single marker set for the 33 measurement stored during the intervention. The boxes represent the average and standard deviation error, and the bars represent the minimum and maximum error.

The average fiducial registration error of the five trials performed in the single markers re-attachment and patient re-positioning experiments were 1.2 mm and 0.9 mm respectively. See Figure 70 for an overview of the results for each trial.

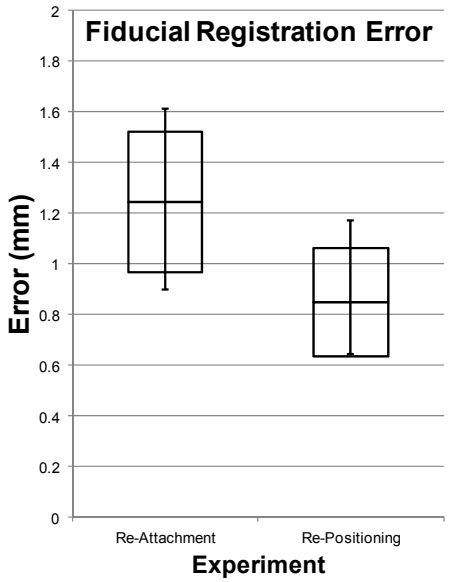

Figure 70: Fiducial registration error of the single marker set during the single markers re-attachment and patient re-positioning experiment. The boxes represent the average and standard deviation error, and the bars represent the minimum and maximum error.

6.4.4 Discussions and Conclusions

This experiment evaluated the workflow of single markers placement during a percutaneous nephrolithotomy intervention. In addition, it measured different sources of deformation, i.e. fiducial registration error, in the intervention. The necessary workflow for using the single markers could be performed without interfering with clinical routine or significantly increasing the patient preparation time. A suitable configuration could be found for placing the system in the intervention room. Existing equipment such as fluoroscope did not interfere with the visibility of the markers. Excessive deformation (9.0 mm in average) was measured during the intervention. Additional experiments demonstrated the feasibility of re-attaching the markers and re-positioning the patient to an optimal position (average error of 1.2 mm and 0.9 mm respectively). Based on such results, one can conclude that a different source introduces deformation to the intervention. A possible source is the filling of the collecting system in the kidney. While the kidney is empty during the imaging process, it is full during the intervention. Such difference might deform the marker set arrangement which cannot return to the imaged configuration. In order to cope with such cases, additional means of registration (such as ultrasound based) should be investigated. Ultrasound image can provide an intra-intervention view of the kidney to be registered with the pre-acquired CT image. After proper alignment of the pre- and intra-intervention scenarios, the single markers can be used to enable gated procedures.

7 Projection of Needle Guidance Data on Patient

Brief: In this chapter, an augmented reality visualization approach to eliminate the need for sight diversion is presented.

7.1 Portable Image Overlay Projector

The approach presented in this chapter is based on a portable image overlay projector device proposed by Gavaghan *et al.* [101]. The projector was initially developed to increase intuitiveness of computer aided liver surgery by eliminating the need for sight diversion from the patient during the intervention. However, the good results obtained with the device have motivated investigation with other applications. The approach has been thus integrated in the implemented navigation system for percutaneous interventions to provide needle guidance information directly on the view of the patient. The usability of the image overlay device has been evaluated with a set of phantom experiments under various application scenarios including percutaneous interventions. Such evaluation is presented in the following section.

7.2 Augmented Reality Applications

The work presented in this section was published in: K. Gavaghan, T. Oliveira-Santos, M. Peterhans, M. Reyes, H. Kim, S. Weber, "Evaluation of a portable image overlay projector for the visualisation of surgical navigation data: phantom studies", International Journal of Computer Assisted Radiology and Surgery, 2011, In Press. ***Copyright © 2011 Springer****. The original publication is available at: http://www.springerlink.com/content/8352445128682685/*

Abstract. Presenting visual feedback for image guided surgery on a monitor requires the surgeon to perform time consuming comparisons and diversion of sight and attention away from the patient. Deficiencies in previously developed augmented reality systems for image guided surgery have however, prevented the general acceptance of any one technique as a viable alternative to monitor displays. This work presents an evaluation of the feasibility and versatility of a novel augmented reality approach for the visualisation of surgical planning and navigation data. The approach which, utilises a portable image overlay device, was evaluated during integration into existing surgical navigation systems and during application within simulated navigated surgery scenarios. A range of anatomical models, surgical planning data and guidance information taken from liver surgery, craniomaxillofacial surgery, orthopaedic surgery and biopsy were displayed on patient specific phantoms, directly on to the patient's skin and on to cadaver tissue. The feasibility of employing the proposed augmented reality visualisation approach in each of the four tested clinical applications was qualitatively assessed for usability, visibility, workspace, line of sight and obtrusiveness. The visualisation approach was found to assist in spatial understanding and reduced the need for sight diversion throughout the simulated surgical procedures. The approach enabled structures to be identified and targeted quickly and intuitively. All validated augmented reality scenes were easily visible and were implemented with minimal overhead. The device showed sufficient workspace for each of the presented applications and the approach was minimally intrusiveness to the surgical scene. The presented visualisation approach proved to be versatile and applicable to a range of image guided surgery appli-

cations, overcoming many of the deficiencies of previously described AR approaches. The approach presents an initial step towards a widely accepted alternative to monitor displays for the visualisation of surgical navigation data.

7.2.1 Introduction

The previous two decades have seen an increase in the use of tools for pre-operative planning and intra-operative guidance. Surgical navigation systems and pre-operative planning tools rely on imaging data to assist in the definition and conduct of surgical procedures and in the identification of critical anatomical structures. Patient specific anatomical models can be constructed from medical image data, allowing surgeons to visualize target and risk structures in 3D alongside surgical plans and guidance information. Preoperatively, such data aids in the definition of resection planes, trajectories and surgical approaches. Intra-operatively, virtual reality (VR) data registered to the patient displayed alongside guided surgical tools and guidance visual feedback, assists in the successful completion of the planned surgical approach, in the localisation of hidden target structures and in the prevention of injury to surrounding tissues.

Primarily, surgical planning and navigation data is displayed on nearby 2D monitors; however, this approach requires the surgeon to divert his sight and attention between the virtual information on the screen and the patient. Error and excess surgical time introduced due to a lack of intuitiveness and reduced patient attention has called for the development of alternative data visualisation methods. Augmented reality (AR), the fusion of real world and virtual data in a single view, allows such deficiencies to be overcome by displaying navigation data directly in the view of the patient. The advantage or AR to a range of surgical applications has been previously identified and reported.

In navigated soft tissue surgery, the display of 3D models of critical and target structures such as blood vessels and metastases aids in the definition and conduct of surgical procedures. However, authors such as Hansen *et al.* [102] and Sugimoto *et al.* [103] have reported on the disadvantages of displaying navigation data on a separate screen. Hansen concluded that mental fusion of planning models with the current surgical view was error-prone and that it frequently resulted in distracting comparisons during the intervention that consumed an unacceptable amount of time. Hansen proposed the idea of using AR technologies such as projection or image overlay for improved visualisation of navigation data but is yet to describe an implemented functional system for doing so. Sugimoto *et al.* described the use of standard data projectors for 2D image overlay AR in soft tissue surgery; however, the set up suffered from a lack of flexibility and a lack of accurate registration techniques and patient movement handling.

In cranio-maxillofacial (CMF) surgery, several authors have described the benefits of AR systems for procedures such as post-traumatic trauma reconstruction [104] and bone resection [105]. Wagner *et al.*, attempted to overlay preoperatively planned resection lines for mandibular osteotomies using head mounted displays and image overlay technology [105]. The technique provided reasonably accurate image overlay for surgical guidance of resection areas but required complex patient to virtual data registration and intrusive head gear to be worn by all operating physicians.

In [106] and [107], Blackwell and DiGioia *et al.* described the benefits of applying AR technologies to a range of navigated orthopaedic surgeries including arthroscopy, joint replacement and tumour removal. They proposed the use of semi transparent displays to give the illusion of navigation data floating within the underlying patient. The approach was initially promising but the need for obtrusive equipment around the surgical scene and the associated limited workspace, long setup times and complex calibrations prevented the widespread use of the approach in navigated orthopaedic or any other form of surgery.

In minimally invasive and percutaneous interventions for which visual feedback is greatly limited, the need for surgical guidance is evident. In [108], Schwald *et al.* described the application of semi-transparent display AR to minimally invasive surgery however, the technique suffered from the disadvantages described above in addition to insufficient accuracy. In more recent work, Liao *et al.* have presented a system for semi-transparent display AR guidance based on auto stereoscopic technology [109]. Initial experimental results suggest that such an elaborated system can provide AR to several observers without presenting parallax problems and without additional head mounted equip-

ment such as displays or trackers. Although such a sophisticated method may present an AR solution for certain minimally invasive procedures, current auto stereoscopic displays still suffer from poor image resolution, blind spots along the field of view and cause visual sickness to certain range of observers making it unsuitable for some applications.

In addition, a number of other groups have developed AR approaches based on image overlay [110], semitransparent displays [106–108] head mounted displays [111, 112] and 2D projection [103, 113, 114] for specific clinic applications which have been applied with varying success. Overcoming deficiencies in limited workspace, obtrusive equipment requirements, elaborate set up times and reduced surgical vision appears however, to be paramount to the widespread acceptance of a single AR approach as an alternative to monitor display in navigated surgery. In addition, a single technique that can be used in a range of image guided surgeries, without the need to replace existing verified image guidance systems will inevitably enhance the general acceptance of an AR approach.

A portable projection image overlay device (IOD) [101] developed within our institute, displays medical data directly on the patient and overcomes many of the deficiencies of previously described AR approaches. The device is minimally intrusive, non-impeding to the view of the surgeon, and efficient in setup and movement handling. Accurate patient registration and patient and tool tracking are realised through the integration of the device into existing surgical navigation systems with verified registration and tracking frameworks.

In an attempt to evaluate the feasibility and versatility of the image overlay projection device as an alternative tool for surgical planning and navigation data visualisation, we herein present an evaluation of the device within the four surgical applications described above; navigated soft tissue surgery, navigated CMF surgery, navigated orthopaedic tumour resection surgery and the guidance of minimally invasive interventions.

7.2.2 Materials and Methods

Image overlay projection

The Image overlay projection device incorporates miniature RGB laser technology (PicoP Microvision, US) that produces in focus images from any projection distance. The device pose is tracked by a navigation system via passive tracking spheres attached to a marker reference on the device housing (Figure 71). The marker shield is suitable for sterilization in standard hospital reprocessing and can be attached externally to a transparent surgical sterilized drape that covers the entire device and part of the attached cable, making the device suitable for use in sterile clinical environments. The device was designed to be integrated into existing surgical planning and navigation systems in order to utilize the systems' inherent registration and tracking capabilities. The projector has an update rate of 60Hz and is thus limited solely by the navigation/planning software image update rate and sensor update rate (typically 20Hz).

Figure 71: Image overlay projection device employed for AR visualisation.

By defining a virtual camera in the virtual scene of the surgical planning or navigation software tool, at the pose of the centre of projection, data for projection can be obtained from the view point of the projector (see Figure 72). Thereafter, geometrically correct images can be projected onto the patient from any position within the navigation camera workspace. The pose of the centre of projection is calibrated using camera calibration techniques. Projection of the device was described by a reverse pin hole camera model and thus, could be solved for the transformation relating an image pixel to a 3D real world point of projection using Zhang's calibration method [115]. The calibrated transformation defining the static transformation from the projection centre to the tracked marker shield of the device, ${}^{IOD}T_{projector}$, could thereafter be determined. The pose of the projection centre can be calculated in real time using equation (17) and is used to define the virtual camera perspective within the virtual scene.

$$ {}^{Sensor}T_{Projecor} = {}^{Sensor}T_{IOD} \cdot {}^{IOD}T_{Projector} \tag{17} $$

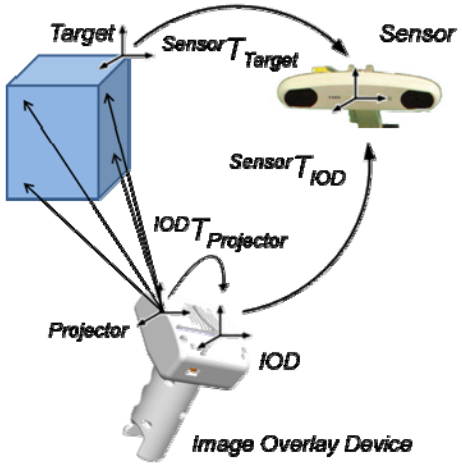

Figure 72: Image overlay system transformation diagram.

Illumination of the device is sufficient to produce images with easily identifiable structures in projected images with size up to 200 × 350 mm in ambient light. As the image overlay device relies on the registration and tracking capabilities of the navigation system into which it is integrated, the accuracy of the device also depends on the accuracy of the navigation system. In a previous study [101] the image overlay device was found to have a mean projection accuracy of 1.3 mm when integrated into a Liver Surgical Navigation System [97] with navigation camera accuracy of approximately 0.3 mm. Tests were performed on both planar and 3D rigid models. The device is lightweight and portable and has a complete set up time of less than 2 minutes. Details of the design, calibration and surface projection accuracy evaluation of the image overlay device is presented in [101]. The image overlay device can be integrated into existing surgical navigation/planning applications via a software module that handles device tracking, image rendering from the perspective of the projector and the output of images for display. To enable AR viewing of existing navigation data, the surgical navigation software must incorporate a 3D virtual scene incorporating anatomical data or guidance data for display. In addition, and as in conventional image guided surgery, a method of registering the 3D scene to the real patient must be available.

Surgical Guidance System Description

During this study, two surgical guidance systems representative of the systems currently in widespread use were augmented to enable AR viewing. Both systems comprise (see Figure 73 for an example) a navigation computer unit, an infrared-based optical passive tracking system (Vicra, NDI, CA) and touch screen/s for user interaction and visual display. The optical cameras track known configurations of retro-reflective marker spheres. Tools (i.e. ultrasound dissectors, microwave ablation

devices, biopsy needles etc) have unique sterilisable reference attachments which the system uses to determine the tools real-time pose. Visual feedback representing the relative pose of the patient anatomy, surgical plans, guidance information and tools are displayed on touch screen monitors. Both systems possess an additional DVI interface to which the image overlay device can be attached. The first system was designed for image guided liver surgery and allows anatomical models, tools and surgical plans to be displayed in a virtual 3D scene. The system incorporates capabilities for both pair point matching and ultrasound based patient-image registration. Patient tracking can be achieved via attachment of a trackable reference. The second system, designed specifically for percutaneous needle intervention guidance based on PET/CT, displays automatically rendered patient models from CT image data in a virtual scene along with co-registered PET images of target lesions. Real time guidance of a needle to target along a preoperatively defined trajectory is displayed in the form a cross hair target and depth bar adjacent to the image data. The system incorporates capabilities for both pair point matching and single marker based patient-image registration. Patient tracking can be achieved via single marker tracking or attachment of a trackable reference.

In this study, the first mentioned system was used in the feasibility evaluation of the first three application scenarios in which 3D anatomical models and various surgical planning data was displayed. The later system was used in the feasibility evaluation of minimally invasive intervention AR surface guidance. The systems are described in more detail in [97] and in the section 5.1 respectively.

Figure 73: Stereotactic instrument guidance system with integrated IOD employed within this study.

Clinical application

The feasibility and usefulness of the image overlay projector was evaluated in four different clinical scenarios within a laboratory setup. Integrated into a liver navigation system, the device was used to display anatomical structures such as blood vessels and tumours in addition to resection planes onto patient specific models and pig liver tissue. In a CMF application the device was used to display 3D anatomical models for the planning of mandibular tumour resection surgery. In a navigated orthopaedic surgery application, the device was used to project tumour locations and optimal bone resection margins onto patient specific tibia models. Finally, the device was tested in simulated navigation of a biopsy needle to a target tumour by projecting the target entry point, needle alignment and needle depth directly onto patient skin. Methodology for the generation of image overlay projection in each application is presented below.

Navigated open liver surgery: The navigation system for open liver surgery described in [97] was augmented to incorporate the image overlay projection device described above. Surface models of a liver and its internal vessels and tumours were pre-segmented from CT by Mevis Distant Services (MeVis Medical Solutions AG, Bremen, Germany) via the process described in [116], see Figure 74a.

The liver model construction process was completed as per non AR navigated liver surgery and the models were added to the surgical navigation systems virtual 3D scene as normal. A patient specific rigid liver model and porcine liver tissue were used as projection surfaces. The rigid model was developed via 3D printing rapid prototyping (Spectrum Z$_{TM}$ 510 printer by ZCorporation). The first was used to validate the projection on the corresponding 3D liver structure whilst the later was used in the determination of the feasibility of projecting the liver models onto real liver tissue. The liver models were registered to the virtual models with the locally rigid pair point matching technique already implemented in the surgical navigation system.

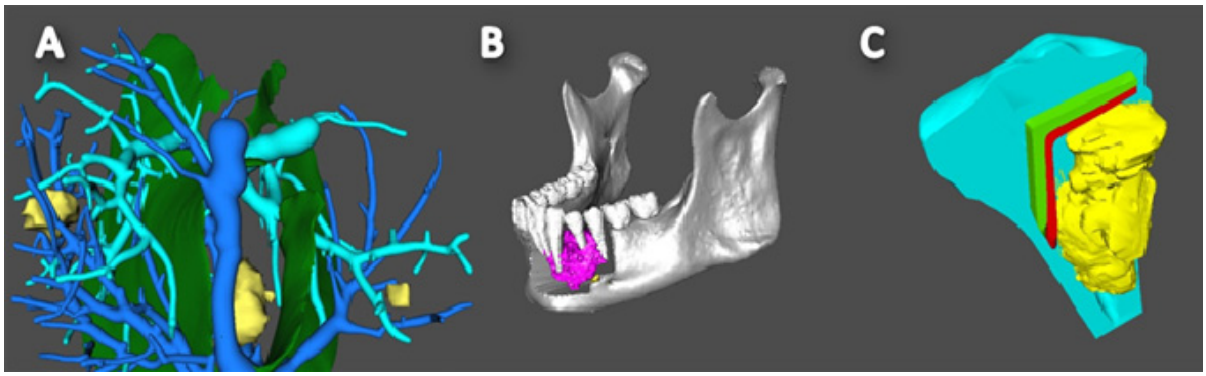

Figure 74: Unmodified original 3D anatomical models from navigation/planning software employed in previous surgical procedures. a) Liver resection plan. b) CMF osteotomy plan. c) Proximal tibia resection plan.

CMF preoperative planning and navigated surgery: The proposed visualisation approach was applied to the planning of a mandibular resection for tumour removal. 3D models of the mandible, target tumour and the mandibular branch of the facial nerve were segmented from NewTom CBCT images using ITK-SNAP as described in [117], see Figure 74b. For this study, structures were highlighted through increased colour intensity and the transparency level of the mandible was increased to enable viewing of critical underlying structures in a single view. The right side of the 3D model was removed to prevent overlay interference during projection on the left side of the jaw. Possible resection areas were defined according to tumour position, size and proximity to critical structures. The 3D model with planned resection areas were loaded into the virtual scene of the liver surgical navigation system. A human subject was placed in a sitting position and registered to the virtual data using the navigation systems locally rigid pair point matching capabilities. Conventionally, thereafter, movement of the patient is tracked via a tracking reference, for example applied to the head and opposite side of the jaw. The 3D anatomical models incorporating various resection options, the tumour tissue and critical structures were projected directly onto the skin of the patient's left jaw.

Navigated orthopaedic tumour resection: Orthopaedic oncological surgical navigation data including 3D surface models of the proximal tibia, tumour and safe resection margins were projected on a patient specific rigid 3D phantom developed via 3D printing rapid prototyping (Spectrum Z$_{TM}$ 510 printer by ZCorporation). The 3D anatomical models and plan, used previously during image guided cadaver limb salvage surgery [118], were semi-automatically segmented from CT images using Amira® (Visage Imaging, Inc., San Diego, CA,USA), and stored in the form of surface point models and surface meshes, see Figure 74c. 3D resection planes were added to the anatomical model by the operating surgeon also using Amira®. No modification to the original navigation data was made for use in this study. The 3D model with planned safe resection planes were loaded into the virtual scene of the liver surgical navigation system. A 3D rigid phantom of the tibia model was developed via 3D printing rapid prototyping (Spectrum Z$_{TM}$ 510 printer by ZCorporation). The model was registered to its virtual model using the navigation system's locally rigid pair point matching capabilities.

Navigated percutaneous needle: A navigation system developed to assist percutaneous interventions based on PET/CT images was augmented with the described projection capability, and the feasibility of displaying the necessary guidance information on the patient skin was assessed. For this

study, patient CT and PET data was used to simulate a navigated biopsy procedure. A single tumour was isolated in the PET dataset and defined as the target for this procedure. 3D model of the patient surface was automatically generated by the navigation system using contour filters from the Visualization Toolkit (VTK) library. A tracking reference was attached to a band placed around the patient's upper torso to allow for patient movement tracking. Patient-to-image registration is usually performed automatically by matching the marker spheres from the reference in both spaces, image and tracking. However, in this study, landmark based registration was used. Prior to the simulated procedure, the user defined the intended needle trajectory by selecting the location of the target and the needle entry point in the navigation system's CT viewers. Guidance information for this application is usually visualised within a targeting viewer that displays the needle tip and shaft positions in addition to a depth bar indicting the distance from the tool tip to the target, see Figure 75. For this study, the visual information to guide the needle to the target according to the planned trajectory was defined on a plane normal to the patient's skin, centred on the preoperatively planed entry point. The main cross-hair target thus remained static on the patient at the entry sight whilst the needle pose and depth guidance were updated to the current needle position at a rate of 20Hz. The correct needle alignment is accomplished by bringing the tip and the shaft to the centre of the cross hair target. The target is reached when the distance bar reaches zero. In the projected image, PET images were displayed under the cross hair guide to allow visualisation of the target structure as the needle approached. The surgery was emulated in a laboratory setup using a retractable needle to avoid piercing the skin of the human subject.

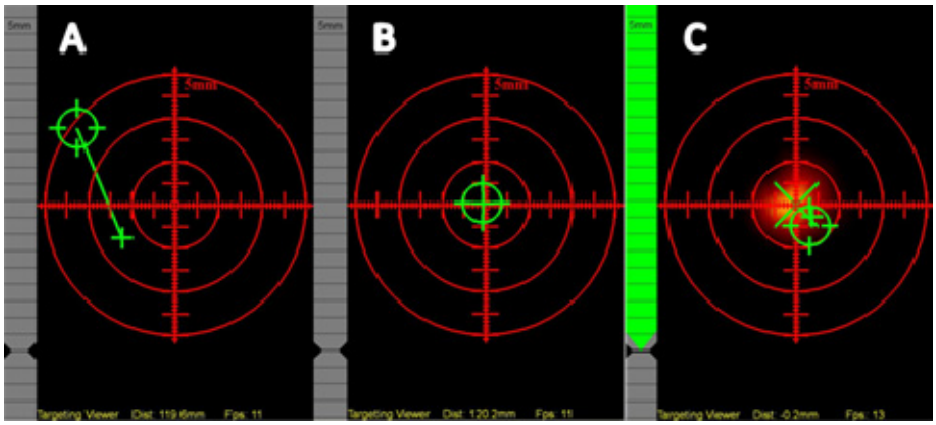

Figure 75: Unmodified original biopsy guidance displays from navigation software with patient PET data. a) Biopsy needle tip entry site alignment. b) biopsy needle shaft alignment. c) biopsy needle depth guidance with visible target lesion (PET data).

Feasibility evaluation: The feasibility of employing the proposed AR visualisation approach in each clinical application was qualitatively evaluated via the following criteria:

1. Integrability of the device into existing surgical image guidance systems
2. Visibility of the projected structures
3. Obtrusiveness of the device to the surgical scene
4. Workspace of the device due to image size and visibility to the optical tracking camera
5. Usability of the device within the surgical scene

The criteria were assessed during the projection of the anatomical and guidance data summarised in Table 7. The study group for each clinical scenario consisted of three subjects. Two additional observes familiar with the AR approach were present to evaluate the simulated scene. All subjects were familiar with image guidance surgery and optical tracking systems. At least one subject in each group was involved in the development of non AR image guidance surgical systems for the corresponding clinical application and at least one subject was unfamiliar with the AR approach being evaluated. Prior to each study, virtual models were loaded into the navigation system, surgical planning was

completed and the model or patient was registered to the image data. Thereafter, each simulated projection study followed the below described protocol.

1. The optical tracking system was placed to one side of the patient or phantom model and the three subjects stood in positions of their choice on the opposite side.
2. One subject was asked to display the image data on the projection surface whilst remaining subjects identified the structures contained within the projected model.
3. Following structure identification, one subject was instructed to hold the image overlay device in one hand and simultaneously perform simple tasks such as positioning a biopsy needle to its entry alignment or pointing out structures with a scalpel or pointer.
4. Thereafter, one subject was instructed to display the image overlay whilst the two other subjects identified structures with pointers or scalpels or performed a simulated biopsy needle placement using the projected data.

Tasks were repeated until all three subjects with differing skills had operated the image overlay device.

Table 7: Data types visualized using AR image overlay projection.

Application	Anatomy	Plan	Maximum projection size (mm)
Liver surgery	Vessels, Lesions	Resection planes	200 x 130
CMF surgery	Tumour, Facial nerve, Mandible	Resection area	110 x 80
Orthopaedic Surgery	Tumour	Safe resection margins	90 x 70
Biopsy	Suspicious lesion (PET)	Entry point crosshair Alignment guidance Depth bar Depth in text	60 x 80

7.2.3 Results

A software module for handling the tracking of the image overlay device and the generation of images at the pose of the projector was successfully integrated into both navigation systems described above. Minimal modifications were required to existing surgical navigation data to enable their visible projection onto the patient or phantom.

Size of the displayed structures, colour, contrast and illumination were all found to be sufficient to enable individual structures to be identified by all subjects and evaluators in ambient light. The maximum image size of projection for each application, as displayed in Table 7, was within the limit of the device and thus the entire model could be viewed in ambient light in a single projection.

The available workspace was sufficient to allow two additional subjects to perform various tasks without being obstructed by the device and without the subjects obstructing the line of sight between the device and the tracking camera. The device was most commonly held approximately 20 to 30 cm from the patient approximately perpendicular to the projection surface. Due to its handheld, portable nature and small size, the device could be held in a non-intrusive position and could be easily moved to alternative positions when necessary to remain out of the workspace of the operating subjects. All subjects in all clinical cases were able to hold the device in one hand whilst simultaneously performing simple tasks with the other. Inexperienced subjects were immediately able to use the device in a useful manner. Initially, some operators of the device were more likely to move it quickly throughout the workspace, possibly due to curiosity. Such movements which cause the projected images to be more affected by lag were however, unnecessary and were no longer performed by operators after a learning period of less than one minute.

During the feasibility study the proposed approach allowed underlying anatomical structures and relative resection planes to be viewed in the same view as the patient. AR visualisation of anatomical models along with associated surgical plan data for liver surgery, CMF surgery and orthopaedic surgery, performed with the image overlay device are illustrated in Figure 76. The approach removed the

need for the user to mentally align the underlying structures with the real patient or to divert their view or attention away from the patient and thus allowed underlying structures to be identified and targeted intuitively and quickly.

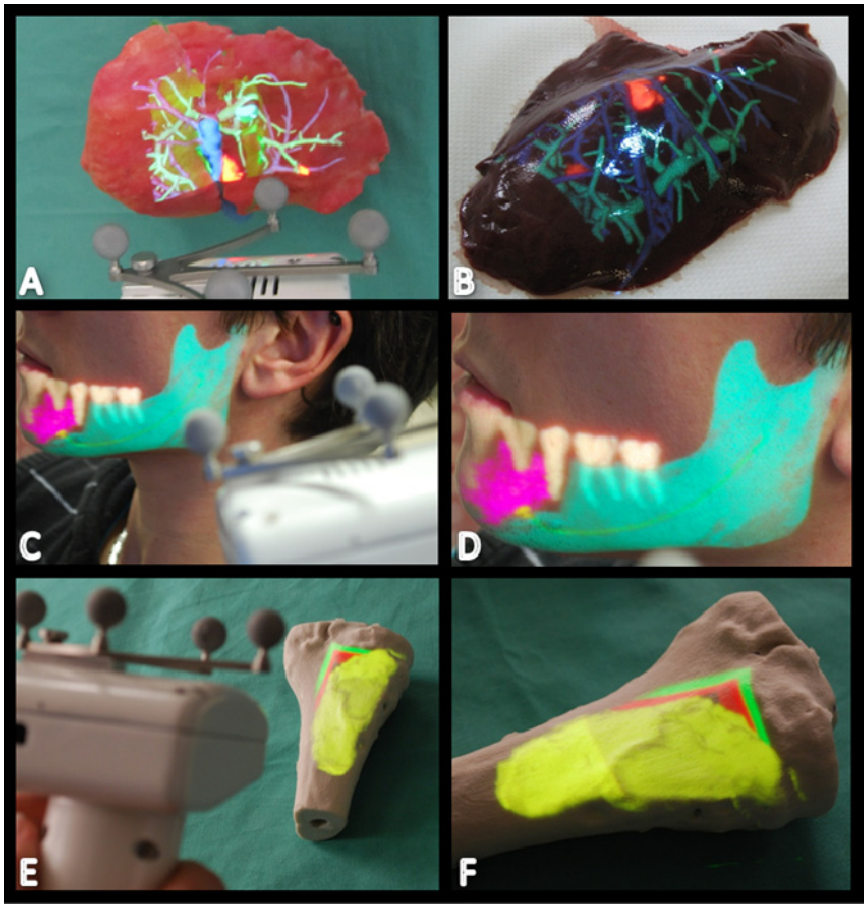

Figure 76: a) Image overlay AR for navigated liver surgery on a patient specific rigid model and b), pig liver tissue; c) and d) Image overlay AR for navigated CMF surgical planning; e) and f) Image overlay AR for navigated orthopaedic tumour resection.

In an open liver surgery, the location of the target tumour tissue could be visualized in relation to surrounding structures directly on the liver surface. Whilst all structures were visible and distinguishable, a certain amount of depth perception was lost in the AR projection and the location of structures was affected by parallax. In CMF surgery, preoperatively defined resection of the mandible could be visualized directly on the patient's jaw. Critical structures in close proximity to the resection area, such as the facial nerve, could be visualized and aided in the planning of a surgical approach. Due to the superficial position of the projected anatomical structures, the visualisation approach suffered minimally from loss of depth perception and parallax effect. In oncology orthopaedics, the image overlay provided an intuitive method of visualizing the position of the tumour with respect to the healthy anatomy along with resection safety margins. Locating resection planes on the bone could be achieved intuitively and quickly. Due to the rigidity of bone, the projected images remained immune from distortion that results from tissue deformation. Due to a loss of depth perception, 3D resection planes were however, more difficult to comprehend suggesting that 2D resection lines defined on the bone surface itself would be more effectively visualised in such an approach.

During a simulated navigated tumour biopsy procedure, needle position and orientation guidance targets were projected by the image overlay device directly onto the skin of the patient at the preoperatively defined entry point. Depth information feedback used to guide the needle to the tumour target was displayed adjacent to the guidance target. Text providing precise distance in mm to the target was displayed below the guidance target. As the simulated position of the needle reached the target, the PET image of the lesion could be viewed in the centre of the cross hair target. Images of the projected guidance are displayed in Figure 77. All information including written text could be easily identified

throughout the simulated procedure. Occasionally, projection was obstructed by the biopsy needle itself. Repositioning the projector easily corrected this problem. Displaying such information on the patient skin right at the point of intervention presented certain advantages. It not only facilitated the spatial interpretation required to orient the needle, but also allowed the physician to keep the patient within his field of attention while performing the virtual puncture.

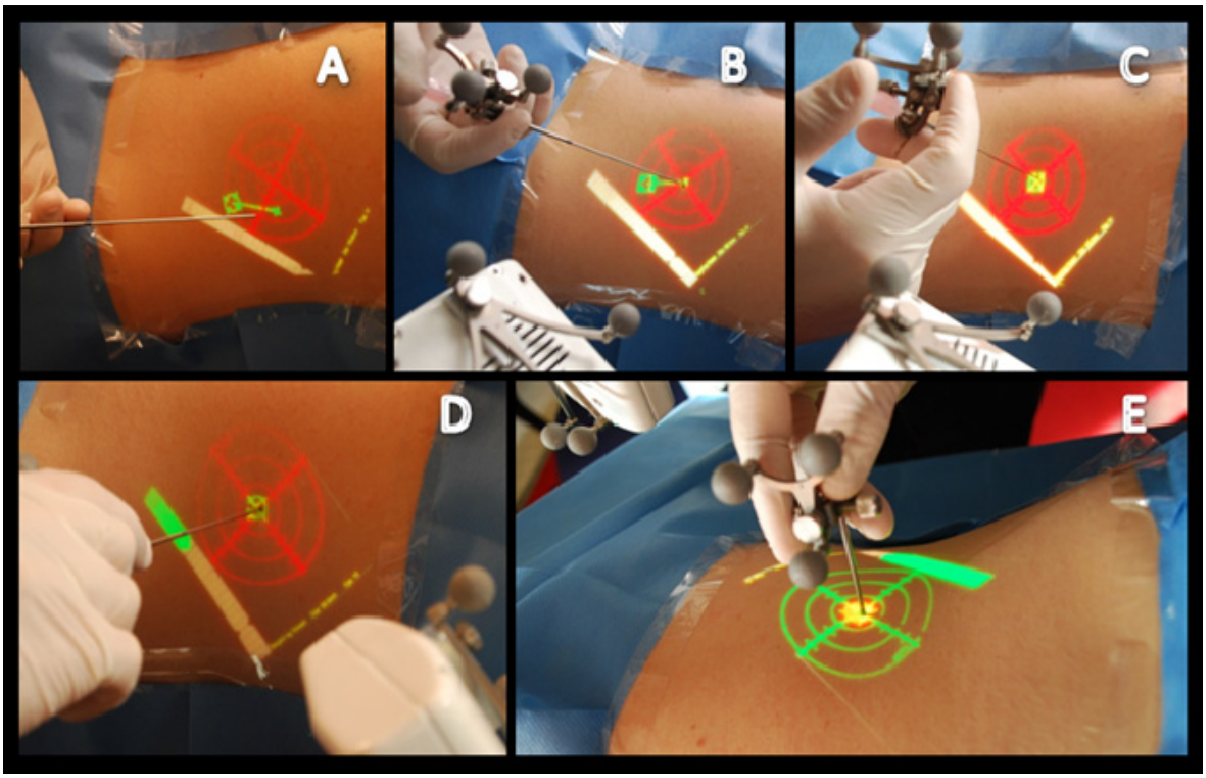

Figure 77: Image overlay projection of percutaneous needle guidance information throughout a simulated biopsy procedure. a) Tip alignment. b) Shaft alignment. c) Aligned needle at point of puncture. d) Depth guidance. e) Target visualisation.

7.2.4 Discussions and Conclusions

The purpose of this work was to investigate the feasibility of using a novel augmented reality approach for the visualisation of surgical navigation data as an improved alternative to monitor display.

Through the integration of the device and through the projection of a range of existing navigation data, we have demonstrated the versatility of the approach. From our experimental results we can state that the navigated image projection system can be easily integrated into existing surgical navigation systems and that the proposed visualisation method does not impose any timely or procedural overhead when compared to monitor displayed navigated procedures. The workspace of the approach was sufficient in all four cases to produce easily visible complete scenes on the respective anatomical phantom surface. Additionally, the portable handheld nature of the device allowed the user to maintain line of sight to the optical tracking camera whilst remaining unobtrusive to the surgical scene.

The user benefited from an image augmented view which eliminated the need for diversion of sight or attention during assessment and use of the additional visual information. We believe that such a direct visualisation is highly intuitive, optimizes the understanding of the spatial context in which a procedure is carried out and may result in reduced surgical time and increased interventional precision.

Our experiments have demonstrated that in a clinical context, virtually any 3D image can be back-projected to its anatomical origin or the skin above it using this approach. In addition to 3D anatomical models, raw image data such as CT, MRI, angiography or PET images of the critical and target anatomical structures could be displayed. Surgical planning data such as resection planes safety

margins, guidance targets, depth levels and even written text can also be displayed directly onto the surgical site.

Whilst the benefits of the image overlay for surgical data visualisation were evident, a number of deficiencies in the approach were also identified during this study. Firstly, when projecting onto soft tissue such as skin or the liver surface, deformations in the tissue at the sight of projection can result in distortion of the projected guidance image. In cases of surface guidance such as used in the simulated navigated biopsy, this deficiency can be easily overcome by repositioning guidance data away from the puncture sight after the entry sight has been located and the skin has been penetrated. However, when surgical guidance involves the display of underlying anatomical structures, deformations in the tissue cannot be so easily handled. Handling tissue deformation in this case requires surface tracking of the projection site and appropriate deformation to the projected images in order to maintain correct geometry. Reports from a number of research groups currently exploring soft tissue movement tracking, do however, indicate that higher accuracy solutions are likely to become available in the near future ([95, 96], and section 6.2).

For applications in which all data for visualisation is defined on the patient surface, such as the navigated biopsy, procedure accuracy is not affected by parallax error. All applications displaying structures that are positioned below the projection surface will however be affected by the pose of the viewer. Whilst the parallax error involved in this approach is less than in semi transparent displays, because the projected scene is viewed directly on the objects surface and not in a certain depth between the observer and the object itself, the effect is still evident when projecting deep lying structures. Previously reported methods of parallax correction have involved non-user friendly solutions that require head or eye tracking. Requiring the surgeon to wear heavy head gear and limiting their movement to within tracking sensor ranges has been poorly accepted and was thus not integrated into this approach. In future work we hope to implement a more simplistic and less obtrusive solution to overcome parallax error. Until such time, guiding surgeons to deep targets with surface defined projections like that displayed in Figure 77, provides a suitable alternative for procedures with high accuracy requirements and deeply targeted structures.

Finally, depth perception of displayed data continues to be a challenge in 2D projection. Depth information could be recovered in future applications by coding it into the models being projected as suggested for example by Hansen *et al.* [102].

In the near future, results of this study suggest that applications involving rigid structures and superficial structures are most suited to AR visualisation using the presented approach. In addition, deep lying structures can be most accurately and quickly target with AR guidance not by displaying the anatomical structure itself but by displaying entrance points, resections lines or real time guidance applications on the anatomical surface.

In conclusion, we have presented an alternative visualisation method for surgical navigation and planning data that overcomes many of the deficiencies of conventional displays and previously developed AR technologies. We believe that this work highlights the usefulness and feasibility of the approach in a range of surgical applications and thus presents an initial step towards a widely accepted alternative to monitor displays for the visualisation of surgical navigation data. It is predicted that future advancements in navigation technology, 3D data representation and miniature laser technology will see continued developments in the presented approach.

8 Conclusions

Brief: In this chapter, the overall achievements of this thesis are summarized and the final conclusions are presented. Finally, the limitations and open questions are presented in the Outlook section.

This thesis has presented a set of advanced and clinically applicable image guidance approaches to overcome the drawbacks associated with the currently used clinical solutions for percutaneous needle interventions. It commenced by an investigation into image guidance methods to support multimodal percutaneous needle interventions based on nuclear images. An image guidance system to aid multimodal interventions in stable regions of human anatomy (e.g. pelvis) has been developed. The system that enables punctures aiming targets located in soft tissue and bone was evaluated during swine cadavers experiments. Results showed that the achieved accuracy was sufficient for interventions based on PET/CT datasets. The number of necessary CT acquisitions have been reduced which consequently decreased the level of radiation exposure and the procedure time. During the experiments, the system showed to increase visual intuitiveness and to facilitate the intervention workflow. Trajectory planning could be performed out of the axial plane and effectively by using the proposed visualization resources. Patient preparation and planning were effectively separated from the sterile phases and the required interaction between the system and the physician was kept low. Additionally, a registration pipeline for correcting target displacement during bone interventions has been proposed and evaluated. Results have shown the feasibility of correcting target displacement during PET/CT intervention aiming lesions located in bones. The registration pipeline enabled reliable target visualization during bone interventions.

In a second step, an image guidance approach to support interventions in deformable regions of human anatomy (e.g. chest and abdomen) has been proposed. The approach is based on market available optical tracking systems and retro-reflective single marker spheres attached to the patient's skin. Firstly, a method for automatic patient-to-image registration was proposed and evaluated. Results have shown that patient-to-image registration can be performed without physician interaction. Such a feature increases the level of clinical acceptance because the standard clinical workflow is unaltered. Additionally, a method for patient referencing under deformation was also proposed and evaluated. Results have shown that soft tissue regions of the patient's anatomy can be tracked in real time while facing different intra-interventional conditions including deformation and occlusions. Results have also shown that identification of deformation is possible and that the information provided can be used for gating procedures. Viewers displaying the current amount of deformation at the region of the intervention enable physicians to give voice commands to patients in order to obtain an optimal state of breath hold to perform the puncture. With the presented approach, non rigid parts of the anatomy can be punctured without increasing the complexity of the intervention.

In a third step, an augmented reality projection approach was proposed in order to eliminate the need for sight diversion during image guided interventions. Using a portable image overlay device proposed in a previous report [101], needle guidance information could be displayed directly in the view of the patient. Results have shown that guidance information is sufficiently visible at real time on patient's skin and unlike other proposed augmented reality approaches, no obtrusive hardware was required. Clinical integration was facilitated by proposing a plug-and-play device that does not need to be calibrated before each intervention. Such a direct visualisation is highly intuitive because it eliminates the need for metal registration between the real and the virtual scene displayed on monitors.

In conclusion, the approaches presented in this thesis were able to address all the clinical issues raised in the introduction, while coping with the technical challenges associated with image guidance. The set of methods presented have been integrated into one image guidance system to provide a single and improved solution for percutaneous needle interventions. With the outcome of this thesis, it is

expected that future image guided intervention can be performed: with a reduced radiation exposure and intervention time, with a flexible trajectory planning along the image volume, with an intuitive guidance within a registered intervention scenario, and with correctly aligned PET/CT. Such achievements are not only beneficial for physicians and hospitals, but also for the patient as access to target will be faster and a more comfortable procedure will be provided. One of the outcomes of this project was a image guidance system integrating the approaches presented in this thesis. The system is going to be used by clinical partners to run a complete clinical study.

8.1 Outlook

Although the approaches presented in this thesis provide an improved solution compared to currently used methods, they have restrictions that have not been addressed and deserve future attention. The first limitation is caused by needle bending that is associated with the type of instrument tracking used. In this work, stiff needles have been used to avoid bending, however in the case of fine needles, bending can be significant. Methods modelling or reducing such effect have been summarized by Abolhassani *et al.* [65]. The second limitation is related to the target displacement correction that has only been addressed in bone. Bones are rigid structures that are very well visible in CT images providing sufficient information to register and correct such displacements. Soft tissue however, might not present sufficient contrast to ensure a good registration. Moreover, soft tissue is a non rigid structure which cannot be registered with rigid registration algorithms. Therefore, investigation of advanced non rigid registration methods is required to address target displacements in soft tissue locations. An additional insight obtained through this work concerns to the patient-to-image registration in percutaneous nephrolithotomy interventions. The long time frame between imaging and intervention, the different imaging and intervention locations, as well as the additional filling of the collecting system in the kidney can introduce significant deformation to the patient. Such cases require investigation of additional image registration techniques (e.g. intra-interventional ultrasound to pre-interventional CT). Further improvements should also include parallax correction to the projected image of the augmented reality approach. Although parallax is not a major issue when displaying surface information such as the crosshair of the targeting viewer, it can still distort the viewer when projecting onto highly curved surfaces. Moreover, it hinders the display of structures located deep in the anatomy. Previous research has tried to use head and eye tracking devices to overcome such problems. However, such an approach requires poorly acceptable equipment to be worn. With the portable solution presented in this thesis, parallax could be corrected by creating an optimal point of view to the user. Finally, clinical trials with the complete approach are still desired.

The proposed image guidance approaches have focused attentions on percutaneous needle interventions. However, the methods presented here are not fixed to one solution and therefore could be expanded to other domains. The non-rigid anatomy tracking for example, can be used for organ tracking in open surgery. Such approach is currently being investigated in the hope that it could provide reference for the liver as well as deformation detection during stereotactic instrument guidance for open liver surgery.

Bibliography

[1] E. Cardinal, R. K. Chhem, and C. G. Beauregard, "Ultrasound-guided interventional procedures in the musculoskeletal system," *Radiologic Clinics of North America*, vol. 36, no. 3, pp. 597-604, May 1998.
[2] G. Poggi et al., "Percutaneous ultrasound-guided radiofrequency thermal ablation of malignant osteolyses," *Anticancer Research*, vol. 23, no. 6, pp. 4977-4983, Dec. 2003.
[3] S. Möller, R. Kothe, L. Wiesner, M. Werner, W. Rüther, and G. Delling, "Fluoroscopy-guided transpedicular trocar biopsy of the spine - results, review, and technical notes," *Acta Orthopaedica Belgica*, vol. 67, no. 5, pp. 488-499, Dec. 2001.
[4] B. Ghelman, "Biopsies of the musculoskeletal system," *Radiologic Clinics of North America*, vol. 36, no. 3, pp. 567-580, May 1998.
[5] A. Hau et al., "Accuracy of CT-guided biopsies in 359 patients with musculoskeletal lesions," *Skeletal Radiology*, vol. 31, no. 6, pp. 349-353, Jun. 2002.
[6] J.-M. Neuerburg, G. Adam, and D. Hunter, "New Trends in Musculoskeletal Interventional Radiology: Percutaneous, MR_Guided Skeletal Biopsy," *Seminars in Musculoskeletal Radiology*, vol. 1, no. 2, pp. 339-348, 1997.
[7] K. Huch, G. Röderer, B. Ulmar, and H. Reichel, "CT-guided interventions in orthopedics," *Archives of Orthopaedic and Trauma Surgery*, vol. 127, no. 8, pp. 677-683, Oct. 2007.
[8] J.-C. Liu et al., "Sonographically guided core needle biopsy of soft tissue neoplasms," *Journal of Clinical Ultrasound: JCU*, vol. 32, no. 6, pp. 294-298, Aug. 2004.
[9] E. Lis et al., "Percutaneous CT-Guided Biopsy of Osseous Lesion of the Spine in Patients with Known or Suspected Malignancy," *AJNR Am J Neuroradiol*, vol. 25, no. 9, pp. 1583-1588, Oct. 2004.
[10] E. Salomonowitz, "MR imaging-guided biopsy and therapeutic intervention in a closed-configuration magnet: single-center series of 361 punctures," *AJR. American Journal of Roentgenology*, vol. 177, no. 1, pp. 159-163, Jul. 2001.
[11] E. Piperkova et al., "Impact of PET/CT in comparison with same day contrast enhanced CT in breast cancer management," *Clinical Nuclear Medicine*, vol. 32, no. 6, pp. 429-434, Jun. 2007.
[12] B. E. Hillner et al., "Impact of Positron Emission Tomography/Computed Tomography and Positron Emission Tomography (PET) Alone on Expected Management of Patients With Cancer: Initial Results From the National Oncologic PET Registry," *Journal of Clinical Oncology*, vol. 26, no. 13, pp. 2155-2161, May 2008.
[13] B. Klaeser, O. Wiederkehr, D. Koeberle, A. Mueller, B. Bubeck, and B. Thuerlimann, "Therapeutic impact of 2-[fluorine-18]fluoro-2-deoxy-D-glucose positron emission tomography in the pre- and postoperative staging of patients with clinically intermediate or high-risk breast cancer," *Annals of Oncology*, vol. 18, no. 8, pp. 1329 -1334, 2007.
[14] B. Klaeser, M. Mueller, R. Schmid, C. Guevara, T. Krause, and J. Wiskirchen, "PET-CT-guided interventions in the management of FDG-positive lesions in patients suffering from solid malignancies: initial experiences," *European Radiology*, vol. 19, no. 7, pp. 1780-1785, Jul. 2009.
[15] G. B. Saha, *Basics of PET Imaging: Physics, Chemistry, and Regulations*, 1st ed. Springer, 2004.
[16] B. Klaeser et al., "PET/CT-guided biopsies of metabolically active bone lesions: applications and clinical impact," *European Journal of Nuclear Medicine and Molecular Imaging*, vol. 37, no. 11, pp. 2027-2036, Nov. 2010.
[17] A. Compston, "The structure and functions of the cerebellum examined by a new method. By Sir Victor Horsley, FRS, FRCS and R.H. Clarke, MA, MB. Brain 1908: 31; 45-124.," *Brain*, vol. 130, no. 6, pp. 1449-1452, Jun. 2007.

[18] D. W. Roberts, J. W. Strohbehn, J. F. Hatch, W. Murray, and H. Kettenberger, "A frameless stereotaxic integration of computerized tomographic imaging and the operating microscope," *Journal of Neurosurgery*, vol. 65, no. 4, pp. 545-549, Oct. 1986.
[19] E. Watanabe, T. Watanabe, S. Manaka, Y. Mayanagi, and K. Takakura, "Three-dimensional digitizer (neuronavigator): new equipment for computed tomography-guided stereotaxic surgery," *Surgical Neurology*, vol. 27, no. 6, pp. 543-547, Jun. 1987.
[20] Y. Kosugi et al., "An articulated neurosurgical navigation system using MRI and CT images," *IEEE Transactions on Bio-Medical Engineering*, vol. 35, no. 2, pp. 147-152, Feb. 1988.
[21] E. M. Friets, J. W. Strohbehn, J. F. Hatch, and D. W. Roberts, "A frameless stereotaxic operating microscope for neurosurgery," *IEEE Transactions on Biomedical Engineering*, vol. 36, no. 6, pp. 608-617, Jun. 1989.
[22] R. L. Galloway Jr, "The process and development of image-guided procedures," *Annual Review of Biomedical Engineering*, vol. 3, pp. 83-108, 2001.
[23] L. P. Nolte and R. Ganz, *Computer Assisted Orthopedic Surgery*. Hogrefe-Verlag, 1999.
[24] R. H. Taylor, S. Lavealle, G. C. Burdea, and R. Mosges, Eds., *Computer-Integrated Surgery: Technology and Clinical Applications*, 1st ed. MIT Press, 1995.
[25] M. Caversaccio, K. Lädrach, R. Bächler, G. Schroth, L. P. Nolte, and R. Häusler, "[Computer-assisted surgical navigation with a dynamic mobile framework for the nasal fossae, sinuses and base of the skull]," *Annales D'oto-Laryngologie Et De Chirurgie Cervico Faciale: Bulletin De La Société D'oto-Laryngologie Des Hôpitaux De Paris*, vol. 115, no. 5, pp. 253-258, Nov. 1998.
[26] M. Caversaccio et al., "[Surgery of the skull base and paranasal sinuses assisted by a computerized navigation system without external orientation support]," *Acta Otorrinolaringológica Española*, vol. 50, no. 5, pp. 392-397, Jul. 1999.
[27] G. Allen, Galloway Jr, R. Maciunas, C. Edwards II, and M. Zink, "Interactive image-guided surgical system for displaying images corresponding to the placement of a surgical tool or the like," U.S. Patent US52303381993.
[28] R. Bucholz, "Indicating the position of a surgical probe," U.S. Patent EP0997109B12003.
[29] T. M. Peters, "Image-guidance for surgical procedures," *Physics in Medicine and Biology*, vol. 51, no. 14, p. R505-R540, Jul. 2006.
[30] K. Cleary and T. M. Peters, "Image-guided interventions: technology review and clinical applications," *Annual Review of Biomedical Engineering*, vol. 12, pp. 119-142, Aug. 2010.
[31] J. V. Hajnal, D. L. G. Hill, and D. J. Hawkes, *Medical Image Registration*, 1st ed. CRC Press, 2001.
[32] C. V. Tiesenhausen, S. Weber, K.-T. Hoffmann, and T. C. Lueth, "A new mobile and light-weight navigation system for interventional radiology," *International Congress Series*, vol. 1281, pp. 412-417, May 2005.
[33] V. Watson, N. Glossop, A. Kim, D. Lindisch, H. Zhang, and K. Cleary, "Image-Guided Percutaneous Vertebroplasty using Electromagnetic Tracking," in *5th Annual Meeting of CAOS-International Proceedings*, Helsinki, Finland, 2005, pp. 492-495.
[34] S. Nicolau, X. Pennec, L. Soler, and N. Ayache, "An Accuracy Certified Augmented Reality System for Therapy Guidance," *In Proc. of the 8th European Conference on Computer Vision (ECCV 04), Part III*, vol. 3023, pp. 79-91, 2004.
[35] S. Nicolau, J. Schmid, X. Pennec, L. Soler, and N. Ayache, "An Augmented Reality & Virtuality Interface for a Puncture Guidance System: Design and Validation on an Abdominal Phantom," in *Proc of the Second Int. Workshop on Medical Imaging and Augmented Reality MIAR 2004*, Beijing, China, 2004, vol. 3150, pp. 302-310.

[36] S. A. Nicolau, X. Pennec, L. Soler, and N. Ayache, "A complete augmented reality guidance system for liver punctures: first clinical evaluation," *Medical Image Computing and Computer-Assisted Intervention (MICCAI)*, vol. 8, no. 1, pp. 539-47, 2005.
[37] S. Nicolau, A. Garcia, X. Pennec, L. Soler, and N. Ayache, "An augmented reality system to guide radio-frequency tumor ablation," *Computer Animation and Virtual World (previously the Journal of Visualization & Computer Animation)*, vol. 16, no. 1, pp. 1-10, 2005.
[38] M. F. Khan et al., "Accuracy of biopsy needle navigation using the Medarpa system - computed tomography reality superimposed on the site of intervention," *European Radiology*, vol. 15, no. 11, pp. 2366-2374, Mar. 2005.
[39] M. F. Khan et al., "Navigation-based needle puncture of a cadaver using a hybrid tracking navigational system," 2006.
[40] L. Maier-Hein et al., "Precision targeting of liver lesions with a needle-based soft tissue navigation system," *In Proc. Medical Image Computing and Computer Assisted Intervention (MICCAI)*, vol. 10, no. 2, pp. 42-49, 2007.
[41] B. Meyer et al., "Electromagnetic field-based navigation for percutaneous punctures on C-arm CT: experimental evaluation and clinical application," *European Society of Radiology 2008*, Jun. 2008.
[42] J. Krücker et al., "Electromagnetic Tracking for Thermal Ablation and Biopsy Guidance: Clinical Evaluation of Spatial Accuracy," *Journal of vascular and interventional radiology : JVIR*, vol. 18, no. 9, pp. 1141-1150, Sep. 2007.
[43] M. Militz, S. Hungerer, and A. Haug, "Pet-Ct-Fluoro-Matching On long Bones? – First Experiences," in *8th CAOS-International Proceedings*, 2008, pp. 53-54.
[44] E. B. Levy, J. Tang, D. Lindisch, N. Glossop, F. Banovac, and K. Cleary, "Implementation of an electromagnetic tracking system for accurate intrahepatic puncture needle guidance: accuracy results in an in vitro model," *Academic Radiology*, vol. 14, no. 3, pp. 344-354, Mar. 2007.
[45] B. J. Wood et al., "Navigation with electromagnetic tracking for interventional radiology procedures: a feasibility study," *Journal of Vascular and Interventional Radiology: JVIR*, vol. 16, no. 4, pp. 493-505, Apr. 2005.
[46] A. M. Venkatesan et al., "Real-time FDG PET Guidance during Biopsies and Radiofrequency Ablation Using Multimodality Fusion with Electromagnetic Navigation," *Radiology*, Jul. 2011.
[47] J. Krücker et al., "Clinical Utility of Real-time Fusion Guidance for Biopsy and Ablation," *Journal of Vascular and Interventional Radiology*, vol. 22, no. 4, pp. 515-524, Apr. 2011.
[48] B. J. Wood et al., "Navigation Systems for Ablation," *Journal of vascular and interventional radiology : JVIR*, vol. 21, no. 8, p. S257-S263, Aug. 2010.
[49] A. S. Carney, N. Patel, D. L. Baldwin, H. B. Coakham, and D. R. Sandeman, "Intraoperative image guidance in otolaryngology - the use of the ISG viewing wand," *The Journal of Laryngology and Otology*, vol. 110, no. 4, pp. 322-327, Apr. 1996.
[50] H. F. Reinhardt, G. A. Horstmann, and O. Gratzl, "Sonic stereometry in microsurgical procedures for deep-seated brain tumors and vascular malformations," *Neurosurgery*, vol. 32, no. 1, pp. 51-57; discussion 57, Jan. 1993.
[51] N. D. Glossop, "Advantages of optical compared with electromagnetic tracking," *The Journal of Bone and Joint Surgery. American Volume*, vol. 91 Suppl 1, pp. 23-28, Feb. 2009.
[52] S. A. Nicolau et al., "An augmented reality system for liver thermal ablation: Design and evaluation on clinical cases," *Medical Image Analysis*, vol. 13, no. 3, pp. 494-506, Jun. 2009.

[53] S. Nicolau, X. Pennec, L. Soler, and N. Ayache, "Clinical Evaluation of a Respiratory Gated Guidance System for Liver Punctures," in *Medical Image Computing and Computer-Assisted Intervention – MICCAI 2007*, 2007, pp. 77-85.
[54] L. Maier-Hein et al., "In-Vivo Targeting of Liver Lesions with a Navigation System Based on Fiducial Needles," in *Bildverarbeitung für die Medizin 2008*, 2008, pp. 227-231.
[55] L. Maier-Hein et al., "Respiratory motion compensation for CT-guided interventions in the liver," *Computer Aided Surgery*, vol. 13, no. 3, p. 125, 2008.
[56] L. Maier-Hein et al., "In vivo accuracy assessment of a needle-based navigation system for CT-guided radiofrequency ablation of the liver," *Medical Physics*, vol. 35, no. 12, p. 5385, 2008.
[57] L. Maier-Hein et al., "On combining internal and external fiducials for liver motion compensation," *Computer Aided Surgery: Official Journal of the International Society for Computer Aided Surgery*, vol. 13, no. 6, pp. 369-376, Nov. 2008.
[58] A. Leroy, P. Mozer, Y. Payan, F. Richard, E. Chartier-Kastler, and J. Troccaz, "Percutaneous renal puncture: requirements and preliminary results," *physics/0610209*, Oct. 2006.
[59] P. Mozer, A. Leroy, Y. Payan, J. Troccaz, E. Chartier-Kastler, and F. Richard, "Computer-assisted access to the kidney," *The International Journal of Medical Robotics and Computer Assisted Surgery*, vol. 1, no. 4, pp. 58-66, Dec. 2005.
[60] J. Hong and M. Hashizume, "An effective point-based registration tool for surgical navigation," *Surgical Endoscopy*, vol. 24, no. 4, pp. 944-948, Apr. 2010.
[61] J. BORGERT et al., "Respiratory motion compensation with tracked internal and external sensors during CT-guided procedures," *Computer aided surgery : official journal of the International Society for Computer Aided Surgery*, vol. 11, no. 3, pp. 119-125, May 2006.
[62] R. S. Santos et al., "Electromagnetic Navigation to Aid Radiofrequency Ablation and Biopsy of Lung Tumors," *The Annals of Thoracic Surgery*, vol. 89, no. 1, pp. 265-268, Jan. 2010.
[63] L. Appelbaum, J. Sosna, Y. Nissenbaum, A. Benshtein, and S. N. Goldberg, "Electromagnetic navigation system for CT-guided biopsy of small lesions," *AJR. American Journal of Roentgenology*, vol. 196, no. 5, pp. 1194-1200, May 2011.
[64] B. Schwald and H. Seibert, "Registration Tasks for a Hybrid Tracking System for Medical Augmented Reality," *IN JOURNAL OF WSCG (FEBRUARY 2004*, pp. 411-418, 2004.
[65] N. Abolhassani, R. Patel, and M. Moallem, "Needle insertion into soft tissue: A survey," *Medical Engineering & Physics*, vol. 29, no. 4, pp. 413-431, Jul. 2006.
[66] H. Kataoka, T. Washio, M. Audette, and K. Mizuhara, "A Model for Relations Between Needle Deflection, Force, and Thickness on Needle Penetration," in *Medical Image Computing and Computer-Assisted Intervention – MICCAI 2001*, vol. 2208, W. J. Niessen and M. A. Viergever, Eds. Berlin, Heidelberg: Springer Berlin Heidelberg, 2001, pp. 966-974.
[67] J. Memisevic, A. M. Okamura, and R. J. W. Iii, "Design Considerations for Robotic Needle Steering," no. April, pp. 3599-3605, 2005.
[68] A. M. Okamura, C. Simone, and M. D. O'Leary, "Force modeling for needle insertion into soft tissue," *IEEE Transactions on Biomedical Engineering*, vol. 51, no. 10, pp. 1707-1716, Oct. 2004.
[69] W. Birkfellner, F. Watzinger, F. Wanschitz, R. Ewers, and H. Bergmann, "Calibration of tracking systems in a surgical environment," *IEEE Transactions on Medical Imaging*, vol. 17, no. 5, pp. 737-742, Oct. 1998.
[70] M. Citak et al., "Percutaneous bone biopsy. A new application for 3D navigation: a pilot study," *Technology and Health Care: Official Journal of the European Society for Engineering and Medicine*, vol. 15, no. 4, pp. 231-236, 2007.

[71] M. Nagel, G. Schmidt, R. Petzold, and W. A. Kalender, "A navigation system for minimally invasive CT-guided interventions," *In Proc. Medical Image Computing and Computer Assisted Intervention (MICCAI)*, vol. 8, no. 2, pp. 33-40, 2005.
[72] H. G. Kenngott et al., "Development of a navigation system for minimally invasive esophagectomy," *Surgical Endoscopy*, vol. 22, no. 8, pp. 1858-1865, Aug. 2008.
[73] T. Wendler et al., "First demonstration of 3-D lymphatic mapping in breast cancer using freehand SPECT," *European Journal of Nuclear Medicine and Molecular Imaging*, vol. 37, no. 8, pp. 1452-1461, Aug. 2010.
[74] D. Cash et al., "Concepts and Preliminary Data Toward the Realization of Image-guided Liver Surgery," *Journal of Gastrointestinal Surgery*, vol. 11, no. 7, pp. 844-859, Jul. 2007.
[75] S. Mersmann et al., "Time-of-flight camera technique for augmented reality in computer-assisted interventions," 2011, p. 79642C-79642C-9.
[76] F. E. Veldpaus, H. J. Woltring, and L. J. Dortmans, "A least-squares algorithm for the equiform transformation from spatial marker co-ordinates," *Journal of Biomechanics*, vol. 21, no. 1, pp. 45-54, 1988.
[77] B. J. Wood et al., "Technologies for guidance of radiofrequency ablation in the multimodality interventional suite of the future," *Journal of Vascular and Interventional Radiology: JVIR*, vol. 18, no. 1 Pt 1, pp. 9-24, Jan. 2007.
[78] J. Ding et al., "Accuracy analysis of an image-guided system for vertebroplasty spinal therapy based on electromagnetic tracking of instruments," in *Medical Imaging 2008: Visualization, Image-guided Procedures, and Modeling*, San Diego, CA, USA, 2008, vol. 6918, p. 69181K-7.
[79] A. Seitel et al., "In-vitro evaluation of different visualization approaches for computer assisted targeting in soft tissue," *International Journal of Computer Assisted Radiology and Surgery*, vol. 2, pp. 188-190, Jun. 2007.
[80] J. M. Fitzpatrick, J. B. West, and C. R. Maurer, "Predicting error in rigid-body point-based registration," *IEEE Transactions on Medical Imaging*, vol. 17, no. 5, pp. 694-702, Oct. 1998.
[81] T. Oliveira-Santos et al., "Navigated Percutaneous Needle Intervention Based on PET/CT Images," in *Swiss Society for Biomedical Engineering (SSBE) Proceedings*, Bern, Switzerland, 2011, p. 51.
[82] L. Ibáñez, W. Schroeder, L. Ng, and J. Cates, "The ITK Software Guide," 2003.
[83] Mattes, D. R. Haynor, H. Vesselle, T. K. Lewellen, and W. Eubank, "Nonrigid multimodality image registration," vol. 4322, no. 1, pp. 1609-1620, 2001.
[84] D. Mattes, D. R. Haynor, H. Vesselle, T. K. Lewellen, and W. Eubank, "PET-CT image registration in the chest using free-form deformations," *Medical Imaging, IEEE Transactions on*, vol. 22, no. 1, pp. 120-128, 2003.
[85] S. Falahatkar, Z. Panahandeh, A. Sourati, M. Akbarpour, N. Khaki, and A. Allahkhah, "Percutaneous Nephrolithotomy Versus Open Surgery for Patients with Renal Staghorn Stones," *UroToday International Journal*, vol. 2, 2009.
[86] A. E. Krambeck, A. J. LeRoy, D. E. Patterson, and M. T. Gettman, "Long-term outcomes of percutaneous nephrolithotomy compared to shock wave lithotripsy and conservative management," *The Journal of Urology*, vol. 179, no. 6, pp. 2233-2237, Jun. 2008.
[87] A. J. LeRoy, H. J. Williams Jr, C. E. Bender, J. W. Segura, D. E. Patterson, and R. C. Benson, "Colon perforation following percutaneous nephrostomy and renal calculus removal," *Radiology*, vol. 155, no. 1, pp. 83-85, Apr. 1985.
[88] A. Khamene et al., "Characterization of Internal Organ Motion Using Skin Marker Positions," in *Medical Image Computing and Computer-Assisted Intervention – MICCAI 2004*, vol. 3217, C. Barillot, D. R. Haynor, and P. Hellier, Eds. Berlin, Heidelberg: Springer Berlin Heidelberg, 2004, pp. 526-533.

[89] J. Illingworth and J. Kittler, "A survey of the hough transform," *Computer Vision, Graphics, and Image Processing*, vol. 44, pp. 87-116, Oct. 1988.
[90] D. H. Ballard, "Generalizing the Hough transform to detect arbitrary shapes," *Pattern Recognition*, vol. 13, no. 2, pp. 111-122, 1981.
[91] M. Smereka and I. Dulęba, "Circular Object Detection Using a Modified Hough Transform," *International Journal of Applied Mathematics and Computer Science*, vol. 18, pp. 85-91, Mar. 2008.
[92] Z. Yaniv, E. Wilson, D. Lindisch, and K. Cleary, "Electromagnetic tracking in the clinical environment," *Medical Physics*, vol. 36, no. 3, pp. 876-892, Mar. 2009.
[93] M. Vetter, "Navigation aids and real-time deformation modeling for open liver surgery," 2003, vol. 5029, pp. 58-68.
[94] L. Maier-Hein, D. Maleike, J. Neuhaus, A. Franz, I. Wolf, and H.-P. Meinzer, "Soft tissue navigation using needle-shaped markers: Evaluation of navigation aid tracking accuracy and CT registration," 2007, vol. 6509, pp. 650926-650926-12.
[95] D. M. Cash, M. I. Miga, T. K. Sinha, R. L. Galloway, and W. C. Chapman, "Compensating for intraoperative soft-tissue deformations using incomplete surface data and finite elements," *IEEE Transactions on Medical Imaging*, vol. 24, no. 11, pp. 1479-1491, Nov. 2005.
[96] M. Markert, A. Koschany, and T. Lueth, "Tracking of the liver for navigation in open surgery," *International Journal of Computer Assisted Radiology and Surgery*, vol. 5, no. 3, pp. 229-235, Aug. 2009.
[97] M. Peterhans et al., "A navigation system for open liver surgery: design, workflow and first clinical applications," *The International Journal of Medical Robotics + Computer Assisted Surgery: MRCAS*, Oct. 2010.
[98] A. J. Herline et al., "Image-Guided Surgery: Preliminary Feasibility Studies of Frameless Stereotactic Liver Surgery," *Arch Surg*, vol. 134, no. 6, pp. 644-650, Jun. 1999.
[99] A. Dalvi, M. Faria, and A. Pinto, "Non-suture closure of wound using cyanoacrylate," *Journal of Postgraduate Medicine*, vol. 32, no. 2, pp. 97-100, Apr. 1986.
[100] W. Schroeder, K. Martin, and B. Lorensen, *The Visualization Toolkit, Third Edition*, 3rd ed. Kitware Inc., 2004.
[101] K. A. Gavaghan, M. Peterhans, T. Oliveira-Santos, and S. Weber, "A portable image overlay projection device for computer-aided open liver surgery," *IEEE Transactions on Bio-Medical Engineering*, vol. 58, no. 6, pp. 1855-1864, Jun. 2011.
[102] C. Hansen, J. Wieferich, F. Ritter, C. Rieder, and H.-O. Peitgen, "Illustrative visualization of 3D planning models for augmented reality in liver surgery," *International Journal of Computer Assisted Radiology and Surgery*, vol. 5, no. 2, pp. 133-141, Mar. 2010.
[103] M. Sugimoto et al., "Image overlay navigation by markerless surface registration in gastrointestinal, hepatobiliary and pancreatic surgery," *Journal of Hepato-Biliary-Pancreatic Sciences*, vol. 17, no. 5, pp. 629-636, Sep. 2010.
[104] S. Weber, M. Klein, A. Hein, T. Krueger, T. C. Lueth, and J. Bier, "The Navigated Image Viewer – Evaluation in Maxillofacial Surgery," in *Medical Image Computing and Computer-Assisted Intervention - MICCAI 2003*, vol. 2878, R. E. Ellis and T. M. Peters, Eds. Berlin, Heidelberg: Springer Berlin Heidelberg, 2003, pp. 762-769.
[105] A. Wagner, M. Rasse, W. Millesi, and R. Ewers, "Virtual reality for orthognathic surgery: the augmented reality environment concept," *Journal of Oral and Maxillofacial Surgery: Official Journal of the American Association of Oral and Maxillofacial Surgeons*, vol. 55, no. 5, pp. 456-462; discussion 462-463, May 1997.
[106] C. Nikou, A. M. Digioia III, M. Blackwell, B. Jaramaz, and T. Kanade, "Augmented reality imaging technology for orthopaedic surgery," *Operative Techniques in Orthopaedics*, vol. 10, no. 1, pp. 82-86, Jan. 2000.

[107] M. Blackwell, F. Morgan, and A. M. DiGioia 3rd, "Augmented reality and its future in orthopaedics," *Clinical Orthopaedics and Related Research*, no. 354, pp. 111-122, Sep. 1998.
[108] B. Schwald, H. Seibert, M. Schnaider, S. Wesarg, and R. Röddiger, "Implementation and Evaluation of an Augmented Reality System Supporting Minimal Invasive Interventions," in *Proceedings of the International Status Conference Virtual and Augmented Reality*, Leipzig, Germany, 2004, p. 10.
[109] H. Liao, H. Ishihara, H. H. Tran, K. Masamune, I. Sakuma, and T. Dohi, "Precision-guided surgical navigation system using laser guidance and 3D autostereoscopic image overlay," *Computerized Medical Imaging and Graphics*, vol. 34, no. 1, pp. 46-54, Jan. 2010.
[110] J. Marescaux, F. Rubino, M. Arenas, D. Mutter, and L. Soler, "Augmented-reality-assisted laparoscopic adrenalectomy," *JAMA: The Journal of the American Medical Association*, vol. 292, no. 18, pp. 2214-2215, Nov. 2004.
[111] H. Fuchs et al., "Optimizing a head-tracked stereo display system to guide hepatic tumor ablation," *Studies in Health Technology and Informatics*, vol. 132, pp. 126-131, 2008.
[112] F. Sauer, A. Khamene, B. Bascle, L. Schinunang, F. Wenzel, and S. Vogt, "Augmented reality visualization of ultrasound images: system description, calibration, and features," in *IEEE and ACM International Symposium on Augmented Reality, 2001. Proceedings*, 2001, pp. 30-39.
[113] F. Volonte et al., "Mixed reality for laparoscopic distal pancreatic resection," *International Journal of Computer Assisted Radiology and Surgery (Abdominal and Laparoscopic Surgery)*, vol. 5, p. S126-S127, May 2010.
[114] J.-p Tardif, S. Roy, and J. Meunier, "Projector-Based Augmented Reality in Surgery without Calibration."
[115] Z. Zhang, "A flexible new technique for camera calibration," *IEEE Transactions on Pattern Analysis and Machine Intelligence*, vol. 22, no. 11, pp. 1330- 1334, Nov. 2000.
[116] A. Schenk et al., "Clinical relevance of model based computer-assisted diagnosis and therapy," 2008, vol. 6915, pp. 691502-691502-19.
[117] S. Tucker et al., "Comparison of actual surgical outcomes and 3-dimensional surgical simulations," *Journal of Oral and Maxillofacial Surgery: Official Journal of the American Association of Oral and Maxillofacial Surgeons*, vol. 68, no. 10, pp. 2412-2421, Oct. 2010.
[118] H. Bou Sleiman, L. E. Ritacco, L. Aponte-Tinao, D. L. Muscolo, L.-P. Nolte, and M. Reyes, "Allograft selection for transepiphyseal tumor resection around the knee using three-dimensional surface registration," *Annals of Biomedical Engineering*, vol. 39, no. 6, pp. 1720-1727, Jun. 2011.

List of Tables

Table 1: Average and standard deviation of the error sources presented in millimetres..... 37
Table 2: Convergence Percentage per Initial Distance. Average time is given in seconds. 47
Table 3: Average distance and time per target. 53
Table 4: Description of the single marker designs with the respective visibility ranges. ... 59
Table 5: Scenarios applied during tracking. 72
Table 6: Percentage of errors (i.e. wrong marker assignments) for 10 different SM arrangements under different tracking scenarios..... 73
Table 7: Data types visualized using AR image overlay projection..... 88

List of Figures

Figure 1: Two examples of needles used for percutaneous interventions. 1

Figure 2: Example of a needle that is used to puncture soft tissue. It comprises a trocar and a cannula. The trocar fits inside the cannula and can be removed when it is not needed. 2

Figure 3: Examples of different image modalities used for needle (pointed by arrows) guidance. a) Ultrasound-guided biopsy (Source: [8]). b) Fluoroscopic needle guidance for percutaneous nephrolithotomy. c) CT-guided biopsy of vertebral body (Source: [9]). d) MR-guided biopsy of vertebral body (Source: [10]). Arrows were additionally added to the images. 3

Figure 4: a) Illustration of a patient positioned for a PET/CT image acquisition (Source: © Siemens AG). b) Example of a PET/CT-guided needle placement for biopsy. 4

Figure 5: Bone biopsy kit example comprising a cannula of 3.4 mm outer diameter (10 G) and 130 mm length, a trocar, a drill and 5 mm long distance holders. 5

Figure 6: PET/CT image fusion showing a lesion in the bone. a) Initial PET fused with initial CT. b) Initial PET fused with control CT. The target displacement introduced by patient movement is highlighted by the arrows. 6

Figure 7: Challenges faced during investigation of a clinically applicable navigation system for percutaneous needle intervention. 7

Figure 8: General navigation system overview. The instrument and patient poses, ${}^{pms}T_{idr}$ and ${}^{pms}T_{pdr}$, are measured by the position measurement system and overlaid on the image data by means of a patient-to-image registration transformation, ${}^{img}R_{pdr}$ (as illustrated in the visualization). 12

Figure 9: Image guidance systems subdivided in four aspects. 12

Figure 10: Image modalities experiments realized in (Source: [45]). a) PET/CT image of the interventional phantom with 6 mCi of ^{18}F-Fluorodeoxyglucose fiducials (arrows). b) Tracked needle position (small arrow) is displayed near internal target (large arrow) from pre-procedural PET during tracked needle insertion. 13

Figure 11: Experimental setups highlighting: a) the self developed stereoscopic optical system, the guidance interface and the user performing the puncture with the tracked needle (Source: [35]); b) the Polaris optical tracking system from NDI, the guidance interface and the user performing the procedure (Source: [40]); c) the electromagnetic field generator Aurora from NDI, the fiducials used for registration, and the tracked needle (Source: [45]); d) the electromagnetic field generator, the head tracking device (optical tracking), and the instruments being tracked (Source: [39]). 15

Figure 12: Needle calibration methods. a) Pivot for calculating tip location. b) Chamfer for calculating axis orientation. c) Calibration unit for calculating tip location and axis orientation by means of a guiding hole. 17

Figure 13: Illustration of a patient fixation and rigid tracking setup. The patient is immobilized with a vacuum mattress and tracked by a dynamic reference (optical markers) attached to the patient stretcher (Source: [72], image was cropped to emphasise the fixation and tracking devices). 18

Figure 14: a) Patient tracking by means of rigid dynamic reference (DR) (Source: [60]). b) Patient tracking by means of radio-opaque marker detected from video images (Source: [37]). The pair of images correspond to one frame of the stereo camera. It shows one pair of reliable marker detection and one pair of ambiguous detection. c) Patient tracking by means of navigation aids (left) and virtual 3D view showing the navigation aids in the liver (right) (Source: [54]). 19

Figure 15: Planning of an entry point for the needle (left) and a target location (right) for radio-frequency ablation (Source: [77]). 20

Figure 16: Instrument guidance viewers. a) Needle angle and position relative to the target site displayed as circle and cross in the middle on the cross-hair (Source: [42]). b) Axial view (top-left), off-sagittal view (top-right), off-axial (bottom-left), and targeting view (bottom-right) (Source: [78]). c) States of a targeting process evaluated by the DKFZ group (Source: [79]). Insertion point reached (first row), needle aligned (second row), needle insertion started (third row), target point reached (forth row). d) Augmented reality view displaying the 3D reconstruction of the liver and the virtual needle on the top of a video frame (Source: [35]). 21

Figure 17: Diagram relating the deficits (red) of the state of the art approaches for image guidance of percutaneous needle interventions based on multimodal images and the respective improved approaches proposed in this thesis (green). 26

Figure 18: Navigation system overview. The transformations ${}^{cam}T_{ndr}$ and ${}^{pdr}T_{cam}$ are measured by the position sensor, whereas the ${}^{img}R_{pdr}$ is the patient-to-image registration.... 30

Figure 19: a) 3D viewer showing an overview of the planned situation and the orientation of the trajectory viewer. b) Trajectory viewer showing the planned trajectory and possible obstacles. c) Navigation platform beside the PET/CT scanner table. d) Needle and calibration unit in calibration position. 31

Figure 20: a) Shows the targeting viewer schematic. The virtual camera is aligned with the planned trajectory and looks to the target. The needle tip and the needle shaft are projected back to the crosshair plane, and are respectively displayed as a cross and a circle that is complementary to the cross. Both are connected through a line. The viewer background displays the fused PET/CT slice orthogonal to the planned trajectory at the depth of the needle tip d, or alternatively 10 mm beyond the tip, $d + 10$. b) Shows the needle plane viewer schematic. The virtual camera looks to the needle tip, has its y axis parallel to the needle and its x axis parallel to the cross product between the needle and the z axis of needle DR. The viewer background displays the PET/CT slice surrounding the needle axis. In order to aid the physician in predicting the final tip position if the needle continues in the current direction, a projection of the needle along the remaining distance d is displayed.32

Figure 21: a) Shows the targeting viewer with the needle aligned with the planned trajectory and moving towards the target. The distance to the target is displayed in the left bar, and is also represented by the distance arrows approaching the centre of the cross hair target, which removes the necessity to deviate ones attention from the centre of the viewer. b) Shows the needle plane viewer displaying the needle, its projection to the target, and the PET/CT slice along the needle axis. 32

Figure 22: System workflow emphasizing the non-sterile and sterile phases, and the particularities of bone and soft tissue interventions. 34

Figure 23: Illustration of the target projection and error components. a) Shows different projection methods: patient DR registration transformation R_{pdr}, rigid structure

registration transformation R_{rig}, and machine coordinate system transformation R_{mcs}. b) Shows locations of the target projected with different methods: patient DR registration transformation $R_{pdr}P_{plt}$, rigid structure registration transformation $R_{rig}P_{plt}$, and machine coordinate system transformation $R_{mcs}P_{plt}$. Additionally, the picture on the right illustrates how the different error vectors correlate to each other. 36

Figure 24: a) Shows the best result for bone punctures, puncture 14 in S1 with a planned trajectory length of 81 mm. b) Shows the best result for soft tissue punctures, puncture 2 in S3 with a planned trajectory length of 98 mm. 37

Figure 25: The figures a) and b) show the different error sources per puncture for bone and soft tissue punctures respectively, ordered by the overall error. The figures c) and d) show the correlation between the error sources and the overall error for bone and soft tissue punctures respectively. The lines represent the linear fitting of each error source. 39

Figure 26: Results of punctures in S2 with high error in the drilling direction. a) Puncture 2. b) Puncture 3. c) Puncture 5. d) Puncture 7. 39

Figure 27: Shows the different error sources per: a) patient DR to target distance for bone punctures, b) patient DR to target distance for soft tissue punctures, c) trajectory length of the bone punctures, d) trajectory length of the soft tissue punctures. The lines represent the linear fitting of each error source. 40

Figure 28: Illustration of the registration pipeline. 43

Figure 29: Reference mask generation example. a) Original reference image. b) Binary bone outer surface threshold of image a). c) Seed point (cross) closest blob selected from image b). d) Resulting reference mask overlaid with image a). 43

Figure 30: Puncture graphs comparing the SAD behaviour of the registration pipeline (RP) against standard registration (SR) using ROI sizes using MI and NC metrics. 46

Figure 31: Registration example for ROI size 90 mm. a) Reference image. b) Moving image. c) Reference mask. d) Moving mask. e) Subtracted registration pipeline MI results. f) Subtracted registration pipeline NC results. g) Subtracted standard registration MI results. h) Subtracted standard registration NC results. Subtracted images are the absolute difference between reference and transformed moving image displayed with window/level equal to 200/100. 46

Figure 32: Patient optical reference setup with the fiducial marker used for imaging and their respective positions marked with a surgical pen. 50

Figure 33: Instrument guidance system. 50

Figure 34: Rapid prototype model used to demonstrate the system to the physicians. 51

Figure 35: a) 3D viewer showing the planned access point. b) Trajectory viewer showing the planned trajectory with possible anatomical obstacles. 52

Figure 36: a) Target viewer. b) Needle plane viewer. 52

Figure 37: Suspicious lesion location displayed in the axial (lower right), sagittal (upper right), and coronal (upper left) slices with fused PET and CT of the patient's head. 54

Figure 38: Instruments and patient preparation. a) Shows the instrument to be tracked with the respective dynamic reference (DR) attached to the instrument shaft via a clamp, and the calibration unit used to calibrate the instrument intra-operatively.

b) Shows the patient dynamic reference attached to the patient forehead via a band in order to provide referencing to the patient. 55

Figure 39: Overview of the planned scenario. a) Volume rendering of the patient's head with the planned trajectory. b) Trajectory plane (located at position showed in a)) showing the planned trajectory comprising a target and an entry point. 55

Figure 40: Overview of the five landmarks used during the intervention in order to register the patient to the image. 55

Figure 41: Overview of the instrument guidance. a) Intervention setup with image guidance (IG) system facing the surgeon. b) Close-up to the patient head and tracked instrument. c) Virtual view of the patient head and the tracked instrument displayed in the upper monitor of the image guidance system. d) Targeting viewer (left) and needle plane viewers used to guide the instrument to the target. 56

Figure 42: Overview of the patient tracking approach based on retro-reflective single. A set of single markers is placed on the patient's skin, the patient is imaged, and the position of each single marker in the image is used to initialize the tracking algorithm. Based on the position of each single marker measured by the position sensor, the tracking algorithm estimates the current patient pose, ${}^{pdr}T_{pms}$, and the amount of deformation (e.g. during breathing, going from non deformed represented in green to deformed in red). 57

Figure 43: Illustration of the visibility angle experiment. 58

Figure 44: Example of attachment of single markers type 3 on the patient skin with 3M™ Tegaderm™ Dressings (from 3M AG, Switzerland). a) Place post under the adhesive side if the tape. b) Place the marker post at the desired position. c) Screw the sphere in the post. d) Single marker attached to the skin. 59

Figure 45: Example of single markers visibility in CT images. a) Axial view of a patient with a single marker attached on the abdomen. b) Axial zoom of the single marker displayed in a). c) Sagittal zoom of the single marker displayed in a). d) Coronal zoom of the single marker displayed in a). 60

Figure 46: Localization pipeline overview. An image of the patient with the single markers is given as input. The candidate to single markers are identified. The region of interest (ROI) is extracted. The spheres of each selected ROI is identified and a list of 3D positions of the sphere centres, ${}^{img}P_{SC}$, in the image coordinate system is given as output. 61

Figure 47: Overview of the steps and outcomes of the process to select candidates to single markers. An image of the patient with the single markers is given as input. A Gaussian filter smoothes the image. A threshold based segmentation eliminates the soft tissue of the image. The posts are selected considering their physical size, and a list containing the 3D position of the centre of each post bounding box, ${}^{img}P_{PL}$, in image coordinate system is given as output. 61

Figure 48: Comparison of threshold applied to remove soft tissue. a) Shows an example of the threshold segmentation directly applied on the image. b) Shows an example of the threshold segmentation after application of the Gaussian filter. 62

Figure 49: Voting process of a Hough transform. a) Classical circular Hough transform. b) Classical Hough transform considering multiple radii in one parameter space. c) Oriented Hough Transform. d) Oriented Hough transform considering multiple radii in one parameter space. (Source: [91]) 62

Figure 50: Overview of the steps and outcomes of the process to precisely determine the centre of each sphere. A small region containing one of the single markers of the patient image is given as input. The image is resampled to higher resolution and isotropic voxels. A threshold based segmentation selects the air of the image. The largest blob representing air is kept and inverted to background. A fast 3D Hough transform votes for pixels with high probability of being the centre of the sphere. A Gaussian adjusts the contributions of voxels within a certain region. Finally, the maxima of the smoothed image is located and used as the centre of the sphere (red cross). 64

Figure 51: Comparison of sphere localization error for the automatic and the manual methods. The boxes represent the average and standard deviation errors, and the bars represent the minimum and maximum errors. 65

Figure 52: Example of the automatic localization pipeline results. a) Best case with an error of 0.05 mm. b) Worst case with error of 0.65 mm. 65

Figure 53: Axial view of the excluded single marker. The original image is showed in the left and a modified version highlighting the shadow produced is showed in the right. 65

Figure 54: a) Comparison of the single marker localization time for the automatic and the manual methods. The time represents the localization of six single markers in one image. The boxes represent the average and standard deviation time, and the bars represent the minimum and maximum time. b) The behaviour of time according to the image size. The total single marker localization time, the spheres localization time, and the posts localization time are displayed as three different curves. 66

Figure 55: Illustration of the coordinate systems and transformations (left). Illustration of the data flow within the SM tracking algorithm (right). 68

Figure 56: Illustration of two situations**,** a) and b), where phantom markers are created. 69

Figure 57: Illustration of the phantom removal. 70

Figure 58: Surgical workflow overview. 72

Figure 59: a) Phantom experiment: arrows represent the liver rotation. b) Axial compression: arrows represent the direction of forces applied. c) Handling: arrows represent the direction of forces applied. d) Rigid motion: arrows represent the direction of motion. Target point is represented by the x. 73

Figure 60: Frequency of phantom positions produced during one 360° rotation of the liver in front of the *pms* for one of the SM set arrangements. 73

Figure 61: (Left) Boxplot of TRE values for the 4 targets for 5 SM arrangements. (Right) Difference in target localization and DRB fitting error for one of the SM arrangement. 74

Figure 62: Comparison of deformation measured by single markers and one evaluation point under axial compression and simulated surgical handling of a silicon liver phantom. 74

Figure 63: Example of tracking under deformation. a) Deformable phantom with a set of six single markers and a needle being guided to the target. b) Viewers displaying the guidance and deformation information. The top viewer displays an overview of the intervention scenario with the needle and the individual error of each marker. The bottom viewer displays average fiducial registration error over time..... 75

Figure 64: Overview of the changes performed in the system workflow to incorporate the tracking of non-rigid structures approach presented above. The patient preparation was altered (orange) to include the single markers placement. The automatic single marker detection was added (green) to reduce the necessary user interaction. Patient-to-image registration (red) is now continuously performed in the during instrument guidance. Instrument guidance (orange) was altered to include deformation information. 76

Figure 65: Kidney stones (arrows) showed in the axial (lower right), sagittal (upper right), and coronal (upper left) slices of a diagnose CT of the patient. 77

Figure 66: Overview of process to attach the single markers for image acquisition of percutaneous nephrolithotomy interventions. a) Draw the position of each single marker with a surgical pen. b) Attach the single marker posts with 3M™ Tegaderm™ Dressings. c) Screw spheres on the posts. d) Acquire CT image of the patient including single markers and kidney. 78

Figure 67: Example of a planned trajectory. a) Volume rendering of the patient with the planned trajectory. b) Trajectory plane (located at position showed in a)) showing the planned trajectory comprising a target and an entry point. 78

Figure 68: Overview of process to attach the single markers for patient referencing during percutaneous nephrolithotomy interventions. a) Attach the single marker posts with 3M™ Tegaderm™ Dressings at the marked positions. b) Screw sterile spheres on the posts. c) Final sterile single markers arrangement. 79

Figure 69: Overview of the percutaneous nephrolithotomy intervention. a) Surgeon guiding the needle to the kidney collecting system. b) Fiducial registration error of the single marker set for the 33 measurement stored during the intervention. The boxes represent the average and standard deviation error, and the bars represent the minimum and maximum error. 79

Figure 70: Fiducial registration error of the single marker set during the single markers re-attachment and patient re-positioning experiment. The boxes represent the average and standard deviation error, and the bars represent the minimum and maximum error. 80

Figure 71: Image overlay projection device employed for AR visualisation. 83

Figure 72: Image overlay system transformation diagram. 84

Figure 73: Stereotactic instrument guidance system with integrated IOD employed within this study. 85

Figure 74: Unmodified original 3D anatomical models from navigation/planning software employed in previous surgical procedures. a) Liver resection plan. b) CMF osteotomy plan. c) Proximal tibia resection plan. 86

Figure 75: Unmodified original biopsy guidance displays from navigation software with patient PET data. a) Biopsy needle tip entry site alignment. b) biopsy needle shaft alignment. c) biopsy needle depth guidance with visible target lesion (PET data). 87

Figure 76: a) Image overlay AR for navigated liver surgery on a patient specific rigid model and b), pig liver tissue; c) and d) Image overlay AR for navigated CMF surgical planning; e) and f) Image overlay AR for navigated orthopaedic tumour resection. 89

Figure 77: Image overlay projection of percutaneous needle guidance information throughout a simulated biopsy procedure. a) Tip alignment. b) Shaft alignment. c) Aligned needle at point of puncture. d) Depth guidance. e) Target visualisation. 90

Complete List of Publications

In Journals

- K. Gavaghan, **T. Oliveira-Santos**, M. Peterhans, M. Reyes, H. Kim, S. Weber, "Evaluation of a portable image overlay projector for the visualisation of surgical navigation data: phantom studies," *International Journal of Computer Assisted Radiology and Surgery*, 2011, In Press.
- **T. Oliveira-Santos**, B. Klaeser, T. Weitzel, T. Krause, L.-P. Nolte, and S. Weber, "A Navigation System for Percutaneous Needle Interventions Based on PET/CT Images: Design, Workflow and Error Analysis of Soft Tissue and Bone Punctures," *Computer Aided Surgery*, 16(5):203-19. Jul. 2011.
- K. Gavaghan, M. Peterhans, **T. Oliveira-Santos**, and S. Weber, "A Portable Image Overlay Projection Device for Computer Aided Open Liver Surgery," *IEEE Transactions on Biomedical Engineering*, vol 58, no. 6, pp. 1855-1864, Jun. 2011.

Full Papers in Conference Proceedings

- K. Gavaghan, S. Anderegg, M. Peterhans, **T. Oliveira-Santos**, and S. Weber, "Augmented Reality Image Overlay Projection for Image Guided Open Liver Ablation of Metastatic Liver Cancer," in *Conference Proceedings of the 6th MICCAI 2011 Workshop on Augmented Environments for Computer-Assisted Interventions*, Toronto, Canada, 2011, pp. 78-88.
- **T. Oliveira-Santos**, M. Peterhans, S. Hofman, and S. Weber, "Passive Single Marker Tracking for Organ Motion and Deformation Detection in Open Liver Surgery," in *Conference Proceedings of Information Processing in Computer-Assisted Interventions (IPCAI)*, Berlin, Germany, 2011, LCNS 6689, pp. 156-167.
- **T. Oliveira-Santos**, S. Hofmann, M. Peterhans, and S. Weber, "Soft Tissue Surface Tracking for Open Liver Surgery," in *Conference Proceedings of Computer- und Roboterassistiert Chirurgie (CURAC)*, Düsseldorf, Germany, 2010, vol. 9, pp. 39-43.
- M. Peterhans, S. Anderegg, P. Gaillard, **T. Oliveira-Santos**, and S. Weber, "A fully automatic calibration framework for navigated ultrasound imaging," in *Conference Proceedings of Engineering in Medicine and Biology Society (EMBC), 2010 Annual International Conference of the IEEE*, Buenos Aires, Argentina, 2010, vol. 1, pp. 1242-1245.
- **T. Oliveira-Santos** et al., "Multimodal target correction by local bone registration: A PET/CT evaluation," in *Conference Proceedings of Engineering in Medicine and Biology Society (EMBC), 2010 Annual International Conference of the IEEE*, Buenos Aires, Argentina, 2010, vol. 1, pp. 5616-5619.
- **T. Oliveira-Santos** et al., "Computer aided surgery for percutaneous nephrolithotomy: Clinical requirement analysis and system design," in *Conference Proceedings of Engineering in Medicine and Biology Society (EMBC), 2010 Annual International Conference of the IEEE*, Buenos Aires, Argentina, 2010, vol. 1, pp. 442-445.

Abstracts in Conference Proceedings

- **T. Oliveira-Santos** et al., "Navigated Percutaneous Needle Intervention Based on PET/CT Images," in *Conference Proceedings of Swiss Society for Biomedical Engineering (SSBE)*, Bern, Switzerland, 2011, p. 51.
- K. Gavaghan, **T. Oliveira-Santos**, M. Peterhans, S. Anderegg, and S. Weber, "Augmented reality for image guided surgery," in *Conference Proceedings of Swiss Society for Biomedical Engineering (SSBE)*, Bern, Switzerland, 2011, p. 51.
- **T. Oliveira-Santos** et al., "Positron Emission Tomography/Computer Tomography (PET/CT) Navigated Biopsy: Discrete Surface Tracking," in *Graduate School Symposium 2011 Proceedings*, Bern, Switzerland, 2011.
- K. Gavaghan, **T. Oliveira-Santos**, M. Peterhans, M. Reyes, H. Kim, and S. Weber, "Portable image overlay projection for the visualization of surgical planning and navigation data," in *Conference Proceedings of Computer Assisted Radiology and Surgery (CARS)*, Berlin, Germany, 2011
- **T. Oliveira dos Santos** et al., "Positron Emission Tomography/Computer Tomography (PET/CT) Navigated Biopsy: Discrete Surface Tracking," in *Graduate School Symposium 2011 Proceedings*, Bern, Switzerland, 2011.
- B. Klaeser, T. Weitzel, **T. Oliveira dos Santos**, S. Weber, and T. Krause, "Instrument guidance based on multi-modality imaging: Validation of an optical system for computer-assisted PET-CT guided interventions," in *J Nucl Med*, 2010, vol. 51, (Supplement 2):9.
- **T. Oliveira dos Santos** et al., "Positron Emission Tomography/Computer Tomography (PET/CT) Navigated Biopsy," in *Graduate School Symposium 2010 Proceedings*, Bern, Switzerland, 2010.
- **T. Santos**, T. Weitzel, B. Klaeser, M. Reyes, and S. Weber, "Introducing Computer-Assisted Surgery into combined PET/CT image based Biopsy," in *Conference Proceedings of 9th Annual Meeting of Computer Assisted Orthopaedic Surgery-International (CAOS)*, Boston, USA, 2009, pp. 308-311.
- **T. Oliveira dos Santos**, B. Klaeser, T. Weitzel, M. Reyes, and S. Weber, "Pet-Ct Navigated Biopsy: A Feasibility Study," in *Conference Proceedings of Swiss Society for Biomedical Engineering (SSBE)*, Bern, Switzerland, 2009, p. 42.

Declaration of Originality

Last name, first name: **Oliveira dos Santos, Thiago**

Matriculation number: **08-124-257**

I hereby declare that this thesis represents my original work and that I have used no other sources except as noted by citations.
All data, tables, figures and text citations which have been reproduced from any other source, including the internet, have been explicitly acknowledged as such.
I am aware that in case of non-compliance, the Senate is entitled to divest me of the doctorate degree awarded to me on the basis of the present thesis, in accordance with the "Statut der Universität Bern (Universitätsstatut; UniSt)", Art. 20, of 17 December 1997.

Place, date Signature

…… ……